ISSN 2949-561X (Online)

APPLIED PHYSICS

2` 26

Applied Physics
2026, No. 2

The journal was founded in 1994

The scientific and technical peer-reviewed journal is intended for the publication of articles on the latest achievements in the field of physics with prospects for advancements (technical and scientific) applications.

The periodicity is 6 issues per year.

Founder and publisher

Research, Development and Production Center ORION, Joint-Stock Company – Russian Federation State Science Center
(RD&P Center ORION, JSC)
9, Kosinskaya st., Moscow, 111538 Russia

The journal is included in the Unified State List of Scientific Publications. The Journal is included in Scientific Electronic Library eLIBRARY.RU, SCOPUS, Chemical Abstracts (CA), Russian Science Citation Index (RSCI), Directory of Open Access Journals (DOAJ), Directory of Open Access Scholarly Resources (ROAD), Google Scholar.

Editor-in-Chief

Editorial office address

9, Kosinskaya st., Moscow, 111538, Russia,
RD&P Center ORION, JSC.
Phone: 8(499) 374-82-40
E-mail: advance@orion-ir.ru
Internet: applphys.orion-ir.ru

The registration PI No. FS 77-73641
was issued in September 21, 2018
by the Federal Service for Supervision
of Communications, Information Technology, and Mass Media of Russia

Editorial Board

APPLIED PHYSICS [in Russian]

THE SCIENTIFIC AND TECHNICAL JOURNAL

2026, No. 2 | Founded in 1994 | Moscow

C O N T E N T S

PHYSICAL SCIENCE OF MATERIALS

ELECTRON, ION AND LASER BEAMS

PHYSICAL EQUIPMENT AND ITS ELEMENTS

INFORMATION

GENERAL PHYSICS

UDC 621.384.62; 629.7 PACS: 87.65.+y, 96.50.Pw
EDN: ZIHYVW

Analysis of the composition and sources of deposition on the ISS surface

L. M. Vasilyak[1*], A. V. Peklevskiy[2], S. P. Prokopovich[2], V. N. Chikirev[2], and E. V. Shubralova[2]

[1] *Joint Institute for High Temperatures of the Russian Academy of Sciences, Moscow, 125412 Russia*
[*] *E-mail: vasilyak@ihed.ras.ru*
[2] *Joint Stock Company "Central Research Institute for Machine Building", Moscow Region, Korolev, 141070 Russia*

Received 9.12.2025; revised 23.01.2026; accepted 27.04.2026

The fine deposition delivered from the surface of the International Space Station (ISS), particles of cosmic dust, particles of meteoroid, volcanic and marine origin, enriched with organic matter. These particles are present in the Earth's exosphere and, under conditions of corpuscular, X-ray and ultraviolet irradiation, are an aggressive agent for the surface materials of orbital stations. An analysis of the elemental composition of deposition on the ISS surface made it possible to assess the effect of the detected elements on the stability of the structural materials of the orbiting objects, as well as to identify the sources of their entry onto the ISS surface.

Keywords: international space station, fine deposition, exosphere.

DOI: 10.51368/2949-561X-2026-2-5-9

For citation: Vasilyak L. M., Peklevskiy A. V., Prokopovich S. P., Chikirev V. N., and Shubralova E. V., Applied Physics, No. 2, 5–9 (2026).

Introduction

Possible sources of regular deposition of fine particulate matter on the surface of an orbital station may be particles of meteoroids and comet tails, delivering molecules of the interstellar medium adsorbed by them, and cosmic dust particles from outer space [1–7]. Data on 36 regular streams of comet tails crossing near-Earth space are well known; particle velocities are in the range from 18 to 70 km/s. The "UV Atmosphere" telescope on the ISS registers micrometeorites entering the nadir zone. At this time, the ISS is located in the zone of a comet tail particle stream, and the registration of meteoroid glow by the "UV Atmosphere" telescope is a sign of possible contact of particles with the ISS surface. This proves that the Earth's exosphere includes minute particles of cosmic origin continuously moving toward the Earth [3], which fall onto the surface of an orbital object. In addition, particles from the Earth resulting from volcanic activity and the uplift of microparticles in the electric fields of the global electric circuit of the Earth may also be present in the exosphere [1, 7]. All these particles may be present in the sediment on the ISS surface, along with products of station material degradation. From 2010 to 2024, under the "Test" program, sampling of fine particulate matter from the external surface of the pressure hull of the Russian segment of the ISS was carried out, and disperse, chemical, and geological-mineralogical analyses of the samples delivered to Earth were performed. Based on the analysis of the sediment from different elements of the ISS, conclusions can be drawn about the composition of the sediment, as well as about its sources. In addition, conclusions can be drawn about the possible danger of the sediment to station materials or to cosmonauts.

Analysis of sediment composition

The following methods are used to obtain the results of post-flight physicochemical analysis

of fine particulate matter on the surfaces of elements of the "Test-Exponat" device after a long period in open space: mass spectrometry, inductively coupled plasma atomic emission spectrometry, electron paramagnetic resonance spectrometry, and scanning electron microscopy. In the experiment completed in 2024, during the research carried out under the "Test" program, the elemental composition of the contaminant on the fluoroplastic body of the "Test-Exponat" device, which had been located on the external surface of the "Poisk" module for 3.5 years, was studied. The quantitative and elemental composition was determined by inductively coupled plasma optical emission spectrometry (the ICP-OES method) as the most reproducible and metrologically supported. The microwave sample digestion system allows all elements contained on various carriers to be transferred into solution.

In micrographs of the body surface, the pattern of sediment deposition can be observed (Fig. 1). The contamination is contained on any irregularities and roughnesses left by the milling cutter during fluoroplastic processing. At the same time, no particles were detected on the surface of the material. For investigation using a scanning electron microscope, a section (Fig. 1) of the contaminated surface layer of fluoroplastic from the body of sampler No. 17A was made. It should be noted that the contrast of the scanning electron image is due to the difference in electrical conductivity of the material. The cracks were formed as a result of section deformation (Fig. 1) and do not contain contamination. The rest of the material surface, and especially the pores in it, are contaminated with sediment, as a result of which they have some electrical conductivity, and consequently, appeared dark in color.

Studies of the elemental composition of the contaminant on the fluoroplastic body of the "Test-Exponat" device (Fig. 2) have a number of advantages, since fluoroplastic does not change during subsequent sample preparation and contains a minimal amount of mineral impurities. A control sample of the fluoroplastic scraping was obtained from the same body. The original fluoroplastic contains extremely few foreign inclusions, and the method error can be assessed by the only factor that is difficult to account for in this experiment – the degree of contamination by hands and dust contamination of the sample with ordinary dust. These contaminants, as a rule, introduce calcium into the sample, and to a lesser extent magnesium and silicon, which is observed in the analysis results.

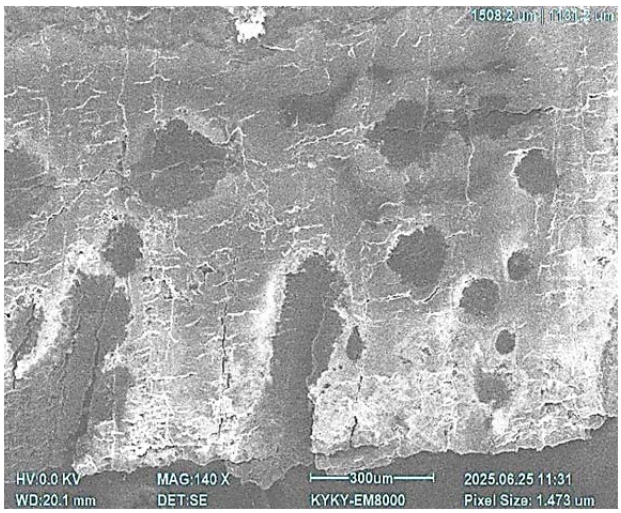

Fig. 1. Micrograph of the fluoroplastic fragment obtained by scanning electron microscopy (SEM) after conducting the ICP-OES.

Among the 65 chemical elements identified in the composition of fine particulate matter on the ISS surfaces in the period from 2010 to 2024, the most common element was iron, which is practically not used in the structural elements of the station. Moreover, iron was not detected in only 5 out of 46 samples studied under the "Test" program. Analysis of the relative content of iron and nickel in the samples allows clarification of the origin of iron in the sediment. According to the obtained results of the study of exposed bodies of the "Test-Exponat" device [2], iron was detected in significant quantities: 536 μg/mL. A peak of nickel content was also detected in the OES spectrum, but its content is lower: 1.6 μg/mL. Thus, the iron/nickel ratio in the studied sample is 335, whereas in samples of meteoritic origin, as is well known, the iron/nickel ratio is practically constant and ranges from 11.5 to 14, averaging 12. This allows the conclusion that the iron particles are not only of meteoritic origin.

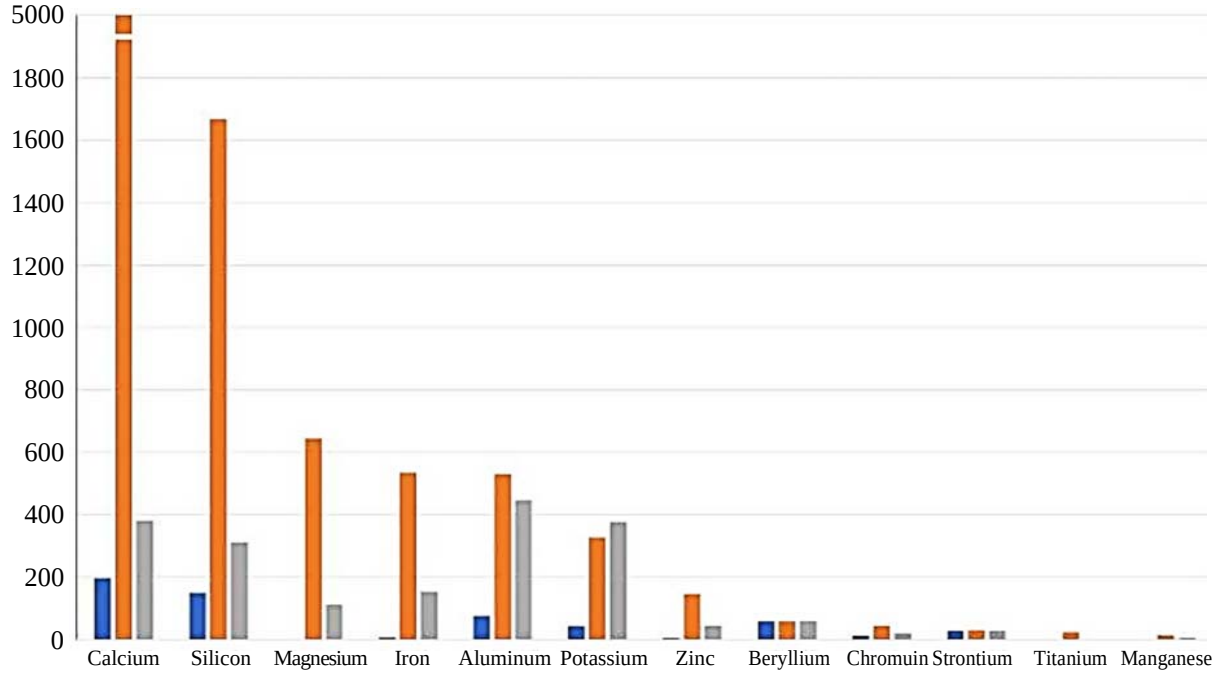

Fig. 2. Elemental composition of the scraping from fluoroplastic bodies. Left blue column – pure fluoroplastic, middle orange column – sampler 17A, right gray column – sampler 18A

The elemental composition of cosmic dust collected from the ISS surface earlier suggests a significant contribution of mixed tropospheric aerosol of terrigenous and marine origin [6, 7]. Volcanic gases rising beyond the atmosphere may contain iron chloride, released at high temperatures from magmatic melt. The presence of iron chlorides in volcanic gases is associated with the reaction of magma with chlorine-containing compounds, which can also be released during an eruption. Anhydrous iron (III) chloride ($FeCl_3$) becomes volatile, which upon strong heating transitions to a gaseous state, forming monomers ($FeCl_3$) and dimers (Fe_2Cl_6).

Studies of the physicochemical properties of fine particulate matter on the ISS surface have confirmed the possibility of its active participation in the development of microdestruction of ISS structural elements. Upon interaction of iron chloride with compact aluminum of the ISS body, accumulation of iron ions occurs, culminating in the release of iron in a free state and the appearance of ferrimagnetic particles, which was detected on the fluoroplastic surface. Chloride ions migrate through the oxide film to the metal, primarily at defect sites, increasing the corrosion rate and microdestruction of ISS elements.

In 27 out of 46 samples of fine particulate matter, elements of high electron affinity were identified, including Cl, F, and S. These elements are not permanent elements of cosmic dust, but they are always present in volcanic gas emissions, constituting up to 5 % of their total volume. It has been established that chemical processes involving elements of high electron affinity negatively affect the tightness of paronite seals in window structures.

The amount of detected magnesium exceeds the content of iron and aluminum not only in the samples of the fluoroplastic device that was exposed for 3.5 years, but also in other samples from the ISS surface. As a result of sampling on the ISS pressure hull in 2012 under the screen-vacuum thermal insulation, the following result of element content levels (μg/mL) was obtained: Mg – 181.55; Al – 39.85; Mn – 2.18. These data indicate a significant (4.5-fold) excess of magnesium content in the sample compared to aluminum, for example, in the composition of the AMg6 alloy: Mg – 6.8 %; Al – 93.68 %; Mn – 0.8 % [7].

It is known that the concentration of magnesium in marine and oceanic aerosols can vary from a few units to several tens or even hundreds of micrograms per cubic meter of air, and magnesium is one of the main components of aerosols of marine origin reaching orbital altitude via the global electric circuit [1]. The dynamic equilibrium of the Earth's exosphere is achieved

by a continuous flow of aerosols via the global electric circuit from the Earth and continuously moving streams of comet tail particles and cosmic dust in near-Earth space, arising from collisions of comets, asteroids, and other bodies in the Solar System.

Cosmic dust consists of small particles of solid matter composed of diatomic oxides MgO, SiO, CaO, FeO. Magnesium is almost entirely in the solid phase (as part of dust particles), rather than in the gas phase. The ratio of the magnesium-26 (Mg) and ordinary magnesium-24 (Mg) isotopes in meteorites allows dating of their formation [4, 5, 6]. The isotope 26(Mg) is a decay product of radioactive aluminum-26 (Al), which was present in the early Solar System. Its half-life is 717,000 years. In iron meteorites, this isotope is abundant compared to ordinary magnesium, while in chondrites it is practically absent. This indicates that chondrites arose somewhat later, when aluminum-26 in the rocks was already very scarce. It is estimated that this occurred approximately two to three million years after the formation of the Solar System. Thus, chondrites are meteorites of the second generation. The content of elements in particles of meteoric origin of the chondrite type averages: O (33.24 %), Fe (27.24 %), Si (17.19 %), Mg (14.29 %), S (1.93 %), Ni (1.64 %), Ca (1.27 %), Al (1.22 %), Na (0.64 %), Cr (0.29 %), Mn (0.25 %), P (0.11 %), and K (0.08 %).

Iron is one of the most abundant elements in the Universe after light elements such as hydrogen, carbon, and oxygen. Iron is most often found in gaseous form in stars, such as the Sun, and in condensed form on planets, in the composition of micrometeorites. Astrophysicists detect only low levels of gaseous-type iron [4, 5, 6]. This implies that it also exists in solid form or a molecular state; however, its identification remains an unresolved task that has been studied for decades. A working hypothesis suggests that interstellar iron combined with carbon molecules and formed molecular chains called iron pseudocarbynes. The spectra of these chains are identical to those of the much more common chains of carbon molecules, whose presence in interstellar space has long been known [6].

In the "Test" experiment, iron particles were identified on the ISS surface as part of fine particulate matter from outer space, which presumably reached the surface as a result of interaction with the electric fields of the station:

1. Electric fields on spacecraft surfaces are formed due to the accumulation of charged particles, such as electrons and ions from the surrounding plasma, on them. If spacecraft surfaces are covered with dielectric materials (e.g., thermal control paints, fluoroplastic), they can accumulate charge, forming an electrical capacitance with the metal body of the spacecraft. Electrons and ions from near-Earth plasma can reach the spacecraft surface and accumulate on it, especially on non-conductive materials (Fig. 3).

Fig. 3. A cotton fabric bundle secured on the painted external surface of the Service Module of the ISS RS

2. Power sources, solar panels, instruments, and thrusters create electric fields.

3. Changes in the near-Earth plasma, for example, when passing through regions with different particle densities, can cause noticeable fluctuations in the surface electric potential and, as a consequence, changes in electric fields [4].

4. Mechanisms of the generation of electric fields and currents on the spacecraft surface upon collision with microparticles:

4.1 A microparticle under the influence of solar UV radiation charges positively due to the photoelectric effect, i.e., electron emission as a result of absorption of UV quanta. The particle charge can reach an order of a thousand electron charges. Currents induced by the negative electric charge flow over the metal surface. Upon contact of the particle with the surface, the particle charge transfers to the metal, and then this space charge dissipates.

4.2. When a microparticle collides with the spacecraft surface, compression of the medium occurs, which causes the appearance of an electric current and an accompanying EMF. The density of the resulting current can reach 10–1000 mA/cm^2. These currents arise in the volume

of the metal and dielectric and can also flow along the opposite side of the metal. Thus, particle impacts on the spacecraft surface lead to the creation of surface currents and electric fields.

As a result of the experiments conducted on the ISS under the "Test" program and the analysis of the sediment, an understanding of the operating environment of orbital objects has been formed, including the presence in the near-space environment of aggressive elements: atomic oxygen, elements of high electron affinity (sulfur, fluorine, chlorine), and other elements of volcanic gases reaching orbit, as well as cosmic sources of influx. Data on the composition of the continuously arriving fine particulate matter on the surface of orbital objects will allow the refinement of the requirements for the quality of spacecraft surfaces in terms of materials, coatings, and protective elements.

Conclusion

The results of the study of the composition of fine particulate matter on the ISS surface demonstrate viable ways of obtaining new data on the Earth's exosphere and outer space. The ISS surface is a unique accumulator of cometary matter in its natural form and the only easily accessible platform for its regular collection. Particles of cometary matter ejected into interplanetary space from the comet nucleus (comet tail) burn up at an altitude of 80–100 km above the Earth. Using the ISS, scientists can regularly obtain factual material for studying cometary matter adsorbed on the ISS surface and, as shown in the "Test" space experiment, delivered to Earth in its natural state. Analysis of fine particulate matter from the surface of orbital stations is a source of information on the state of iron particles and compounds in outer space, as well as magnesium in the Earth's exosphere; furthermore, and based on the results of isotope analysis, it is possible to establish the sources of sediment on the surface of an orbital object. Space debris and massive orbital constellations are collectors and carriers on their surfaces of biological objects, aggressive chemical elements, and radioactive particles that can cause the degradation of station materials, which may also present new potentially hazardous factors accompanying the return of orbital objects to Earth.

REFERENCES

1. Shubralova E. V., Peklevskiy A. V., Prokopovich S. P., Uspenskiy F. A., and Chikirev V. N. Cosmic Research, **63** (2), 29–38 (2025) [in Russian].
2. Zinicovscaia I., Grozdov D., Yushin N., Safonov A., Proshin I., Volkov M., Pryadka A., Belyaev V., Shubralova E., and Tsygankov O., Acta Astronautica **189**, 278–282 (2021).
3. Vasilyak L. M., Shubralova E. V., and Chikirev V. N., Applied Physics, No. 6, 14–19 (2024) [in Russian].
4. Baranov D. G., Gagarin Yu. F., Dergachev V. A., Nymmik R. A., and Yakubovsky E. A., Bulletin of the Russian Academy of Sciences: Physics **69** (6), 832–834 (2005).
5. Baranov D. G., Gagarin Yu. F., Dergachev V. A., Nymmik R. A., and Panasyuk M. I., Cosmic Research **49** (6), 1–8 (2011).
6. Pechersky D. M., Kandinov M. N. Markov G. P., Plyashkevich A. A., Tselmovich V. A., and Sharonova Z. V., Geomagnetism and aeronomy **15** (2), 166–185 (1975).
7. Tsygankov O. S., Grebennikova T. V., Deshevaya E. A., Morozova M. A., Novikova N. D., Polikarpov N. A., Syroeshkin A. V., Shubralova E. V., and Shuvalov V. A., Space equipment and technology, No. 1 (8), 31–41 (2015) [in Russian].

About authors

Vasilyak Leonid Mikhailovich, Doctor of Physical and Mathematical Sciences, Senior Research Assistant, Joint Institute for High Temperatures of the Russian Academy of Sciences (125412, Russia, Moscow, Izhorskaya st., 13, bldg. 2). E-mail: vasilyak@ihed.ras.ru SPIN code: 5623-5167, AuthorID: 19599, ORCID 0000-0001-6982-3038, Scopus 7004886755

Peklevskiy Andrey Viktorovich, Candidate of Physical and Mathematical Sciences, Leading Researcher, Joint Stock Company “Central Research Institute for Machine Building” (141070, Russia, Moscow Region, Korolev, Pionerskaya st., 4). E-mail: 5737@mail.ru SPIN code: 1870-6205

Prokopovich Sergey Pavlovich, Head of Department, Joint Stock Company “Central Research Institute for Machine Building” (141070, Russia, Moscow Region, Korolev, Pionerskaya st., 4). E-mail: prokopovichsp@tsniimash.ru

Chikirev Vladimir Nikolaevich, Chief Specialist, Joint Stock Company “Central Research Institute for Machine Building” (141070, Russia, Moscow Region, Korolev, Pionerskaya st., 4). E-mail: vladch56@yandex.ru AuthorID: 609834

Shubralova Elena Vladimirovna, Chief Specialist, Joint Stock Company “Central Research Institute for Machine Building” (141070, Russia, Moscow Region, Korolev, Pionerskaya st., 4). E-mail: shubralova@mail.ru SPIN code: 2734-5521, AuthorID: 1317404

GENERAL PHYSICS

UDC 537.862 PACS: 41.20.Gz
EDN: VSREWD

Detection of potential electric field induced by a toroid with low frequency current

A. K. Tomilin[1*], I. Misyuchenko[2], and V. S. Vikulin[3]

[1] *Tomsk State University of Control Systems and Radioelectronics, Tomsk, 634050 Russia*
[2] *JSC "Russian Aluminum Management", Moscow, 121096 Russia*
[3] *Macrogroup company, St. Petersburg, 196105 Russia*
[*] *E-mail: aktomilin@gmail.com*

Received 1.09.2025; revised 23.09.2025; accepted 27.04.2026

The article presents the results of experiments on direct measurement of the electric field in the toroid hole with alternating current of 50 Hz. In the first experiment, a shielded charge-sensitive sensor in the form of a metal rod was used. It was found that in the case of traditional single-point grounding, the screen is not equipotential and completely blocks the sensor operation. Forced equipotentiality of the screen is achieved using two-point grounding, and the sensor inside the screen successfully records the alternating electric field. The result of the experiment is explained by the presence of a non-stationary vortex-free vector potential on the toroid axis, which exerts a force effect on free electrons in the metal probe. In the second experiment, a slider rheostat was used. Such a scheme allows us to abandon the grounded screen and the experiment is simplified as much as possible. The conclusions obtained as a result of the experiments complement the idea of the vector potential and its properties and can be used in solving problems of electromagnetic compatibility.

Keywords: generalized electrodynamics, vector potential, magnetic field of a toroid, Aharonov-Bohm effect, electromagnetic compatibility.

DOI: 10.51368/2949-561X-2026-2-10-14

For citation: Tomilin A. K., Misyuchenko I., and Vikulin V. S., Applied Physics, No. 2, 10–14 (2026).

Introduction

Toroidal transformers are often used in electrical and radioelectronic devices. This raises the problem of electromagnetic compatibility of devices and equipment, requiring a detailed study of the generated electric and magnetic fields.

An experiment with a toroidal solenoid (toroid) carrying a current with a frequency of 50 Hz is described in [1]. The toroid winding is enclosed in a solid grounded shield. As a result, a potential electric field was detected and measured by the electrometric method on the axis of the inner hole of the toroid (outside the shielded region). It is shown that this effect is not related to electromagnetic leakage fields. Its origin is explained by the field of the non-stationary vector potential $\mathbf{A}(t)$. The question of the correspondence of the field of vector $\mathbf{A}$ to the Helmholtz decomposition theorem into solenoidal $\mathbf{A}_s$ and potential $\mathbf{A}_p$ components is discussed:

$$\mathbf{A} = \mathbf{A}_s + \mathbf{A}_p \qquad (1)$$

The $\mathbf{A}_p$ component is usually excluded by the Coulomb or Lorentz gauges. However, as it turned out, it possesses certain physical content and paradoxical properties. This coincides with the conclusion made in [2]: "...the vector potential is more important than the electric and magnetic fields. Vector potential fields can generate electric fields in a contactless manner through conducting substances." A similar conclusion is made in [3]. The properties of the $\mathbf{A}_p$ vector field have also been investigated in various works, and the information obtained has been systematized in monographs [4, 5].

The aim of the present study is the direct experimental measurement, by two methods, of the potential electric field in the hole of a toroid with alternating current and outside it, as well as the theoretical explanation of the experimental results.

Note that the methods of measuring the electric field in the present work differ from the method used in [1]. Comparison of the results obtained by different methods allows a conclusion to be drawn about their reliability.

Experiment on measuring the potential electric field by a charge-sensitive sensor

Fig. 1 presents a schematic of the experiment on measuring the electric field in the inner hole of a toroidal solenoid carrying an alternating current with a frequency of 50 Hz. The basis of the solenoid is a laminated steel core shaped as a hollow cylinder with a relative magnetic permeability of 11000. The quasi-static electric field sensor is a conducting steel rod with a resistance of 0.1 Ω, connected to a charge amplifier. The signal of this sensor does not depend on the capacitance of the connecting cables, but only on the sensor's own capacitance and the magnitude of the field acting on it.

The schematic of this experiment differs fundamentally from that described in [1]: here, the toroid is not shielded, whereas the sensor is shielded. The shield is made of a polyvinyl chloride tube with an inner diameter of 50 mm, on the outer surface of which a conductive layer of graphite varnish 20 μm thick is applied. There is an air gap of 20 mm thickness between the sensor and the shielding surface. If the field of the $\mathbf{A}_p$ vector is capable of penetrating through a conductive surface, then the results of experiments with different types of shields should not differ.

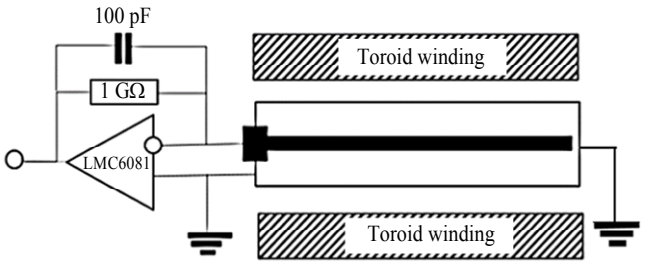

Fig. 1. Schematic of the experiment with a charge-sensitive sensor

Initially, an experiment was conducted with the shield grounded at one point. It showed a complete absence of the sensor signal. When analyzing the reasons for such a result, measurements of the potential difference between the distal and proximal ends of the electrostatic shield were carried out. It was found to be 780 mV. Consequently, such a shield is not equipotential. It is necessary to ensure its equipotentiality. For this purpose, the shield must be grounded at both ends, as shown in Fig. 1. However, with two grounding points of a non-equipotential metal shell, alternating currents will flow through it. To prevent these currents from causing measurement interference, they must be minimized. For this purpose, the shield must be made sufficiently high-resistance (e.g., tens of kiloohms); then the currents flowing in it will be negligibly small, allowing their induction on the sensor to be disregarded.

In the setup used, the toroid height was $h = 0.085$ m, the effective (measured) value of the EMF on the toroid axis $\bar{\varepsilon} = 780$ mV, which corresponds to the expected effective value of the electric field strength:

$$\bar{E} = \frac{\bar{\varepsilon}}{h} = 9.17 \text{ V/m}.$$

Calibration of the probe together with the charge amplifier (CA) was performed by connecting a voltmeter to the grounding circuit. The transfer coefficient was determined as the ratio of the actually measured voltage at the CA output to the voltage applied to the shield ends: $K = 0.03$. When a voltage of 220 V with a frequency of 50 Hz is applied to the toroid winding, a sensor with an equipotential screen and a CA records the effective voltage $\bar{U} = \bar{\varepsilon} = 0.235$ V. Considering the transfer coefficient, this corresponds to the electric field strength $\bar{E}_x = 9.17$ V/m. When the voltage supplied to the toroid was varied using a variable autotransformer (LATR), a linear dependence between the input voltage and the output signal was established.

A sensor located outside the toroid does not register an electric field, which is consistent with numerous measurements using closed loops located entirely outside the hole.

Experiment using a slide rheostat

It is highly desirable to measure the electric field using the simplest possible technical means, avoiding various types of interference and noise. To achieve this goal, a slide rheostat with a resistance of 10 kΩ and a length almost exactly matching the height of the toroid was used. The same toroid as in the first experiment was used in this experiment. The contact point B with the resistive layer changes as the slider moves (Fig. 2).

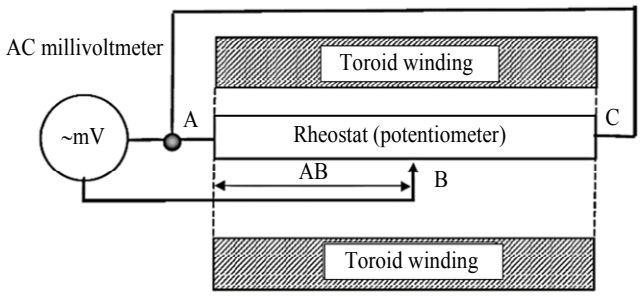

Fig. 2. Schematic of the experiment with a rheostat

If the equipotentiality of the rheostat is ensured by short-circuiting its contacts A and C with a low-resistance conductor, then even under the action of induction on the resistive layer of the rheostat, the potential throughout the entire layer from A to C will be the same. Let us call this technical solution an "equipotential rheostat." Slider B is connected to point A through an AC millivoltmeter. The part of the conductor running from point B to the voltmeter is located inside the toroid. It plays the role of a charge-sensitive probe, as in the first experiment. In this part of the conductor of length $AB = x$, an EMF is induced, which the instrument measures. As the rheostat slider moves, x changes and, accordingly, the measured rms voltage (induction EMF) arising on this section changes. A rheostat with a known nonlinear resistance characteristic $R(x)$ was used in the experiment. The electric field strength E on the toroid axis, calculated using the formula

$$E(x) = \frac{U(x)}{l_0}\frac{R_0}{R(x)}$$

proved to be practically constant and equal to 13 V/m. Here l_0 and R_0 are, respectively, the length and maximum resistance of the rheostat, and $U(x)$ is the measured voltage. As a result, a linear graph of the dependence of the induction EMF on the position of the rheostat slider was obtained (Fig. 3).

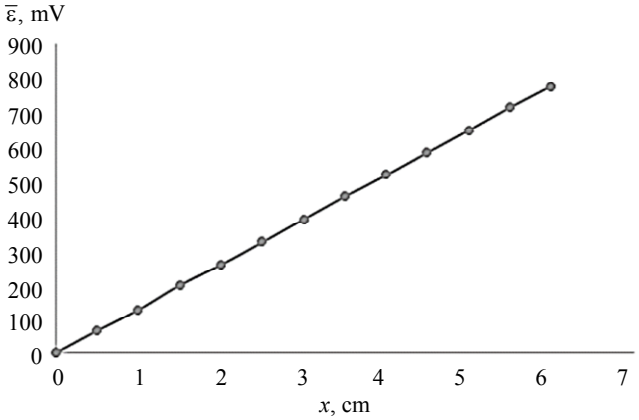

Fig. 3. Dependence of the measured EMF on the length of section AB = x

Thus, both experiments register the presence of a potential electric field on the axis of the toroid through the winding of which an alternating current flows.

Theory

First of all, the question of the origin of the potential electric field on the toroid axis should be answered. This phenomenon cannot be explained by leakage fields around the toroid: at a frequency of 50 Hz, the length of the emitted electromagnetic waves is more than 6000 kilometers; consequently, no noticeable potential difference can arise within the toroid. It is obvious that the cause is related to the non-stationary field of the vector potential, since:

$$\mathbf{E} = -\frac{\partial \mathbf{A}}{\partial t}. \qquad (3)$$

The induction EMF on the x-axis of the toroid "from end to end" is determined by the formula:

$$\varepsilon = \int_0^h E_x dx = -\int_0^h \frac{\partial A_x}{\partial t} dx = -\frac{\partial A_x}{\partial t} h. \qquad (4)$$

Note that here the projection A_x of the potential vector $\mathbf{A}_p$ onto the toroid axis is used,

and it is taken into account that the non-stationary field $E_x(t)$, as follows from experiments, is uniform. In this case, free electrons with charge q move in the metal probe under the action of the force:

$$F_x = qE_x .$$

Since the output voltage of the CA is proportional to the force F_x, the experiment proves the force action of the non-stationary vector potential $\mathbf{A}_p$ on charges. This conclusion allows the well-known Aharonov-Bohm effect [6–11] to be explained, but without the quantum concepts that are often used for this purpose.

With a sinusoidal law of alternating current in the toroid with frequency f, the vector potential changes according to the law:

$$A_x = A_{x(\max)} \cos(2\pi f t). \qquad (5)$$

Substituting (5) into (4), we obtain

$$A_x = \frac{\varepsilon}{2\pi f h} \sin(2\pi f t)$$

then the amplitude of the potential component of vector **A** on the toroid axis can be calculated:

$$A_{x(\max)} = \frac{\overline{\varepsilon}}{\sqrt{2}\pi f h} = 0.0106 \ \text{T}\cdot\text{m}.$$

Here $\varepsilon = \overline{\varepsilon}\sqrt{2}$ is considered.

The monograph [4] outlines the concept of generalized electrodynamics, based on the concept of a four-dimensional vector (quaternion) of the magnetic field $(\mathbf{B}, B^*)$. Such a concept corresponds to the Helmholtz theorem on the decomposition of a field into solenoidal and potential components. The potential component of the magnetic field is determined by the scalar function $B^*(x, y, z, t)$ and is related to the vector potential **A**:

$$\nabla \cdot \mathbf{A} = -B^* . \qquad (6)$$

It is clear that here $\mathbf{A}=\mathbf{A}_p$.

The scalar magnetic field (SMF) is induced, in particular, by a toroidal solenoid (Fig. 4). In the ideal case, the vortex (solenoidal) and potential (scalar) magnetic fields of the toroid are positionally separated: the vortex magnetic field is concentrated inside its winding, and the potential one is concentrated along the axis in the inner hole and is represented by two regions with different signs. In the region of negative SMF, the sources of the potential vector $\mathbf{A}_p$ are located, and in the positive region, the sinks.

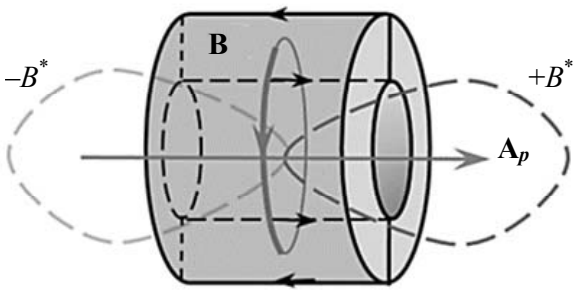

Fig. 4. Magnetic field of a toroidal solenoid

In [3], a system of differential equations of generalized electrodynamics (extended Maxwell's equations) is presented. One of the equations expresses the law of irrotational electromagnetic induction:

$$\nabla \cdot \mathbf{E} = \frac{\partial B^*}{\partial t}, \qquad (7)$$

from which it follows that a non-stationary SMF with induction B^* generates a potential electric field of strength **E**. Note that formula (3) follows from equation (7) taking into account (6). The same monograph presents the results of several experiments confirming the phenomenon of irrotational electromagnetic induction. The experiment described in this article also confirms this phenomenon.

Conclusion

Let us formulate the results obtained in this study:

1. In the first experiment, a potential electric field in the inner hole of a toroid with alternating current was registered using a charge-sensitive sensor. It was shown that in such experiments, it is necessary to ensure the equipotentiality of the electrostatic shield.

2. The phenomenon of penetration of the irrotational vector potential field through an equipotential electrostatic shield has been confirmed, which is important to consider in problems of electromagnetic compatibility.

3. It has been established that in the non-stationary field of the irrotational vector potential, charged particles experience a force action. This result should be considered when interpreting the Aharonov–Bohm effect.

4. In the second experiment, a very simple circuit with a potentiometer was implemented, requiring no grounding. Its advantage lies in the ease of replicating the experiment in order to verify the described phenomenon.

REFERENCES

1. Tomilin A. K., Misyuchenko I., and Vikulin V. S., Applied Physics, No. 5, 5–11 (2024) [in Russian]. https://doi.org/10.51368/1996-0948-2024-5-5-11
2. Lekchaum S. and Daibo M., IEEE Transactions on Applied Superconductivity **30** (4), 1 (2020). https://doi.org/10.1109/TASC.2020.2970918
3. Apel'tsin V. F. and Poletaev A. I., Engineering Journal: Science and Innovations, No. 9, (2013). URL: http://engjournal.ru/catalog/mathmodel/technical/955.html
4. Tomilin A. K. Generalized Electrodynamics. Moscow: Triumph, 2020 [in Russian]. https://doi.org/10.32986/978-5-93673-270-6-2020-04
5. Zohuri B. Scalar Waves. In book: Scalar Wave Driven Energy Applications. Springer: 2019, pp. 443. https://doi.org/10.1007/978-3-319-91023-9_6
6. Aharonov Y. and Bohm D., Physical Review **115**, 485–491 (1959).
7. Peshkin M. and Tonomura A. The Aharonov-Bohm Effekt. Berlin; Heideberg; New York; London; Tokyo; Hong Kong; Springer-Verlag, 1989.
8. Tonomura A. The Quantum World Unveiled by Electron Waves, with a Preface of Chen Ning Yang. World Scientific, Singapore, 1998.
9. Loshak Zh., Applied Physics, No. 2, 5–11 (2003) [in Russian].
10. Afanasyev G. N., Physics of Elementary Particles and Atomic Nuclei **21** (1), 172–250 (1990) [in Russian].
11. Zubkov M. A. and Polikanov M. I., Letters to JETP **23** (57), 461 (1993) [in Russian].

About authors

Tomilin Alexander Konstantinovich, Doctor of Physical and Mathematical Sciences, Professor, Chief Researcher, Tomsk State University of Control Systems and Radioelectronics (634050, Russia, Tomsk, Leninva Ave., 40). E-mail: aktomilin@gmail.com SPIN code: 6546-3766, AuthorID: 452939

Misyuchenko Igoris, Candidate of Technical Sciences, Head of Innovation Department, JSC "Russian Aluminum Management" (121096, Russia, Moscow, Vasilisy Kozhinoy st., 1). E-mail: ruberoid2101@gmail.com

Vikulin Vladimir Stanislavovich, Engineer, Macrogroup company 196105, Russia, Saint Petersburg, Sveaborgskaya st., 12A). E-mail: v_vikulin@mail.ru

PHOTOELECTRONICS

UDC 621 PACS: 85.60.–g
EDN: YLHYGN

Preparation of inks based on colloidal $AgInS_2$ nanocrystals and their application in microplotter printing of photosensitive structures

I. A. Shuklov*, V. V. Lim, I. S. Vlasov, M. A. Troianova, A. Yu. Shalagin, O. V. Vershinina, V. O. Iakovlev, V. S. Popov, and V. V. Ivanov

Moscow Institute of Physics and Technology, Dolgoprudny, Moscow Region, 141701 Russia
** E-mail: shuklov.ia@mipt.ru*

Received 10.12.2025; revised 14.01.2026; accepted 27.04.2026

For the first time, ligand exchange in solution was used to produce inks based on colloidal $AgInS_2$ nanocrystals that are suitable for the fabrication of photosensitive structures. Within this study, a system of stabilizing ligands was identified that allowed the resulting sol in dimethylformamide to remain stable for two weeks without significant agglomeration. FTIR spectroscopy confirmed the completeness of the ligand exchange. Using a microplotter, a photosensitive, photoconductive-type structure was fabricated on gold interdigitated electrodes from the obtained colloidal materials, and its photoelectrical characteristics were measured under illumination with a 405 nm laser.

Keywords: silver indium sulfide, hot injection synthesis, nanocrystals, colloidal quantum dots, thin films.

DOI: 10.51368/2949-561X-2026-2-15-22

For citation: Shuklov I. A., Lim V. V., Vlasov I. S., Troianova M. A., Shalagin A. Yu., Vershinina O. V., Iakovlev V. O., Popov V. S., and Ivanov V. V., Applied Physics, No. 2, 15–22 (2026).

Introduction

Colloidal quantum dots represent a new class of nanomaterials with the possibility of modifying optical properties through the modification of semiconductor nanoparticle sizes [1, 2]. The synthesis of colloidal nanocrystals is typically carried out by hot injection synthesis using long-chain surfactants that act as ligands and stabilizers of the forming nanoparticles. These organic ligands make it possible to obtain nanocrystals with a narrow size distribution and a low-defect surface. Furthermore, they ensure the long-term sedimentation stability of the resulting sols. Unfortunately, these same long-chain ligands act as insulators and do not allow thin layers of colloidal nanocrystals with good conductivity to be obtained. Therefore, to create thin photosensitive conductive films based on colloidal quantum dots (CQDs), the method of layer-by-layer deposition with in-situ ligand exchange is typically used. The replacement of long-chain ligands with short-chain ones directly within the films makes it possible to ensure conductivity while preserving the individuality of the deposited nanoparticles. Thus, both photoresistors and more complex multilayer structures, such as photodiodes, can be obtained. The weak point of this method is the difficulty of obtaining relatively thick films, since the rate of ligand exchange in the film drops sharply with increasing thickness. Also, many exchange reactions occurring during heterophase processing do not allow a high percentage of original ligand replacement to be achieved even in thin films with the thickness of a nanocrystal monolayer (i.e., 5–10 nm) [3, 4]. In recent years, as an alternative approach for obtaining conductive films based on colloidal nanocrystals, the replacement of long-chain ligands in solution

to produce relatively stable colloidal solutions of nanocrystals with short-chain ligands has been proposed [5]. In these colloids, sedimentation stability is typically ensured by electrostatic stabilization [6]. Colloidal solutions of this type make it possible to create thin films possessing photosensitivity and conductivity directly, without additional ligand exchange steps in the films. The deposition can be carried out by spin-coating or by aerosol printing methods. From the point of view of obtaining photosensitive structures, printing is the most attractive method, as it allows for reduced consumption of nanomaterials and precise deposition in selected areas [7].

Monitors and televisions manufactured using quantum dot light-emitting diode (QLED) technology are widely available in electronics chain supermarkets today. Cadmium selenide (CdSe) colloidal quantum dots (CQDs) used in QLED technology as phosphor materials are synthesized according to well-developed and reproducible methods. However, despite the technological advantages, this system has a serious drawback – the environmental toxicity of cadmium compounds. The use of cadmium not only creates additional production safety requirements but also increases the risk of environmental pollution in case of device damage, disposal, or improper recycling. It is this factor that is one of the important constraining factors for the proliferation of solar cells based on cadmium chalcogenide nanocrystals. These environmental limitations stimulate the search for alternative materials and the development of safer technologies [8, 9].

Colloidal nanocrystals of ternary chalcogenides of the ABX_2 type represent a promising class of semiconductor nanomaterials for applications in solar cells, flexible displays, and photosensors [10]. Silver indium disulfide ($AgInS_2$) has a band gap estimated to be 1.87 eV for the bulk material and exciton Bohr radius of 5.5 nm. Thus, as a nanomaterial, it is of interest as a possible alternative to CdSe.

Conductive thin films based on $AgInS_2$ nanocrystals have been obtained by a number of methods, including the layer-by-layer deposition method with exchange for mercaptopropionic acid [11]. Direct deposition methods for $AgInS_2$ sols are poorly studied and are of little suitability for creating photosensitive structures. A previously published study on the creation of a solar cell based on a colloidal $AgInS_2$ solution, designated by the authors as an "ink", also includes annealing of the obtained films at 450 °C in an atmosphere of elemental sulfur [12]. In addition, drop-casting was used as the deposition method, rather than any type of printing. The creation of inks based on $AgInS_2$ nanocrystals with a ZnS shell for creating luminescent labels has been recently published [13]. This system contains stabilizing long-chain ligands, as well as polymethyl methacrylate, which precludes its application in the creation of sensor or photosensitive structures.

To date, we have been unable to find examples in the literature of obtaining inks, i.e., sols of $AgInS_2$ colloidal quantum dots with ligands that allow the creation of thin films with good conductivity. Such "inks" have been developed for a number of nanocrystals of binary chalcogenides, such as PbS [14, 15], CdSe [16], PbSe [17], and HgTe [18]. Within the framework of the presented work, a system suitable for obtaining "inks" based on $AgInS_2$ was found for the first time, and photosensitive resistive-type elements were fabricated using a microplotter.

Materials and methods

Reagents

The following chemicals were used in the synthesis of $AgInS_2$ CQDs without further purification: indium iodide (99 %, Lanhit), sulfur (99.99999 %, Reakhim), 1-decene (90 %, Vekton), 1-dodecanethiol (Acros, 99 %), 2-mercaptoethanol (95 %, Vekton), n-butylamine (95 %, Vekton), silver nitrate (chemically pure, Vekton), hexane (99 % HPLC grade, Macron Fine Chemicals), decane (ultra-high purity, Komponent-Reaktiv), oleic acid (90 %, Vekton), and oleylamine (80–90 %, Acros), which was dried by heating (100 °C) under reduced pressure (1 mbar). Indium stearate was prepared from metallic indium according to the method described in the literature [19]. Silver stearate was synthesized from silver nitrate [20].

Measurement methods

The size, morphology, and structure of the nanoparticles were studied using a JEM-2100 transmission electron microscope (TEM) by JEOL (Japan) at an accelerating voltage of 200 kV. The crystal structure was analyzed by comparing the interplanar distances measured

from the obtained selected area electron diffraction (SAED) images to the values from the database of crystal structures. The optical properties were evaluated by spectrophotometry methods using a JASCO V-770 spectrophotometer (JACSO) and by infrared spectrometry using a Spectrum 100 FTIR spectrometer (PerkinElmer) equipped with a multiple attenuated total internal reflection (MATIR) attachment containing Ge and ZnSe prisms (incidence angle 45°, number of reflections 25). Electrical characteristics were measured using a Keithley 4200A-SCS source measurement unit under illumination from a 405 nm laser. The surface morphology of the thin films was studied using NT-MDT Solver-PRO atomic force microscope in tapping mode.

Obtaining the sulfur precursor

A total of 15.625 mmol (0.5 g) of elemental sulfur was dissolved in 10 mL of 1-decene at a temperature of 185 °C and elevated pressure in a screw-cap thick-walled tube for 1 hour. The resulting dark yellow solution was used as a sulfur precursor in the synthesis of nanocrystals.

Synthesis procedure for $AgInS_2$ CQDs

Silver nitrate (10.2 mg, 0.06 mmol) and indium stearate (57.9 mg, 0.06 mmol) were added to a mixture of 0.4 mL of oleic acid, 0.3 mL of 1-decene, and 3 mL of decane. The resulting mixture was heated under an argon flow at 110 °C until a homogeneous solution formed. The resulting solution was diluted with 27 mL of decane and heated to 150 °C. The sulfur solution in 1-decene (1.56 M, 1.5 mL) was injected at 150 °C. The reaction mixture acquired a brown color during the reaction, and the temperature was maintained at 150 °C. After 60 min, the flask was immersed in an ice bath. $AgInS_2$ nanoparticles were isolated by double reprecipitation. Isolation and purification of the CQDs were carried out by adding a 1:2 methanol:isopropanol mixture followed by centrifugation and redispersion in n-hexane (1.5 mL of the alcohol mixture per 2.5 mL of the reaction mixture for the first precipitation, and 0.6 mL of the alcohol mixture per 1 mL of CQDs in n-hexane for the second precipitation). The nanocrystals were redispersed in n-hexane.

Procedure for preparing $AgInS_2$ CQD inks

Sodium acetate (8.2 mg, 0.1 mmol) was added to a solution of indium iodide in dimethylformamide (0.1 M, 2 mL) under argon and dissolved with stirring. A volume of 0.2 mL of 2-mercaptoethanol was added to the resulting solution to form a homogeneous solution. This solution was mixed with an $AgInS_2$ CQD sol in *n*-octane, with an interface between the hydrophilic and hydrophobic phases being observed. The resulting mixture was stirred for 20 minutes, after which the $AgInS_2$ CQDs transferred from the hydrophobic phase to the hydrophilic phase. The CQDs with a hydrophilic ligand shell were isolated by centrifugation of the mixture for 10 minutes at 3000 rpm in the form of a dark precipitate. The resulting finely crystalline precipitate was redispersed in 2 mL of DMF with the addition of 0.2 mL of n-butylamine. Then, the product was isolated by single reprecipitation by adding tetrachloroethylene (3 mL of TCE per 1 mL of sol in DMF) followed by centrifugation and redispersion in DMF.

Procedure for fabricating a photoresistor based on $AgInS_2$ CQD inks by the drop-casting method

A volume of 50 μL of the $AgInS_2$ CQD solution in dimethylformamide was dropped onto a substrate that had been pre-cleaned from resist using hot (90 °C) n-methylpyrrolidone and rinsed in boiling isopropanol. For more complete evaporation of DMF, the substrate was placed on a hotplate at 70 °C.

Findings and Discussion

Colloidal nanocrystals obtained with a sulfur precursor based on 1-decene were chosen as possible precursors for inks based on $AgInS_2$ nanoparticles [21].

The synthesis of colloidal $AgInS_2$ nanoparticles was carried out according to a modified procedure developed earlier. $AgNO_3$ was used instead of silver stearate as the silver precursor [22]. The synthesis was carried out at 150 °C in decane as the solvent. This procedure allows nanocrystals to be obtained with a ligand shell consisting of oleic acid and oleylamine, which makes it possible to replace the original shell with different types of short-chain ligands. The obtained nanocrystals possess a chalcopyrite crystal structure and exhibit absorption in the visible range (Fig. 1). The as-synthesized $AgInS_2$ nanomaterial has an absorption edge at 700 nm and an excitonic peak maximum at about 580 nm.

TEM micrographs showed that the nanocrystals have the rectangular shapes, including rectangular morphologies with protrusions on one face, and exhibit an average size of about 16 nm (Fig. *2a–b*). Analysis of the size distribution histograms showed that the distribution is relatively narrow with a standard deviation of to 3.98.

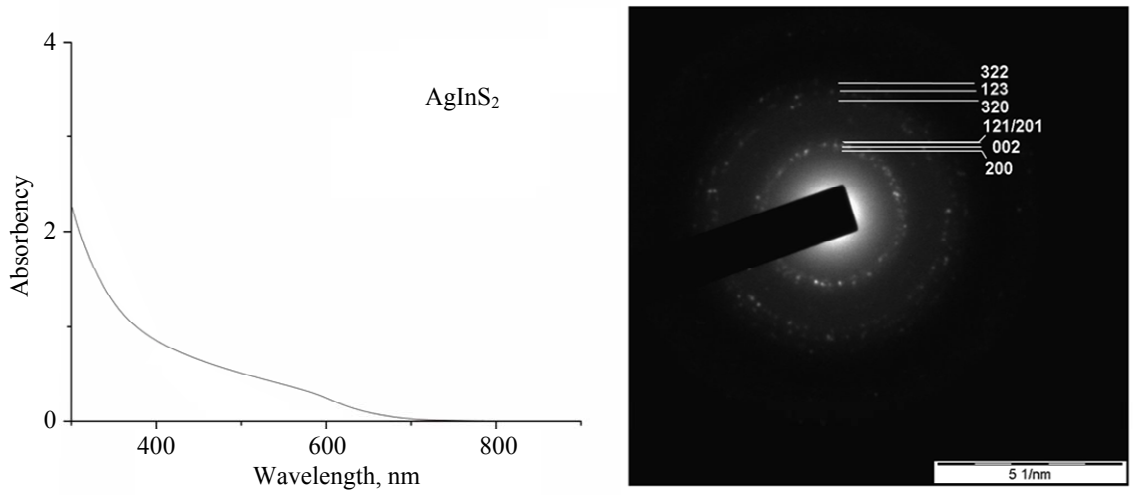

a) *b*)

Fig. 1. $AgInS_2$ CQDs a) Absorption spectrum (visible range, 300–700 nm); b) SAED image

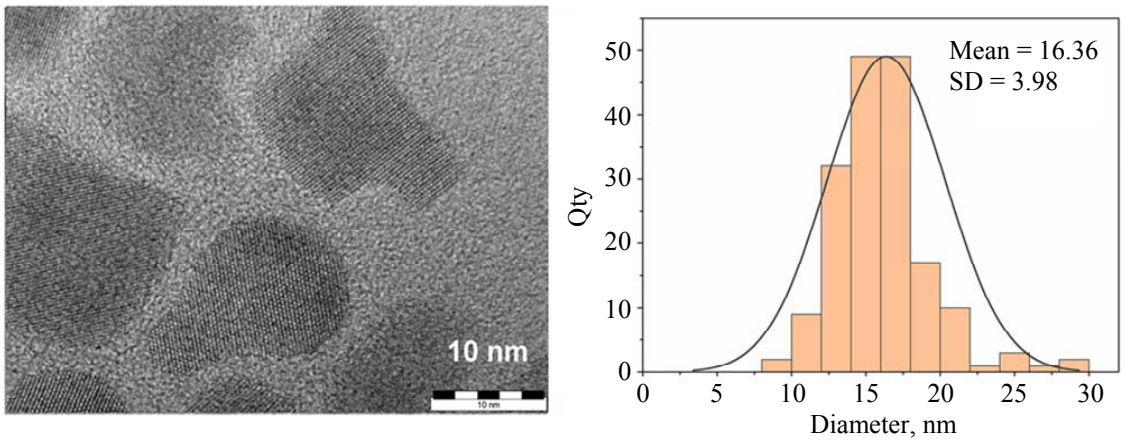

a) *b*)

Fig. 2. a) TEM image and b) size distribution diagram $AgInS_2$ CQDs

To prepare inks from nanocrystals of binary chalcogenides, such as PbS, CdSe, or HgTe, the original ligand shell is usually replaced in dimethylformamide with the halide of the corresponding metal and butylamine. The substitution is usually carried out in a two-phase system, and the efficiency of the ligand exchange can be judged by the transfer of nanoparticles from one phase to another accompanied by a change in their color. For the hydrophobic phase, this corresponds to a change in color from black to colorless, and for the hydrophilic dimethylformamide phase, from colorless to colored.

As already mentioned, the preparation of inks based on colloidal $AgInS_2$ nanocrystals has not been previously described in the literature. In this case, by analogy, either silver halides, or indium halides, or a mixture of both metal salts, can be used. Initial experiments showed that the use of silver halides or mixtures with them for carrying out the substitution is difficult due to their extremely low solubility. Thus, systems based on indium halides were chosen for optimization. Substitution of the original ligand shell with a phase transfer was observed when using indium iodide for the studied nanocrystals with a carboxylate shell. At the same time, the

resulting colloidal solutions exhibited very low stability and degraded almost instantly with the precipitation of $AgInS_2$ nanoparticles, which could not be redispersed back into a stable sol.

For using nanocrystal sols as inks, the key factor is sedimentation stability. The authors achieved long-term colloidal stability using a combination of n-butylamine and 2-mercaptoethanol based on $AgInS_2$ nanocrystals. At the same time, the resulting $AgInS_2$ sols in DMF did not precipitate upon the addition of toluene, as described for analogous sols, which complicated their purification and isolation. The use of tetrachloroethylene as a nonsolvent solved this problem.

TEM investigation showed that the nanocrystals after ligant substitution retain a size close to the original, while acquiring a more spherical shape. SAED showed the retention of the chalcopyrite crystal structure of $AgInS_2$. At the same time, the crystallinity of the sample increases; furthermore, the relative intensity of the reflection from the 122/202 plane increases.

A comparative study of films obtained from the original colloidal $AgInS_2$ nanocrystals and $AgInS_2$ "inks" in dimethylformamide showed that the signals of the original shell consisting of long-chain carboxylate ligands disappear. Thus, the intensity of the signals of stretching vibrations of methylene groups at 2950 cm^{-1} drops fivefold as a result of the substitution of oleate with butylamine, and the signal of the carboxylate ion at 1585 cm^{-1} completely disappears. At the same time, a signal of the carbonyl group of dimethylformamide coordinated on the surface of the nanocrystals appears at 1661 cm^{-1}. Also, a broad peak with a maximum at 4050 cm^{-1}, associated with an intraband transition, appears in the IR region.

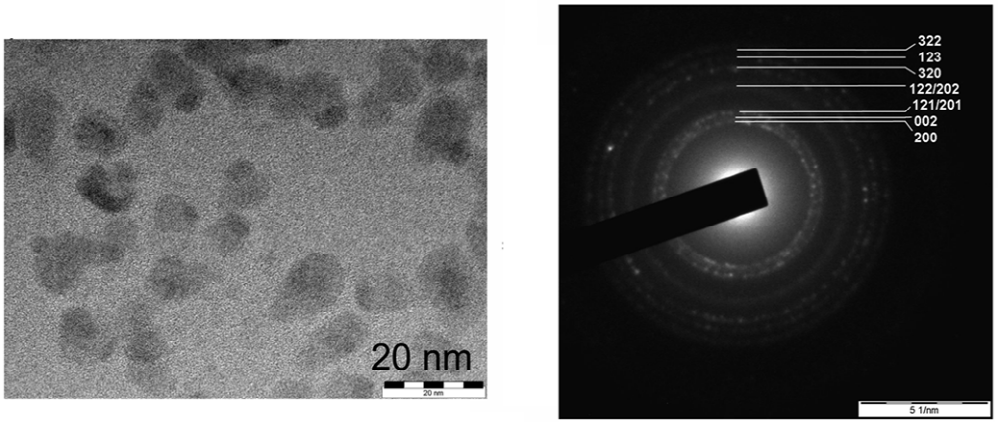

a) *b*)

Fig. 3. $AgInS_2$ CQD "inks" a) TEM image and b) SAED

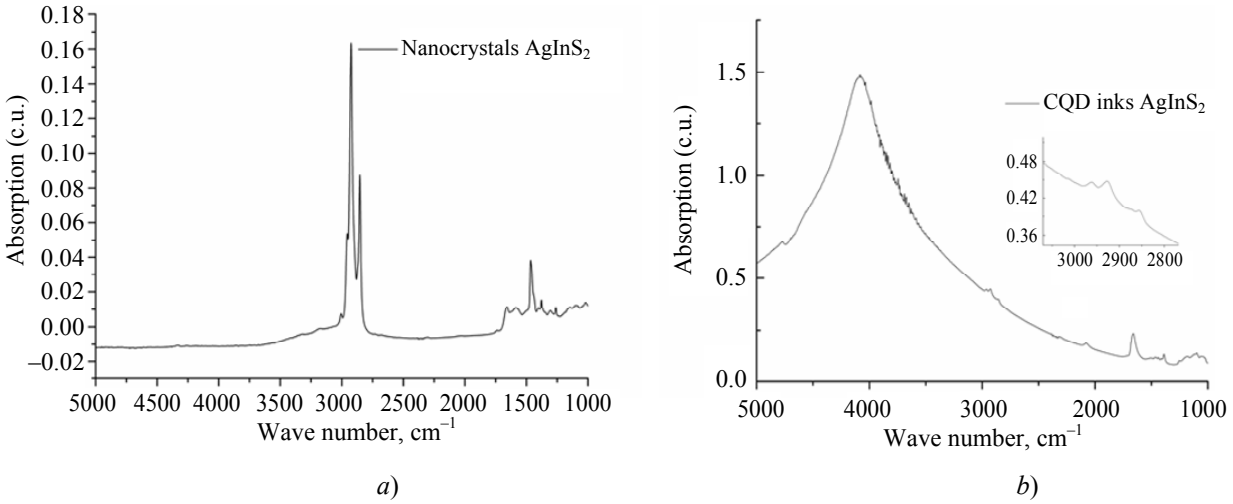

a) *b*)

Fig. 4. a) IR spectra in the range of 5000–1000 cm^{-1}; b) $AgInS_2$ CQD nanoparticles before ligand exchange in solution and after ligand exchange

The process of forming thin-film functional conductive microstructures was performed using a SonoPlot GIX Microplotter II (SonoPlot, Middleton, WI, USA). The microplotter allows the use of picoliter volumes of liquid for depositing functional elements with planar dimensions down to 5 μm. Deposition occurs using a liquid ejection technology via a nozzle that employs ultrasonic vibration generated by a piezoelectric element. In this case, the capillary positioning accuracy reaches 5 μm. A wide range of liquids can be used with this microplotter: the viscosity of functional inks can reach 450 cP, which significantly exceeds similar characteristics of typical inkjet printers operating on the drop-on-demand principle. The formation of elements was carried out using CQD-based inks on silicon oxide substrates with an oxide thickness of 260 nm and gold electrodes prefabricated by lithography. Two types of substrates were fabricated with the following electrode geometries: interdigitated electrodes with gaps between electrodes of 2, 3, and 5 μm, and "bow-tie" electrodes with gaps between electrodes of 30, 20, and 10 μm.

A glass capillary with a nozzle diameter of about 400 μm was chosen for printing. Before printing, the capillary was filled with ink and lowered to a distance of 5–10 μm above the substrate, and a control voltage of 10 V was applied to the piezoelectric element to form contact between the ink and the substrate, after which the control voltage was reduced to 1 V. During the printing process, the capillary moved at a speed of 10 mm/s, and the control voltage applied to the piezoelectric element remained unchanged. Printing was carried out in one and two layers for the interdigitated electrodes, and in one, two, and four layers for the "bow-tie" electrodes. After printing, the samples were dried at room temperature.

Surface investigation using AFM showed a high degree of surface uniformity of the obtained thin-film samples (Fig. 5).

The obtained photoresistor samples showed an increase in conductivity under the action of monochromatic radiation with a wavelength of 405 nm. The maximum photocurrent value at an incident radiation power density of 0.9 mW/mm^2 was 0.18 pA, with a dark current of 0.01 pA (Fig. 6), which provides a sensitivity of 0.03 μA/W.

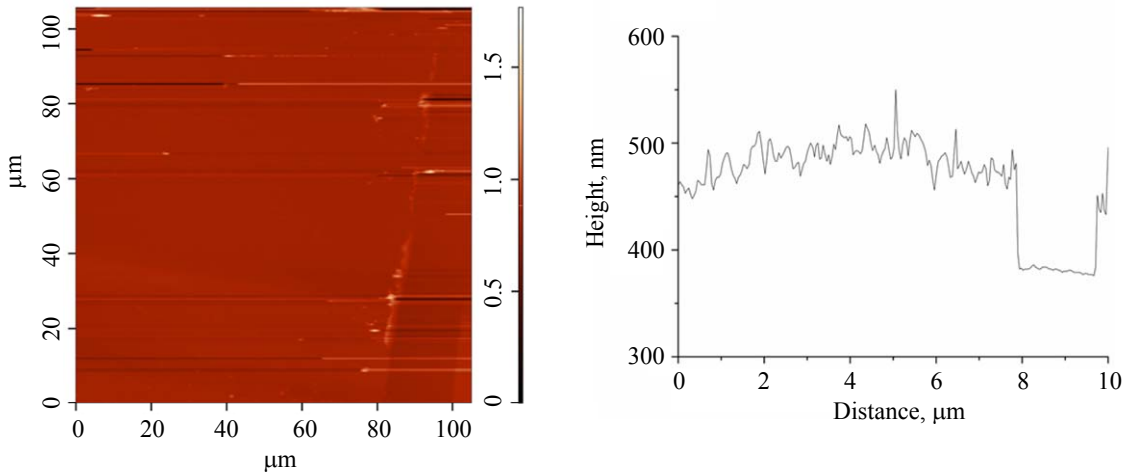

a) *b*)

Fig. 5. Surface image and film cross-section profile obtained by depositing $AgInS_2$ CQD inks

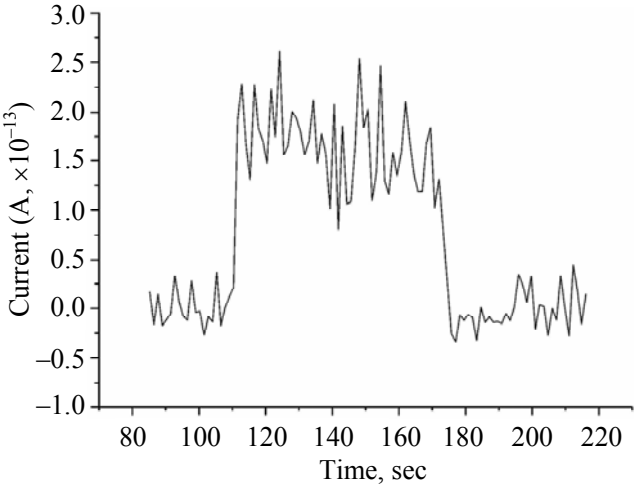

Fig. 6. Typical dependence of current on time when switching on and off illumination from a 405 nm source

Conclusions

For the first time, inks for direct printing of photosensitive structures were obtained based on colloidal $AgInS_2$ nanocrystals. For this purpose, a new method for the in-solution exchange of long-chain ligands for short-chain ones was developed for $AgInS_2$ nanoparticles. It was demonstrated that $AgInS_2$ nanoparticles with this type of ligand shell are highly suitable for ligand exchange aimed at ink formulation. We established that the carboxylate ligand shell allows the required ligand exchange to be carried out efficiently and completely for produce inks. The obtained inks were deposited using a microplotter onto interdigitated electrodes, resulting in the fabrication of a photosensitive structure of the photoresistive type, which showed a clear photoresponse under exposure to monochromatic radiation with a wavelength of 405 nm.

The research is supported by the Ministry of Science and Higher Education of the Russian Federation (Goszadaniye) 075-03-2025-662 at 17.01.2025 (project No. FSMG-2024-0009).

REFERENCES

1. Ponomarenko V. P., Popov V. S., Shuklov I. A., Ivanov V. V., and Razumov V. F., Russ. Chem. Rev. **93** (4), RCR5113 (2024).
2. Shuklov I. A. and Razumov V. F., Russ. Chem. Rev. **89** (3), 379 (2020).
3. Liu M., Tang G., Liu Y., and Jiang F.-L., The Journal of Physical Chemistry Letters **15** (7), 1975–1984 (2024).
4. Shuklov I. A., Dyomkin D. V., Milenkovich T., Dubrovina N. V., Vershinina O. V., Ivanov V. V., and Razumov V. F., Nanoscience and Technology: An International Journal **16** (4), (2025).
5. Aqoma H. and Jang S.-Y., Energy Environ. Sci. **11** (6), 1603–1609 (2018).
6. Zheng S., Chen J., Johansson E. M. J., and Zhang X., iScience **23** (11), (2020).
7. Xiang C., Wu L., Lu Z., Li M., Wen Y., Yang Y., Liu W., Zhang T., Cao W., Tsang S.-W., Shan B., Yan X., and Qian L., Nature Communications **11** (1), 1646 (2020).
8. Chakraborty D., Ethiraj K. R., Chandrasekaran N., and Mukherjee A., Environmental Pollution **270**, 116049 (2021).
9. Sharma V. K., McDonald T. J., Sohn M., Anquandah G. A. K., Pettine M., and Zboril R., Chemosphere **188**, 403–413 (2017).
10. Liu Y., Gao Y., Yang Q., Xu G., Zhou X., Shi G., Lyu X., Wu H., Liu J., and Fang S., Angewandte Chemie International Edition **62**, e202300396 (2023).
11. Cai C., Zhai L., Ma Y., Zou C., Zhang L., Yang Y., and Huang S., Journal of Power Sources **341**, 11–18 (2017).
12. Peng S., Zhang S., Mhaisalkar S. G., and Ramakrishna S., Physical Chemistry Chemical Physics **14** (24), 8523–8529 (2012).
13. Kumar P., Jin L., Selopal G. S., Abdelkarim O., Liu J., Barba D., Yurtsever A., Wang Z. M., and Rosei F., Nano Materials Science, (2024). In press. https://doi.org/10.1016/j.nanoms.2024.10.005.
14. Wang H., Pinna J., Romero D. G., Di Mario L., Koushki R. M., Kot M., Portale G., and Loi M. A., Advanced Materials **36**, 2311526 (2024).
15. Yuan M., Hu H., Wang Y., Xia H., Zhang X., Wang B., He Z., Yu M., Tan Y., Shi Z., et al., Small **18**, 2205356 (2022). https://doi.org/10.1002/smll.202205356.
16. Tang H., Jia S., Ding S., Liu P., Ma J., Xiao X., Qu X., Liu H., Yang H., Xu B., et al., ACS Applied Electronic Materials **3**, 3005–3014 (2021). https://doi.org/10.1021/acsaelm.1c00210.
17. Yuan M., Hu H., Wang Y., Xia H., Zhang X., Wang B., He Z., Yu M., Tan Y., and Shi Z., Small **18** (48), 2205356 (2022).

18. Martinez B., Ramade J., Livache C., Goubet N., Chu A., Gréboval C., Qu J., Watkins W. L., Becerra L., Dandeu E., et al., Advanced Optical Materials **7**, 1900348 (2019). https://doi.org/10.1002/adom.201900348.
19. Dou Q. and Ng K. M., Powder Technology **301**, 949–958 (2016).
20. Malik W. U., Jain A. K., and Jhamb O. P., Journal of the Chemical Society A: Inorganic, Physical, Theoretical, No. 0, 1514–1517 (1971).
21. Shuklov I. A., Seraya A. V., Shalagin A. Y., Lim V. V., Milenkovich T., Vershinina O. V., and Ivanov V. V., Applied Physics, No. 2, 21 (2025).
22. Shuklov I. A., Milenkovich T., Majorova A. V., Vershinina O. V., Ivanova V. A., Pavlova V. D., and Popov V. S., Journal of Communications Technology and Electronics **70** (2), 61 (2025).

About authors

Shuklov Ivan Alexeyevich, Senior Researcher, Associate Professor, Dr. rer. nat., Moscow Institute of Physics and Technology (141701, Russia, Moscow Oblast, Dolgoprudny, Institutsky lane 9). E-mail: shuklov.ia@mipt.ru SPIN code: 4060-7233, AuthorID: 1146575

Lim Vladimir Valerievich, Technician, Bachelor, Moscow Institute of Physics and Technology (141701, Russia, Moscow Oblast, Dolgoprudny, Institutsky lane 9). E-mail: lim.vv@mipt.ru

Vlasov Ivan Sergeyevich, Junior Researcher, Moscow Institute of Physics and Technology (141701, Russia, Moscow Oblast, Dolgoprudny, Institutsky lane 9). E-mail: vlasov.is@mipt.ru SPIN code: 7291-5090

Troianova Margarita Alexandrovna, Technician, Bachelor, Moscow Institute of Physics and Technology (141701, Russia, Moscow Oblast, Dolgoprudny, Institutsky lane 9). E-mail: troianova.ma@mipt.ru

Shalagin Alexander Yurievich, Technician, Bachelor, Moscow Institute of Physics and Technology (141701, Russia, Moscow Oblast, Dolgoprudny, Institutsky lane 9). E-mail: shalagin.au@mipt.ru SPIN code: 9769-2552

Vershinina Olesya Valerievna, Junior Researcher, Postgraduate Student, Moscow Institute of Physics and Technology (141701, Russia, Moscow Oblast, Dolgoprudny, Institutsky lane 9). E-mail: seraia.ov@phystech.edu

Iakovlev Viktor Olegovich, Junior Researcher, Postgraduate Student, Moscow Institute of Physics and Technology (141701, Russia, Moscow Oblast, Dolgoprudny, Institutsky lane 9). E-mail: iakovlev.vo@mipt.ru SPIN code: 3324-6931

Popov Viktor Sergeyevich, Head of Laboratory, Leading Researcher, Associate Professor, Candidate of Chemical Sciences, Moscow Institute of Physics and Technology (141701, Russia, Moscow Oblast, Dolgoprudny, Institutsky lane 9). E-mail: popov.vs@mipt.ru SPIN code: 1128-2332, AuthorID: 625948

Ivanov Viktor Vladimirovich, Chief Researcher, Director of the Institute of Quantum Technologies, Professor, Doctor of Physical and Mathematical Sciences, Corresponding Member Russian Academy of Sciences, Moscow Institute of Physics and Technology (141701, Russia, Moscow Oblast, Dolgoprudny, Institutsky lane 9). E-mail: Ivanov.vv@mirt.ru SPIN code: 1856-3914, AuthorID: 19128

PHOTOELECTRONICS

UDC 621.383 PACS: 85.60.–q
EDN: SJAUCB

Dependence of photosignal decay in colloidal HgTe quantum dot based photoresistors on preparation conditions

V. O. Yakovlev[1], T. V. Koroleva[1], K. T. Khakimov[1], O. A. Saptsova[1], A. A. Koronnov[1], O. V. Vershinina[1], A. G. Medvedev[1], V. P. Ponomarenko[1,2], and V. S. Popov[1,2*]

[1] *Moscow Institute of Physics and Technology, Moscow Region, Dolgoprudny, 141701 Russia*
[2] *RD&P Center ORION, JSC, Moscow, 111538 Russia*
[*] *E-mail: popov.vs@mipt.ru*

Received 25.12.2025; revised 3.03.2026; accepted 27.04.2026

This paper examines the influence of colloidal quantum dot synthesis conditions on the number and types of surface states, which in turn determine the response time of photosensors based on them. It is shown that replacing ethanedithiol with β-mercaptoethanol improves the response time of HgTe CQD-based photoresistors by three orders of magnitude.

Keywords: photosensor, colloidal quantum dots, CQDs, surface states, mercury telluride.

DOI: 10.51368/2949-561X-2026-2-23-27

For citation: Yakovlev V. O., Koroleva T. V., Khakimov K. T., Saptsova O. A., Koronnov A. A., Vershinina O. V., Medvedev A. G., Ponomarenko V. P., and Popov V. S., Applied Physics, No. 2, 23–27 (2026).

Introduction

Photosensorics based on colloidal quantum dots (CQD) is one of the most dynamically developing areas of infrared photoelectronics [1, 2]. Photosensitive elements of resistive and barrier types based on colloidal quantum dots are used both for single photosensitive elements and the formation of matrix photoreceiving devices for the short- and medium-wave IR-ranges [3]. The sensitive layers in such photosensors are based on consolidated layers made by a liquid method from sols of semiconductor nanocrystals, mainly lead sulfide and mercury telluride. With this approach, the transfer of carriers in the resulting polycrystalline nanostructured layers proceeds primarily by a hopping mechanism. The surface of nanocrystals in layers formed by chemical methods contains a large number of different functional groups and uncompensated bonds, resulting in the appearance of surface states. The issues of response speed in photosensors based on CQDs play an important role due to the large surface area of quantum-confined materials and a more difficult-to-control environment surrounding the nanocrystals during the formation of consolidated films. The study of the effect of surface conditions on the sensitivity and response speed of photosensors during the targeted modification of CQD surfaces and their layers is of great importance for the development of methods for the formation of photosensitive layers. The results of studies of the effect of traps presented in the literature are usually focused on the study of attenuation curves in photoresistors [4, 5], photoluminescence, [6, 7] or pump-probe spectroscopy[8] when varying ligands in PbS CQDs, at the same time, sufficient attention has not been paid to other CQDs, and the influence of the synthesis conditions of the nanocrystals themselves has not been considered in the literature.

The purpose of this work is to study the changes in surface states when varying the methods of CQD synthesis and post-synthetic treatment of the HgTe QCD surface by studying the decay curves of the photoelectric signal in photoresistors based on HgTe QCDs.

1. HgTe CQDs synthesis and the fabrication of layers based on them

Synthesis of HgTe CQDs

The HgTe CQD synthesis was carried out according to the published method [9] using the

complex compound $NH_4[HgCl_2(SCN)]$ as a mercury precursor.

Photoresistive structures were manufactured in two stages. The first stage is substrate activation, and the second stage is the successive layer-by-layer formation of the photoresistive structure. Both stages involve using the same solution for activator and ligand exchange: a solution of ethanedithiol (EDT) in hydrochloric acid and isopropanol (HCl:EDT:IPA, 1:1:20 by vol.) or a β-mercaptoethanol (β-ME) solution in hydrochloric acid and isopropanol (HCl:β-ME:IPA, 1:1:20 by vol.).

Methods

Fourier-transform IR spectra were obtained using a Spectrum 100 FTIR spectrometer (Perkin-Elmer, USA) equipped with an attenuated total reflectance (ATR) accessory. High-resolution images were obtained using a JEM-2100 transmission electron microscope (JEOL, Japan).

2. Method for studying photoelectric signal decay curves

The study of photocurrent decay processes is one of the classic tools for studying surface states in photoconductive layers of semiconductors [9]. Depending on the type of trap and the energy level created by it, the trapped carriers return after some time to the valence band or conduction band.

Since the photocurrent is proportional to the number of charge carriers [10], the expression for the current decay over time is described by the following expression [11]:

$$I_{\Phi} = I_{\Phi 0} e^{-\frac{t}{\tau}},$$

where $I_{\Phi 0}$ is the photocurrent at saturation, and τ is the lifetime of the carrier.

The signal is divided by the amplitude of the photocurrent to analyze the multistage relaxation. The threshold is determined as follows:

$$I_{\text{thr}} = I_{\min} + \gamma\left(I_{\max} I_{\min}\right),$$

where $I_{\min}$ and $I_{\max}$ is the minimum and maximum values of the photocurrent in the selected interval.

Coefficient γ sets the relative position of the threshold level within the full dynamic range of the photovoltage and thus defines the boundary between different stages of the relaxation process. In the method used, the value is selected in the following form γ:

$$\gamma = \frac{1}{e^n},$$

where e is the base of natural logarithms, and the exponent factor n is a whole or a fractional number set by the user depending on the expected number and extent of relaxation components. When $n = 1$, the threshold corresponds to the level $1/e$ of the full amplitude range, which is a characteristic value for single-exponential decay and is naturally associated with the determination of the time constant. As the exponent factor increases, the threshold value consistently shifts to the area of lower photocurrents, which allows the identification of slower relaxation stages.

This method of setting thresholds ensures a physically reasonable signal division into sections, each of which corresponds to a certain time range and, respectively, the dominant relaxation mechanism. As a result, each selected area can be analyzed independently using its own exponential approximation, which increases the accuracy of determining the time constants and amplitudes of individual components, while reducing the mutual effect of fast and slow processes when processing the whole signal together.

A running-median smoothing is used to reduce the noise impact and single outliers. At the same time, a combined mode is also possible in which the initial stage of the time series is preserved without filtration and the subsequent part is subject to smoothing. This allows one to preserve the initial changes in photovoltage and simultaneously increase the analysis stability of the slow relaxation area.

The approximation of the relaxation part of the photoresponse is carried out using a model of the sum of decaying exponential components. In general, the model is written as follows:

$$I_{\text{model}}(t) = I_{\text{т}} + \sum_{k=1}^{N} A_k \exp\left(-\frac{t - t_s}{\tau_k}\right),$$

Where I_{d} is the dark current, A_k is the amplitude of individual relaxation components, τ_k represents the time constants corresponding to them, N is the number of exponential summands and t_s is the

effective time shift of the relaxation beginning. At the same time, it is assumed that $A_k \geq 0$, which ensures a physically reasonable interpretation of the results.

The results of processing are the numerical values τ of sections of the photovoltage attenuation curve, as well as a set of time dependences including the initial signal and approximating curves.

3. Discussion of the results

In this work, HgTe colloidal quantum dots with an exciton absorption peak in the range from 2.13 to 3.16 μm were synthesized (Fig. 1).

According to the transmission electron microscopy data, HgTe nanocrystals were synthesized in all cases (Fig. 2). Photoresistor layers based on HgTe CQDs had a thickness of about 80–90 nm according to atomic-force microscopy data.

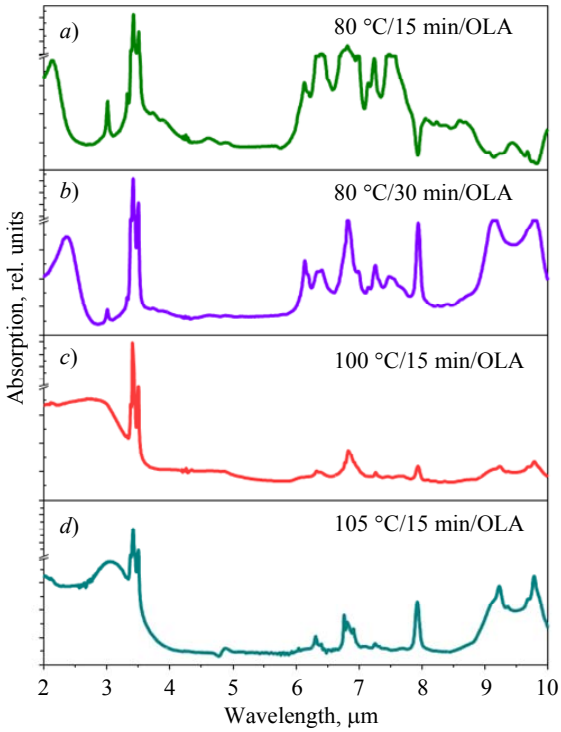

Fig. 1. Fourier-transform IR spectra of HgTe CQDs synthesized under different modes (OLA: oleylamine)

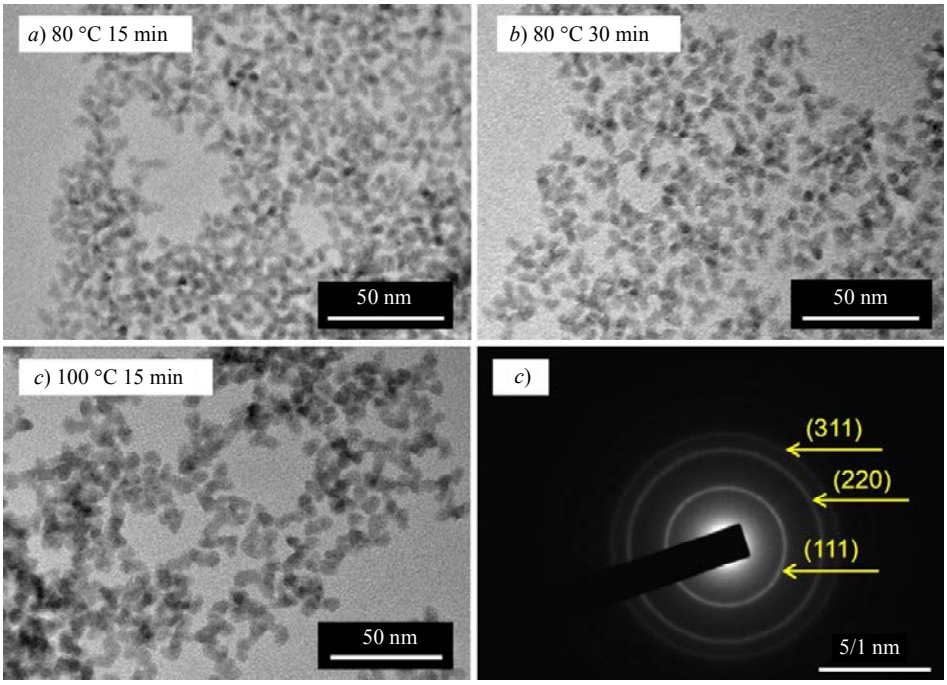

Fig. 2. (a–c) Transmission electron microscopy of HgTe CQDs obtained under different conditions; (d) selected-area electron diffraction pattern

The study of the decay curves showed that the number and type of surface states vary depending on the synthesis conditions of the CQDs and the type of ligand used for the surface modification of the photosensitive layers (Fig. 3).

Since the lifetime characterizes the energy of the surface state (namely, deeper traps correspond to longer lifetimes) [12], it can be concluded that depending on the quantum dot and the used ligand, surface states that are significantly different in terms of energy appear on its surface.

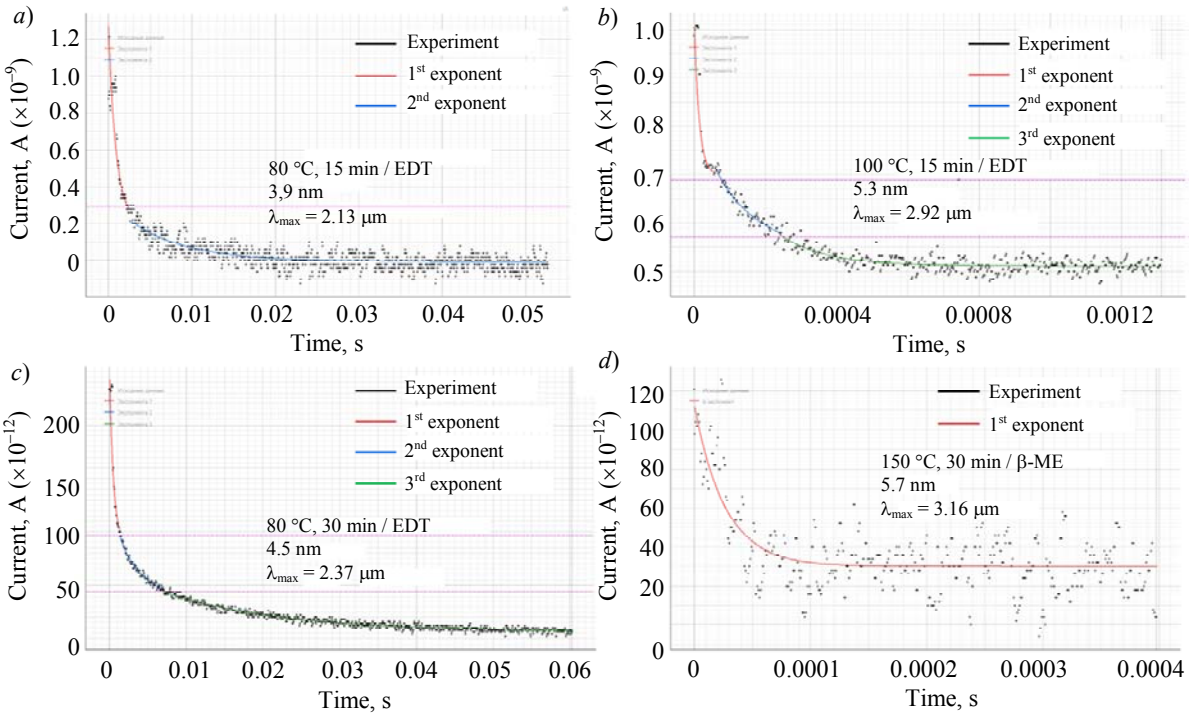

Fig. 3. Decay curves of the photosignals of photoresistors based on HgTe CQDs obtained under different conditions (temperature and synthesis time: a) 80 °C, 15 min, b) 100 °C, 15 min, c) 80 °C, 30 min) and using different ligands during surface modification: b) ethanedithiol (EDT) and d) – β-mercaptoethanol (-ME)

For HgTe CQDs with subsequent exchange by ethanedithiol, when the CQD size changes from 3.9 nm to 4.5 nm, the surface states are preserved, which are characterized by $\tau \sim 0.0002$ s and $\tau \sim 0.003$ s, while a new type of surface states is added with $\tau \sim 0.02$ s. When changing the CQD size from 4.5 nm to 5.3 nm, only those surface states are preserved that are characterized with $\tau \sim 0.02$ s, and simultaneously, new surface states occur with $\tau \sim 0.08$ s and $\tau \sim 0.003$ s (Fig. 4).

The use of β-mercaptoethanol instead of ethanedithiol for ligand exchange at a close quantum dot size (5.3 and 5.7 nm) drastically alters the surface states: instead of three types with $\tau \sim 0{,}02$ s, $\tau \sim 0.08$ s and $\tau \sim 0.003$ s, only one type with $\tau \sim 0.00001$ s is observed (Fig. 4).

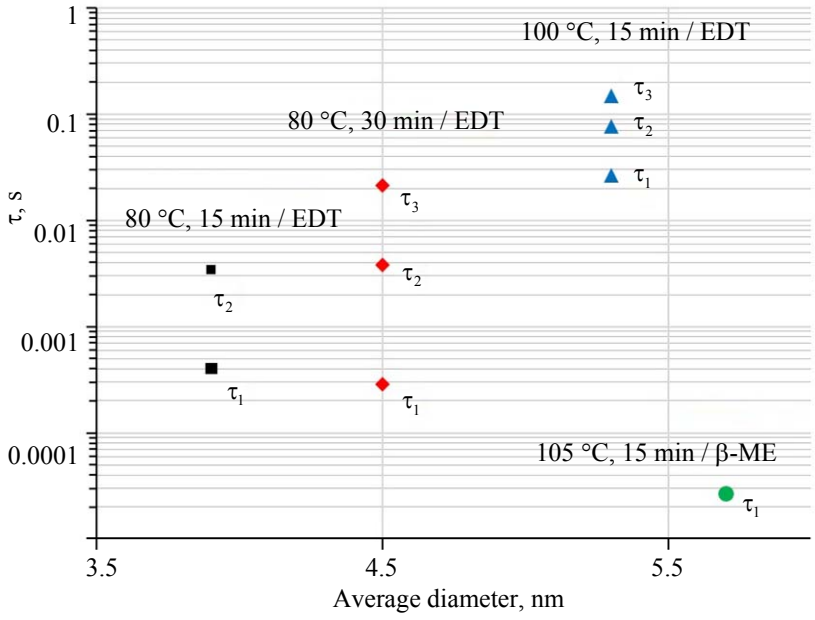

Fig. 4. τ values obtained during the processing of decay curves of the photoelectric signals of photoresistors based on HgTe CQDs obtained under different conditions (temperature and synthesis time: 80 °C, 15 min, 100 °C, 15 min, 80 °C, 30 min) and using different ligands during surface modification: ethanedithiol (EDT) and β-mercaptoethanol (-ME)

Conclusion

The analysis of the photoresponse decay of photoresistors based on HgTe CQDs, obtained while varying the synthesis parameters and the size of the nanocrystals, shows the existence of different types of surface states. The use of β-mercaptoethanol as a ligand exchange allows one to reduce the number of surface states from three types to one. This surface state is characterized by the shortest lifetime found in this paper, equal to 10 μs, thus ensuring a fast response speed of the photosensor.

This work was supported by the Ministry of Science and Higher Education of the Russian Federation (project No. FSMG-2025-0024).

REFERENCES

1. Popov V. S., Ponomarenko V. P., and Popov S. V., J. Comm. Tech. Electron. **69** (4–6), 219–226 (2024).
2. Ponomarenko V. P., Popov V. S., Shuklov I. A., Ivanov V. V., and Razumov V. F., Russ. Chem. Rev. **93** (4), RCR5113 (2024).
3. Popov V. S., Ponomarenko V. P., Dirochka A. I., and Popov S. V., J. Comm. Tech. Electron. **70** (1), 21–27 (2025).
4. Konstantatos G. and Sargent E. H., Appl. Phys. Lett. **91**, 1 (2007).
5. Gong W., Wang P., Deng W., Zhang X., An B., Li J., Sun Z., Dai D, Liu Z., Li J., Zhang Y., ACS Appl. Mater. Interfaces **14**, 25812 (2022).
6. Xia Y., Chen W., Zhang P., Liu S., Wang K., Yang X., Tang H., Lian L., He J., Liu X., Liang G., Tan M., Gao L., Liu H., Song H., Zhang D., Gao J., Wang K., Lan X., Zhang X., Müller-Buschbaum P., Tang J., and Zhang J., Adv. Funct. Mater. **30**, 2000594 (2020).
7. Liu X., Fu T., Liu J., Wang Y., Jia Y., Wang C., Li X., Zhang X., and Liu Y., ACS Appl. Mater. Interfaces **1**4, 14274 (2022).
8. Bakulin A. A., Neutzner S., Bakker H. J., Ottaviani L., Barakel D., and Chen Z., ACS Nano **7**, 8771 (2013).
9. Koroleva T. V., Medvedev A. G., Khakimov K. T., Yakovlev V. O., Saptsova O. A., Koronnov A. A., Chemakina Y. A., Asnachev D. D., Vershinina O. V., Ponomarenko V. P., and Popov V. S., Optical Materials **175**, 118029 (2026).
10. Bube R. Photoconductivity of Solids. NY-London: John Wiley & Sons, 1960.
11. Le B. Q., Van T. N., Quang D. T., Le Dinh V., Van T. P., and Kim N. C. T., J. Semicond. **46**, 072101 (2025).
12. Konstantatos G., Levina L., Fischer A., and Sargent E. H., Nano Lett. **8**, 1446 (2008).

About authors

Yakovlev Viktor Olegovich, Junior Researcher, Moscow Institute of Physics and Technology (141701, Russia, Moscow Region, Dolgoprudny, Institutsky Per., 9). E-mail: iakovlev.vo@mipt.ru SPIN code: 3324-6931, AuthorID: 1290912, ORCID 0009-0009-3507-082X

Koroleva Taisiya Viktorovna, Junior Researcher, Moscow Institute of Physics and Technology (141701, Russia, Moscow Region, Dolgoprudny, Institutsky Per., 9). E-mail: koroleva.tv@mipt.ru SPIN code: 6991-6170, AuthorID: 1292280, ORCID 0000-0003-0792-1948

Khakimov Karim Timurovich, Junior Researcher, Moscow Institute of Physics and Technology (141701, Russia, Moscow Region, Dolgoprudny, Institutsky Per., 9). E-mail: khakimov.kt@mipt.ru SPIN code: 8812-6012, AuthorID: 1209525, ORCID 0000-0001-8133-6128

Saptsova Olga Alexandrovna, Junior Researcher, Moscow Institute of Physics and Technology (141701, Russia, Moscow Region, Dolgoprudny, Institutsky Per., 9). E-mail: saptsova.oa@mipt.ru SPIN code: 3710-5884, AuthorID: 1323937, ORCID 0009-0008-5445-4629

Koronnov Alexey Alexeyevich, Candidate of Technical Sciences, senior research scientist Moscow Institute of Physics and Technology (141701, Russia, Moscow Region, Dolgoprudny, Institutsky Per., 9). E-mail: koronnov.aa@mipt.ru SPIN code: 9854-4380, AuthorID: 116157, ORCID 0000-0001-6046-3400

Vershinina Olesya Valerievna, Junior Research Assistant, graduate student, Moscow Institute of Physics and Technology (141701, Russia, Moscow Region, Dolgoprudny, Institutsky Per., 9). E-mail: seraia.ov@phystech.edu

Medvedev Alexander Gennadyevich, Candidate of Chemical Sciences, Deputy Head of the Laboratory, Senior Researcher, Moscow Institute of Physics and Technology (141701, Russia, Moscow Region, Dolgoprudny, Institutsky Per., 9). E-mail: medvedev.ag@mipt.ru SPIN code: 3699-6664, AuthorID: 822022, ORCID 0000-0002-6762-004X

Ponomarenko Vladimir Pavlovich, Doctor of Physical and Mathematical Sciences, Chief Designer, Head of Department, Professor Moscow Institute of Physics and Technology (141701, Russia, Moscow Region, Dolgoprudny, Institutsky Per., 9); RD&P Center ORION, JSC (111538, Russia, Moscow, Kosinskaya st., 9). E-mail: 2392325@gmail.com SPIN code: 6882-8721, AuthorID: 171358

Popov Viktor Sergeevich, Candidate of Chemical Sciences, Head of Laboratory, Leading Researcher, Associate Professor, Moscow Institute of Physics and Technology (141701, Russia, Moscow Region, Dolgoprudny, Institutsky Per., 9); RD&P Center ORION, JSC (111538, Russia, Moscow, Kosinskaya st., 9). E-mail: popov.vs@mipt.ru SPIN code: 1128-2332, AuthorID: 625948, ORCID 0000-0002-0962-9775

PHOTOELECTRONICS

UDC 621.315.5:621.383 PACS: 85.30.-z, 85.60.-q
EDN: TLQEOJ

Microdefects influence on leakage currents and noise of silicon photodiodes

K. O. Boltar[1,2], M. N. Vildyaeva[1], S. S. Demidov[1], E. A. Klimanov[1,3*], D. S. Konorev[1], E. A. Makarova[1], D. S. Molchanov[1], K. A. Popov[1], V. V. Poluneev[1], and A. A. Zhukovich-Gordeeva[1]

[1] *RD&P Center ORION, JSC, Moscow, 111538 Russia*
[*] *E-mail: klimanov3@mail.ru*
[2] *Moscow Institute of Physics and Technology, Moscow Region, Dolgoprudny, 141701 Russia*
[3] *MIREA – Russian Technological University, Moscow, 119454 Russia*

Received 27.03.2026; revised 7.04.2026; accepted 27.04.2026

Microdefects causing leakage currents and noise in the p^+–n junctions of silicon photodiodes were investigated. It was established that the tunnel component of dark currents is caused by local defects in the oxide and impurity precipitates in the space charge region of the p–n junction. The tunnel currents leads to the generation of noise with a wide spectrum, including "burst" noise.

Keywords: silicon photodiode, microdefects, tunnel currents, current-voltage characteristics.

DOI: 10.51368/2949-561X-2026-2-28-34

For citation: Boltar K. O., Vildyaeva M. N., Demidov S. S., Klimanov E. A., Konorev D. S., Makarova E. A., Molchanov D. S., Popov K. A., Poluneev V. V., and Zhukovich-Gordeeva A. A., Applied Physics, No. 2, 28–34 (2026).

Introduction

One of the main requirements for photodiodes (PhDs) used in photoreceiving devices is a low noise level, which requires reducing dark currents and excluding excess noise in the low-frequency range.

The manufacturing cycle of silicon photodiodes includes a number of thermal operations (oxidation, boron and phosphorus diffusion, low-temperature annealing), during which the samples are contaminated with metal impurities, and local defects form in the oxide, as well as oxygen and impurity precipitates in the silicon bulk. [1–3]. The specified defects can lead to the formation of local n^+-channels in p^+–n junctions and defects on the silicon surface and in its bulk causing leakage currents – "soft" current-voltage characteristics [4], which results in an increase in photodiode noise, including low-frequency noise with a 1/f type spectrum.

The study [5] established that the reason for "soft" current-voltage characteristics is the occurrence of a tunnel current in the strong electric field of local defects.

1. Experiment

Photosensitive elements (PSEs) with a pad size of 1.4×1.4 mm^2 were manufactured on *n*-type monocrystalline silicon (Cz-Si) wafers with a diameter of 100 mm, a resistivity of 4–5 Ω·cm and a (100) orientation without swirl defects.

The manufacturing process cycle of manufacturing included oxidation in H_2O + HCl vapors, photolithography, the pre-depositon (precipitation) of boron from boron nitride (BN) sources, boron and phosphorus diffusion (drive-in) in different modes.

The concentration and distribution of local defects across the wafers with the fabricated PSE were analyzed using selective etching and an optical microscopy, and the distribution of the charge carrier lifetime was also determined. The current-voltage characteristics of the PSEs were

measured on the manufactured samples in the range of reverse voltages from 0.01 V to 90 V, and the noise was measured in the frequency range from 10 to 12.000 Hz.

2. Results

2.1 Current-voltage characteristics

Since the defects of the oxide layers [2] seen in an optical microscope have a different diameters (5–10 μm) and depths, not all of them are electrically active, which makes it difficult to compare the spatial distributions of PSEs with a "soft" IVC and defects on the wafer. Only a qualitative relationship was observed between the spatial distributions of such as PSEs and the defect density.

Therefore, to find the dependence of tunnel currents on the oxide defect density, the distribution of the threshold voltage U_t was determined for PSEs with a different number of observed defects (N) (Fig. 1) through an array of 350 PSEs. The threshold value was taken as the value at which the dark current I_d exceeded 10^{-7} A.

The observed correlation of N and the U_t value confirms the relationship between them.

At the same time, the comparison of the spatial distributions of dark currents at voltages of 0.01, 1, and 5 V shows the existence of areas in which a correlation is observed between tunnel currents and currents at low voltages (Fig. 2). This relationship is confirmed by an increase in the proportion of PSEs with a dark current $I_d < 10^{-11}$ A at 0.01 V among elements with a high threshold value (Fig. 3).

The qualitative correlation between the values of N, U_t and I_d shows the relationship between them and, respectively, between the number of defects N and the value of the dark current I_d.

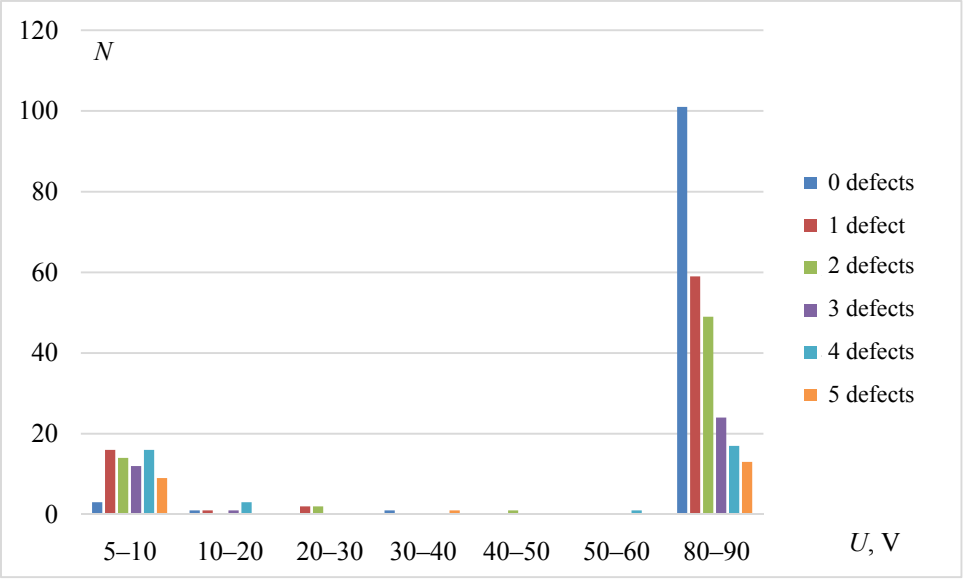

Fig. 1. Histogram of PSE distribution by the threshold voltage value for a different number of defects on one element

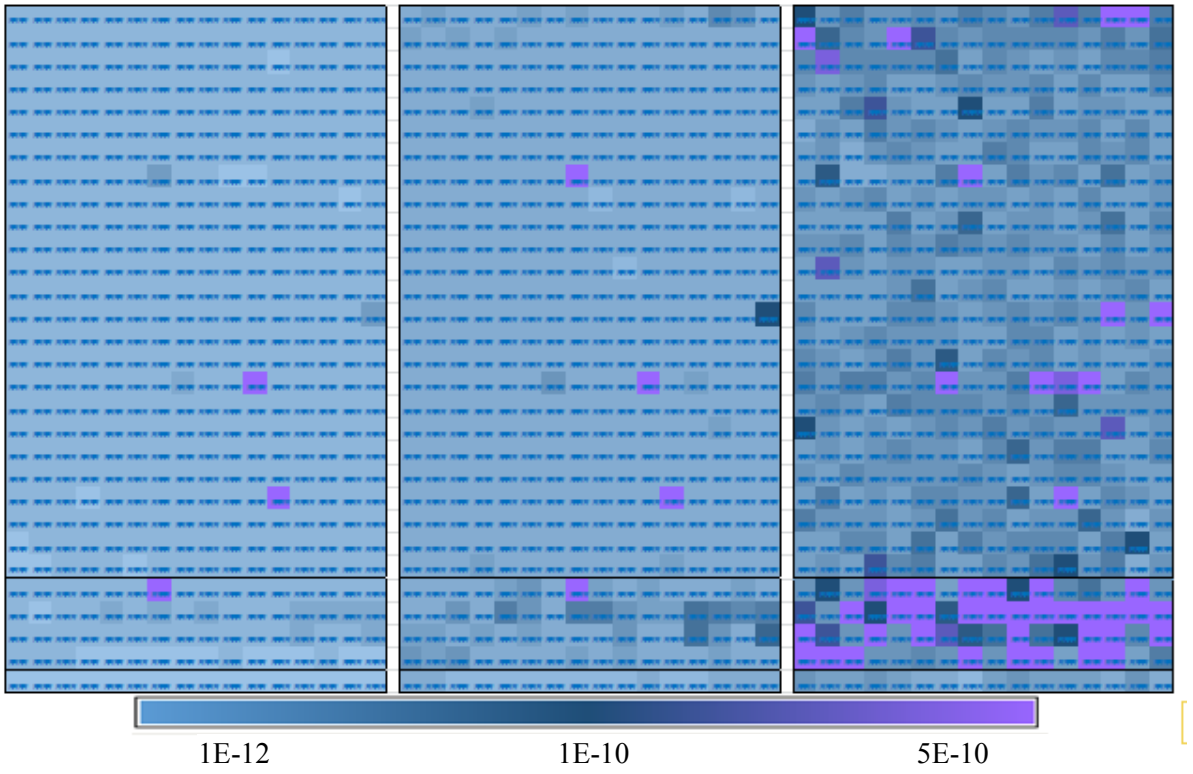

Fig. 2. Distribution of dark currents over the wafer area at voltages of 0.01 V, 1 V, and 5 V.

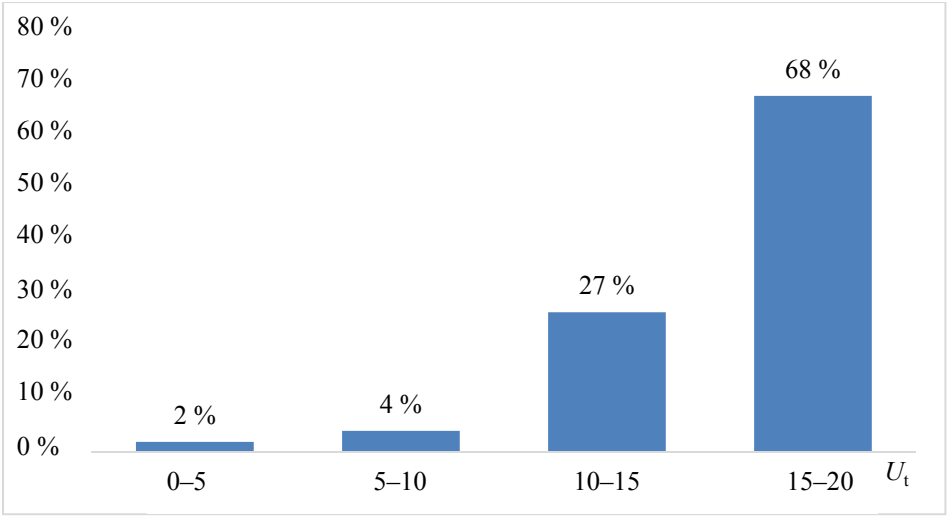

Fig. 3. Dependence of the PSE proportion with a current $I_d < 10^{-11}$ A on the threshold value

2.2. Noise

Measurements of noise and noise spectral density in the frequency band 100–12000 Hz at various reverse voltages were carried out on PSEs with a “soft” IVC. Fig. 4 shows the oscillograms of the noise voltage at bias voltages of 1 V (*a*) and 10 V (*b*). At a voltage of 10 V, which corresponds to the area of exponential growth of the tunnel current, a large number of noise emissions with an amplitude of up to 400 mV were observed against the background of a noise track with an amplitude of up to 50 mV. At the same time, a section of the oscillogram with two states characteristic of “explosive” (random telegraph) noise was observed in some PSEs [5, 6].

Fig. 5 shows the corresponding frequency dependences of the spectral noise density at

voltages of 1 V (a) and 10 V (b), showing a sharp increase in the noise spectral density at a voltage of 10 V, which is especially significant at a frequency of 1 kHz.

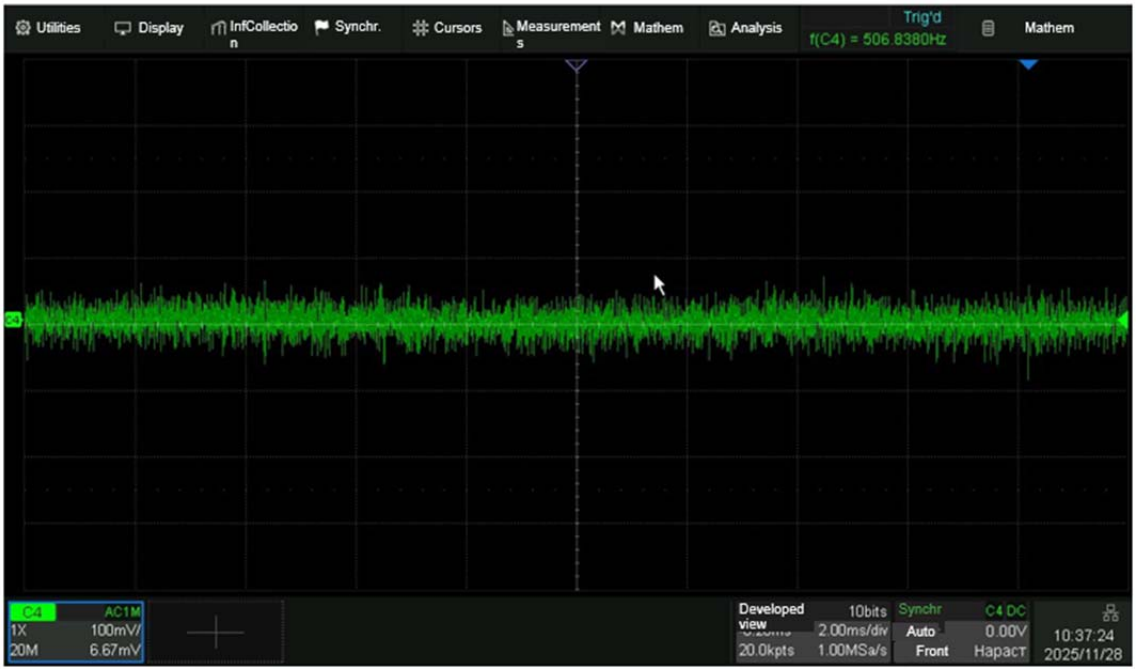

a)

b)

Fig. 4. Noise voltage oscillograms at voltages of 1 V and 10 V

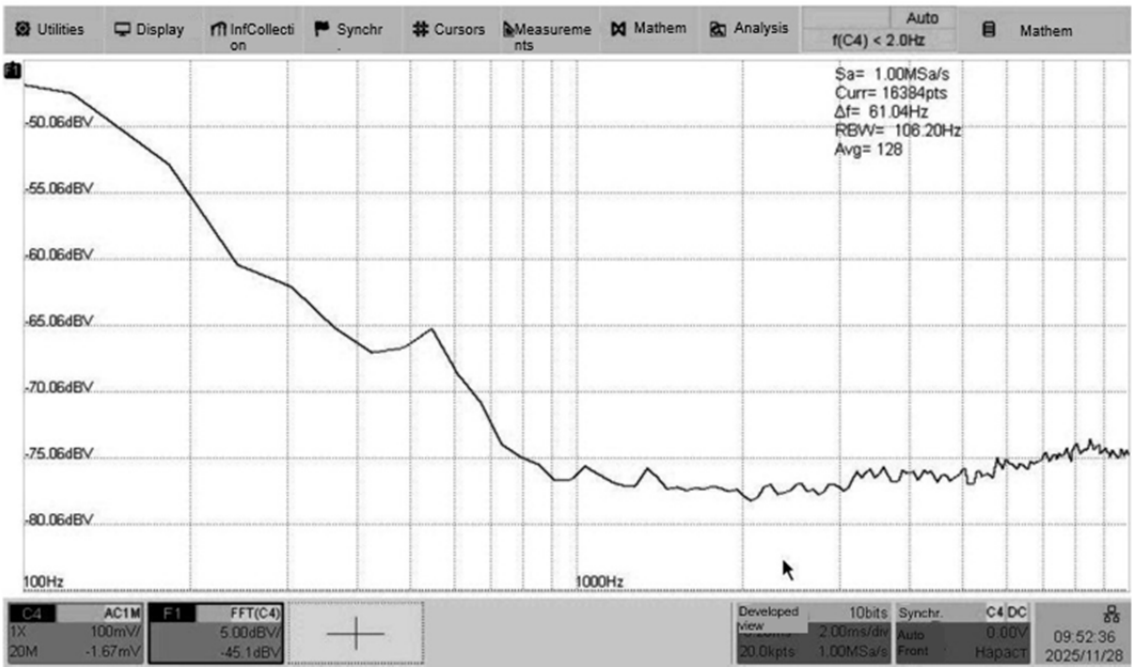

a)

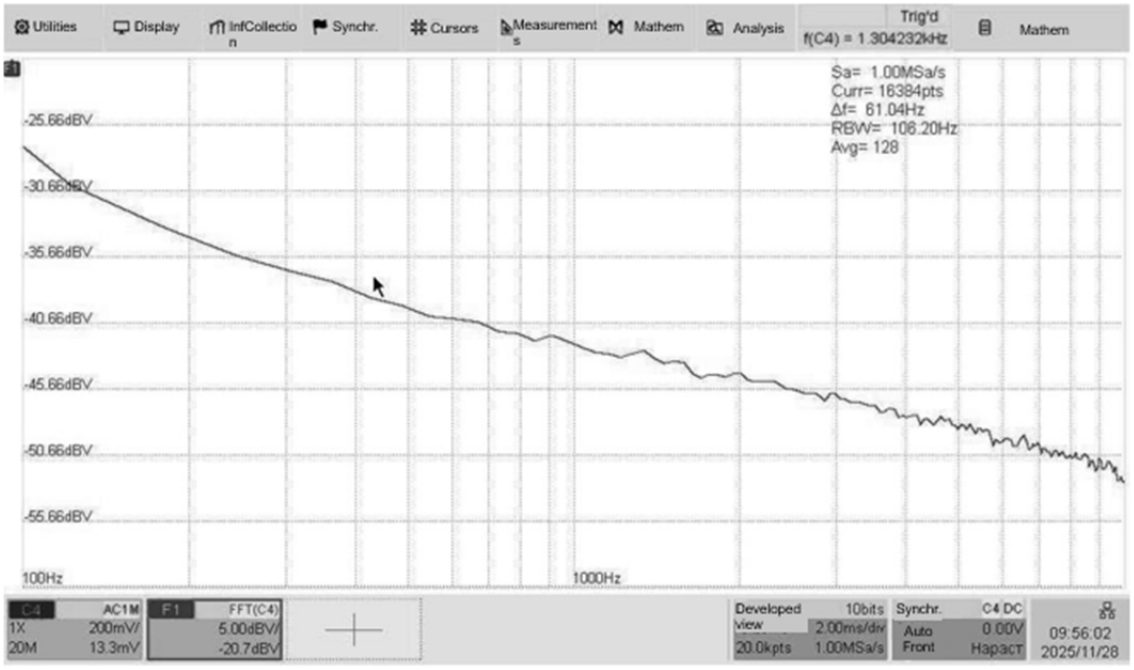

b)

Fig. 5. Dependence of the spectral noise density on frequency at voltages of 1 and 10 V

Discussion of the results

Studies [3, 7] established the influence of oxygen precipitates on the lifetime of charge carriers in silicon, as well as on the dark currents and photosensitivity of photodiodes made on silicon with a circular distribution of oxygen concentration over the wafer area [8].

In this work, silicon without swirl defects was used, with a more uniform distribution of oxygen, which resulted in a more uniform distribution of the charge carrier lifetime (range of 10-12%) and microdefects (etching pits) over the wafer area and, respectively, a random distribution of PSEs with a “soft” IVC.

Since the distribution of PSEs with “soft” characteristics over the area of the wafers is random, the reason for their occurrence may be local defects, such as defects in the oxide and on the silicon surface formed by phosphorus

diffusion [2]. The location of defects causing tunnel currents near the surface is confirmed by the fact that in the considered range of reverse voltages, the width of the space charge region of the p^+–n junction with a high field strength does not exceed 5–7 microns. Deep defects of the specified type may lead to a tunnel breakdown of parasitic p^+–n^+ junctions due to a high concentration of alloying admixtures, as well as the formation of local defects on the silicon surface containing impurities of oxygen, carbon, and heavy metals (impurity precipitates). A tunnel breakdown of p^+–n^+-junctions results in an IVC with a sharp breakdown at voltages of 6–7 V.

Consequently, an important task is to reduce the density of oxide defects, which is achieved by optimizing the phosphorous diffusion modes and improving of the quality of the oxide formed before diffusion [1, 2].

Another reason for the occurrence of tunnel currents can be impurity precipitates, including oxygen ones, in the space charge region of p–n-junctions [9, 10], resulting in a "soft" IVC with increasing currents at voltages exceeding 10 V. By selecting the optimal modes of the gettering operation, leading to the removal of heavy metal impurities from silicon, including from impurity precipitates, it is possible to significantly reduce the number of PSEs with such characteristics.

Repeated impurity gettering on wafers containing PSEs with "soft" characteristics also leads to a reduction in the number of such elements.

The dependence of the spectral noise density on the value of the reverse voltage at 1 V and 10 V at frequencies of 100 Hz and 1 kHz shows a significantly weaker dependence on the current for low-frequency noise, which may indicate different noise generation mechanisms: at low frequencies, the $1/f$ type prevails, caused the trapping of the surface states at the Si-SiO_2 boundary, while at high frequencies "explosive" (RTN) noise, having a wide range, dominates. Since there are known works [11, 12], linking the occurrence of RTN in p–n-junctions with the modulation of the current flowing through impurity precipitates, these data can also confirm the model of tunnel current generation in the precipitate electric field.

The expression for the electric field in the area of the precipitate can be written as follows [9]:

$$E = \beta E_{\max} = \beta\left(\frac{2qNd}{\varepsilon_s}\right)\left(V_b + V\right)^{1/2}, \qquad (1)$$

where V_b is the built-in potential, N_d is the concentration of charge carriers in the n-region, $E_{\max}$ is the maximum field strength in a homogeneous area of the space charge, β is a coefficient considering local field changes due to the defect, and ε_s is the dielectric constant.

Using the experimentally obtained values of the coefficient β = 100–200 for different samples, it is possible to estimate the shape of the defects. Large values of β indicate that the defect is elongated along the applied field. This allows the defect's electric field to be analyzed using the potential solution for a conducting prolate hemispheroid (with semi-axes c and b) oriented along a uniform electric field E_0 [13]. The expression for the electric field on the surface of the hemispheroid in the direction of the major axis is written as follows:

$$E = E_0 \frac{1}{\left(\frac{1}{2}\ln\frac{\eta_0+1}{\eta_0-1}-1\right)\left(\eta_0^2-1\right)}, \qquad (2)$$

where $\eta_0 = c/(c^2-b^2)^{1/2}$, and E_0 is the field of the space charge region of the p–n-junction.

From expression (2) and the given values of β we obtain the ratio of the semiaxes c/b = 10–20. Assuming b to be half the diameter of the defect and using b = 200–300 A [2], we obtain the defect size in the field direction to be 0.2–0.6 μm. A variation of c/b values results in a corresponding variation in the values of threshold voltages of the tunnel current.

Thus, another reason for "soft" VAC and increased PSE noise is elongated impurity precipitates in the space charge region of the junction, for the removal of which it is necessary to use optimal modes of gettering metal impurities.

Conclusions

1. The current-voltage characteristics of silicon photodiodes with leakage currents are determined by the presence of a tunnel component of the current. The value of the dark current at low voltages (0.01 V) depends on the

voltage at the start of the sharp increase in the tunnel current (threshold voltage).

2. There is a correlation between the threshold voltage, the value of the dark current, and the number of oxide defects.

3. The presence of tunnel currents results in different type of noise. In some cases, "burst" (random telegraph) noise is observed at high tunnel currents.

4. The cause of the tunnel currents is local defects with a small area in the oxide, which results in the formation of parasitic p^+–n^+-junctions, and impurity precipitates in the space charge region of the p–n-junction that are elongated in the direction of the electric field.

5. An improvement of dielectric quality and the use of optimal impurity gettering lead to a sharp decrease in the number of photosensitive elements with a tunnel currents.

REFERENCES

1. Blackstone S., Henry W., Jastrzebski L. and Fisher A. W., Journal of Electrochemical Society **3**, 667–668 (1982).
2. Boltar K. O., Vildyaeva M. A., Irodov N. A., Klimanov E. A., Lyalikov A. V., Malygin V. A., Molchanov D. S., Makarova E. A., Applied Physics, No. 2, 39 (2025) [in Russian].
3. Murphy J. D., Al-Amin M., Bothe K., Olmo M., Voronkov V. V., and Falster R. J., Journal of Applied Physics **118**, 215706 (2015).
4. Rejvi K. Defekty` i primesi v poluprovodnikovom kremnii. Moscow: "Mir", 1984, pp. 269.
5. Boltar K. O., Vildyaeva M. A., Demidov S. S., Klimanov E. A., Molchanov D. S., Makarova E. A., Popov K. A., Zhukovich-Gordeeva A. A., and Egorov A. V., Applied Physics, No. 6, 5 (2025) [in Russian].
6. Bukingem M. Shumy` v e`lektronny`x priborax i ustrojstvax. Moscow: "Mir", 1986, pp. 193.
7. Vil'dyaeva M. N., Demidov S. S., Klimanov E. A., Lyalikov A. V., and Fokina A. S., Applied Physics, No. 6, 54 (2017) [in Russian].
8. Vil'dyaeva M. N., Demidov S. S., Klimanov E. A., Lyalikov A. V., and Fokina A. S., Usp. Prikl. Fiz. (Advances in Applied Physics) **5** (3), 282–287 (2017) [in Russian].
9. Busta H. H. and Waggener H. A., Journal of Electrochemical Society **124** (9), 1424–1429 (1977).
10. Vil'dyaeva M. N., Demidov S. S., Demidova Yu. S., Klimanov E. A., Skrebneva P. S., and Khlyzova U. D., Usp. Prikl. Fiz. (Advances in Applied Physics) **13** (6), 511–514 (2023) [in Russian].
11. Hsu S. T., Whittier R. J., and Mead C. A., Solid-State Electronics **13**, 1055–1070 (1970).
12. Mori Y., Takeda K., and Yamada R., Journal of Applied Physics **107**, 014509 (2010).
13. Smythe W. R. Static and Dynamic Electricity. McGraw-Hill, 1969, pp.178–179.

About authors

Boltar Konstantin Olegovich, Doctor of Physical and Mathematical Sciences and Mathematics, Head of Scientific and Technical Complex, RD&P Center ORION, JSC (111538, Russia, Moscow, Kosinskaya st., 9); Moscow Institute of Physics and Technology (141701, Russia, Dolgoprudny, Moscow Region, 9, Institutsky lane). E-mail: boltarko@yandex.ru SPIN code: 9249-2720, AuthorID: 171355

Vildyaeva Maria Nikolaevna, Engineer Cat. 1, RD&P Center ORION, JSC (111538, Russia, Moscow, Kosinskaya st., 9). E-mail: mari.vildyaeva@mail.ru

Demidov Stanislav Stefanovich, RD&P Center ORION, JSC (111538, Russia, Moscow Kosinskaya st., 9). SPIN code: 2028-9758, AuthorID: 780596

Klimanov Evgeniy Alekseevich, Doctor of Technical Sciences, Professor, Chief Research Assistan, RD&P Center ORION, JSC (111538, Russia, Moscow, Gilyarovskogo st., 9); MIREA – Russian Technological University (119454, Russia, Moscow, Vernadskogo avenue, 78). E-mail: klimanov3@mail.ru SPIN code: 7697-4688, AuthorID: 171375

Konorev Dmitry Sergeevich, Engineer, RD&P Center ORION, JSC (111538, Russia, Moscow. Kosinskaya st., 9). E-mail: konorev.dima@mail.ru

Makarova Elina Alekseevna, Engineer Cat. 2, RD&P Center ORION, JSC (111538, Russia, Moscow, Kosinskaya st., 9).

Molchanov Dmitry Sergeevich, Engineer, RD&P Center ORION, JSC (111538, Russia, Moscow. Kosinskaya st., 9).

Popov Konstantin Alekseevich, engineer, RD&P Center ORION, JSC (111538, Russia, Moscow, Kosinskaya st., 9). E-mail: kostya.popov.2001@gmail.com SPIN code: 5321-4009

Poluneev Vladimir Vasilievich, Chief Specialist RD&P Center ORION, JSC (111538, Russia, Moscow, Kosinskaya st.,9). SPIN code: 5228-6837, AuthorID: 780556

Zhukovich-Gordeeva Aleksandra Aleksandrovna, Engineer Cat. 2 RD&P Center ORION, JSC (111538, Russia, Moscow, Kosinskaya st., 9).

PLASMA PHYSICS AND PLASMA METHODS

UDC 533.9.03, 537.528 PACS: 52.77.-j
EDN: UEWQIB

Conversion of CO_2 in microwave discharge in liquid methanol

T. S. Batukaev[1], I. V. Bilera[1], G. V. Krashevskaya[1,2], Yu. A. Lebedev[1*], and V. K. Shumilov[1]

[1] *A. V. Topchiev Institute of Petrochemical Synthesis of the Russian Academy of Sciences (TIPS RAS), Moscow, 119991 Russia*
[*] *E-mail: lebedev@ips.ac.ru*
[2] *Institute LAPLAZ, National Research Nuclear University MEPhI, Moscow, 115409 Russia*

Received 20.01.2026; revised 9.02.2026; accepted 27.04.2026

The dependence of the degree of CO_2 decomposition and the concentration of the main products (H_2 and CO) on the CO_2 flow rate at the reactor inlet is shown. The maximum degree of CO_2 decomposition reached 75 %.

Keywords: microwave discharge in liquid methanol, CO_2 decomposition, chromatography of discharge products, production of synthesis gas.

DOI: 10.51368/2949-561X-2026-2-35-38

For citation: Batukaev T. S., Bilera I. V., Krashevskaya G. V., Lebedev Yu. A., and Shumilov V. K., Applied Physics, No. 2, 35–38 (2026).

Introduction

Currently, technologies for the decomposition and conversion of carbon dioxide (CO_2) into valuable chemical products are being studied. This task is important for ensuring the ecological safety of industrial processes, where carbon dioxide is one of the by-products. An effective way to solve this problem is to use a low-temperature plasma generated by various types of electrical discharges [1].

The study of the CO_2 conversion process is carried out mainly in a gas-discharge plasma. It is known that the addition of components such as methane and hydrogen allows one to significantly increase the degree of CO_2 decomposition. Thus, the positive effect of hydrogen and methane on CO_2 conversion is confirmed in dielectric barrier discharges, sliding arcs, and microwave discharges in the gas phase (see, for example, [2–8]). The introduction of methanol vapor in a mixture with CO_2 contributes not only to an increase in the decomposition degree but also to the formation of synthesis gas [8, 9]. The obtained CO_2 conversion degrees do not exceed 20 %.

Study [9] demonstrated a new approach to the plasma conversion of a mixture of CO_2 and methanol vapor in a device with a sliding arc at atmospheric pressure, which makes it possible to obtain synthesis gas with simultaneous CO_2 conversion with an efficiency of up to 20 %. By analogy with traditional dry methane reforming, this process is called “dry methanol reforming” by the authors.

A high degree of CO_2 conversion is demonstrated by microwave discharges initiated in the liquid phase, where the discharge is ignited in a gas bubble at the end of a microwave antenna. One of the most important advantages of such systems is the natural implementation of the products’ quenching process at the stage of the discharge afterglow (after the separation of the gas bubble from the antenna, caused by liquid evaporation into a hot gas bubble). This significantly increases the efficiency of CO_2 decomposition. In particular, in study [10] at atmospheric pressure, using a microwave discharge in liquid hydrocarbons, a 60 % decomposition degree of CO_2 was achieved. The degree of CO_2 conversion reached 45 % [11] in a microwave discharge in an aqueous solution. It is

worth noting that under these conditions, the product is synthesis gas, which serves as a raw material for obtaining different chemical compounds. The disadvantage of using such liquids was the formation of soot. In [11], to suppress soot formation, instead of pure ethanol, its aqueous solution was used, which negatively affected the CO_2 conversion.

Therefore, it is promising to study CO_2 conversion in a microwave discharge in liquid methanol, which is the simplest representative of the homologous series of alcohols, and in plasma of which H_2 and CH_4 are formed without soot generation. [12].

This study presents for the first time the results of an experimental study of CO_2 conversion when passing it through a microwave discharge in methanol. Special emphasis is placed on determining the decomposition degree of CO_2 and the composition of the main gaseous products.

Experimental Setup

Experimental setup used for the generation and study of a microwave discharge in liquids is described in detail in [10, 11]. The microwave system includes a magnetron microwave oscillator (2.45 GHz) and the elements necessary for the controlling and measuring the incident microwave power. The experiments were carried out at an incident microwave power of 490 W. The discharge section is a coaxial-to-waveguide adapter, the central conductor of which serves as an antenna for microwave energy input into the reactor. The discharge was formed near the antenna tip in a quartz reactor (diameter 55 mm) filled with methanol and placed in a protective metal mesh (wire spacing 0.5 mm). To facilitate the discharge, a tungsten rod with a diameter of 3 mm was located over the central conductor at a distance of 3 mm. The central conductor of the coaxial line was a tungsten tube (outer diameter 3.0 mm, channel diameter 1 mm), through which carbon dioxide was supplied to the liquid. The methanol volume in the reactor was about 40 mL, which ensured that the end of the central electrode of the coaxial line was below the liquid surface.

CO_2 with a flow rate from 110 to 670 mL/min passed through the RRG-20 mass flow controller and was introduced into the reactor through the channel in the antenna. The pressure on the liquid surface was close to atmospheric pressure. The duration of the experiment was about one minute. During this time, the gas flow at the reactor outlet was measured, and after stationary conditions were established, a gas sample was taken for the analyzing the products' composition. During a single experiment, the composition of the liquid in the reactor was replenished.

A water cooler was used to separate the gaseous products of the plasma-chemical reactions from the evaporated liquid products. The condensed liquid was returned to the reactor. The flow rate of the gas mixture flow at the discharge outlet downstream of the water cooler was measured with a mechanical flowmeter.

The composition of the gas phase (CO, CO_2, H_2, C_2H_2, C_2H_4 and CH_4) at the reactor outlet with a discharge was determined on a FIA back-flush portable gas chromatograph (SPC MEMS, Russia) with a thermal conductivity detector (TCD) and two chromatographic columns using HayeSep N adsorbents and 13X molecular sieves. The carrier gas was argon.

The main discharge products were H_2 and CO. Minor mixture components included CO_2, CH_4, C_2H_2 and C_2H_4. In this paper, we focus on studying the process of CO_2 decomposition and the production of synthesis gas.

The decomposition degree of CO_2 (α) was calculated from the product flow rates at the reactor output using the formula:

$$\alpha = \frac{CO_2^{input} - CO_2^{out}}{CO_2^{input}} \cdot 100\ \% \qquad (1)$$

where CO_2^{out} is the CO_2 flow rate of at the reactor output and CO_2^{input} is the CO_2 flow rate at the reactor input. These values were obtained from the measured total gas flow rate at the reactor output and the corresponding component concentrations.

Results and Discussion

Fig. 1 shows the dependences of the concentration of the main components of the gas mixture at the discharge outlet on the CO_2 flow

rate at the reactor input. The decrease in the hydrogen concentration with an increase in the CO_2 flow rate is probably related to the dilution of the methanol vapor with carbon dioxide, as well as the reduction of the residence time of the reaction mixture in the discharge zone. It should be noted that the residence time decreases due to the reduction of the lifetime of the gas bubble containing the plasma with the increase in the CO_2 flow rate.

Fig. 2 shows the dependence of CO_2 decomposition degree on its flow rate at the reactor input. A decrease in the CO_2 decomposition degree is due to the reduction of the residence time of the reaction mixture in the discharge zone.

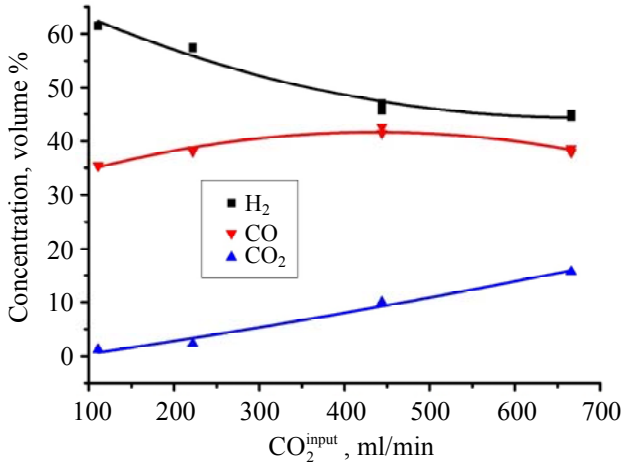

Fig. 1. Dependence of the concentrations of the main products on the CO_2 flow rate

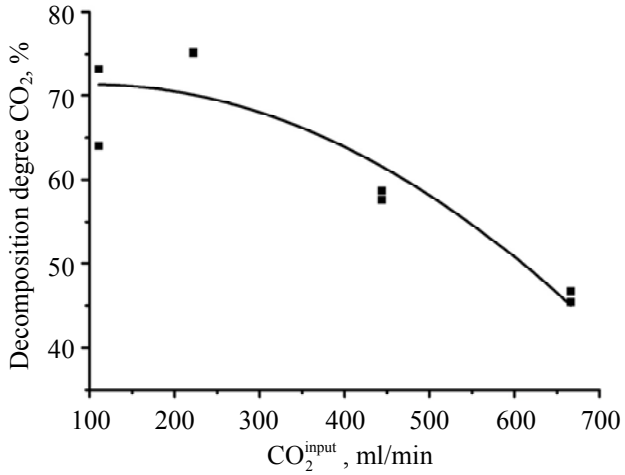

Fig. 2. Dependence of the CO_2 decomposition degree on the CO_2 flow rate at the input

Conclusion

The presented results show that a microwave discharge in liquid methanol can be an effective method for decomposing carbon dioxide while simultaneously producing synthesis gas. The obtained degree of carbon dioxide conversion exceeds the values obtained in a microwave discharge in an ethanol aqueous solution.

The paper has been prepared as part of the state assignment of the Institute of Petrochemical Synthesis RAS

REFERENCES

1. Bogaerts A. and Centi G., Front. Energy Res. **8**, 111 (2020).
2. Aerts R., Snoeckx R., and Bogaerts A., Plasma Process. Polym. **11** (10), 985 (2014).

3. Kim S. C., Lim M. S., and Chun Y. N., Plasma Chem. Plasma Process **34**, 125 (2014).
4. Van Alphen S., Wanten B., Girard-Sahun F., Slaets J., Creel J., Aghaei M., and Bogaerts A., Sustain. Chem. Eng. **12** (42), 15715 (2024).
5. Mei D., Duan G., Fu J., Liu S., Zhou R., Zhou R., and Ostrikov K. K., J. CO2 Util. **53**, 101703 (2021).
6. Wanten B., Gorbanev Y., and Bogaerts A., Fuel **374**, 132355 (2024).
7. Kelly S., Mercer E., De Meyer R., Ciocarlan R. G., Bals S., and Bogaerts A., J. CO2 Util. **75**, 102564 (2023).
8. Czylkowski D., Hrycak B., Miotk R., Jasinski M., Dors M., and Mizeraczyk J., Int. J. Hydrogen Energy **40** (40), 14039 (2015).
9. Zhang H., Li X., Zhu F., Cen K., Du C., and Tu X., Chem. Eng. J. **310**, 114 (2017).
10. Batukaev T. S., Bilera I. V., Krashevskaya G. V., Lebedev Y. A., and Nazarov N. A., Plasma **6** (1), 115 (2023).
11. Batukaev T. S., Bilera I. V., Krashevskaya G. V., Lebedev Y. A., and Shumilov V. K., Pisma v Zhurnal Tekhnicheskoi Fiziki **51** (21), 50–53 (2025).
12. Niu Y. L., Li S. Z., Wang X. C., Cao S. L., Yang D., and Zhang J., J. Appl. Phys. **134** (1), 013304 (2023).

About authors

Batukaev Timur Saidemievich, Candidate of Physical and Mathematical Sciences, Research fellow A. V. Topchiev Institute of Petrochemical Synthesis of the Russian Academy of Sciences (TIPS RAS) (119991, Russia, Moscow, Leninsky Prospekt, 29). E-mail: batukaevtimur95@gmail.com ORCID: 0001-8246-0868, WOS Research ID AAQ-7536-2021, SPIN code: 4215-8220, Scopus Author ID 57209216257

Bilera Igor Vasilievich, candidate of chemical sciences, Leading Researcher A. V. Topchiev Institute of Petrochemical Synthesis of the Russian Academy of Sciences (TIPS RAS) (119991, Russia, Moscow, Leninsky Prospekt, 29). E-mail: bilera@ips.ac.ru ORCID 0000-0001-6724-1907, WOS Research ID E-6524-2014, SPIN code: 5140-8527, Scopus Author ID 6603277297

Krashevskaya Galina Vitalevna, Candidate of Physical and Mathematical Sciences, Associate Professor A. V. Topchiev Institute of Petrochemical Synthesis of the Russian Academy of Sciences (TIPS RAS) (119991, Russia, Moscow, Leninsky Prospekt, 29); Institute LAPLAZ, National Research Nuclear University MEPhI (115409, Russia, Moscow, Kashirskoe Shosse, 31). E-mail: krashevskaya-gv@mail.ru ORCID: 0001-6724-1907, WOS Research ID N-5208-2017, SPIN code: 1186-9514, Scopus Author ID 35776305000

Lebedev Yurii Anatolevich, Doctor of Physical and Mathematical Sciences and Mathematics, Chief researcher, A. V. Topchiev Institute of Petrochemical Synthesis of the Russian Academy of Sciences (TIPS RAS) (119991, Russia, Moscow, Leninsky Prospekt, 29). E-mail: lebedev@ips.ac.ru ORCID: 0001-5374-3957, WOS Research ID E-5939-2014, SPIN code: 2509-0361, Scopus Author ID 57203810439

Shumilov Vladislav Konstantinovich, student, A. V. Topchiev Institute of Petrochemical Synthesis of the Russian Academy of Sciences (TIPS RAS) (119991, Russia, Moscow, Leninsky Prospekt, 29). E-mail: shumilow.vladislav@yandex.ru SPIN code: 8718-2948, AuthorID: 1318446

PLASMA PHYSICS AND PLASMA METHODS

UDC 537.868.4 PACS: 75.78.-n, 77.84.-s
EDN: UJSYVZ

The effect of plasma on resonant scattering of a magnetic field by a dielectric ring

M. S. Dobroklonskaya*, V. Ya. Pecherkin, and L. M. Vasilyak

Joint Institute for High Temperatures of Russian Academy of Sciences, Moscow, 125412 Russia
** E-mail: m.dobro42@gmail.com*

Received 2.03.2026; revised 23.03.2026; accepted 27.04.2026

The resonance scattering spectra on the main magnetic mode of structures made of a subwavelength dielectric thin ring and a low-pressure discharge plasma in a linear fluorescent lamp and a spiral lamp excited by an incident plane electromagnetic wave of the microwave range have been experimentally studied. It was found that when the discharge is turned on, the amplitude of the magnetic field induced by the ring at the resonant frequency of the ring decreases significantly. The reduction effect is realized with a certain orientation of the discharge relative to the ring. Computer simulation confirms the effect of reducing the magnetic field induced by the ring at the resonant frequency. An electric discharge can be used to switch the resonant electromagnetic fields of dielectric elements in filters, antennas, and energy redistribution systems.

Keywords: low pressure discharge, dielectric magnetic dipole, negative magnetic response, dielectric ring, plane microwave, resonance.

DOI: 10.51368/2949-561X-2026-2-39-43

Introduction

Resonant elements of different types [9–11] are used to create metamaterials [1], metasurfaces [2] for antennas [3–5], radiation filtration and redistribution systems [6, 7] and ideal lenses [8]. The first metamaterials were created on the basis of a resonant *LC* circuit in the form of a metal ring with a thin slit [12, 13], the properties of which are well-known, and the resonant parameters can be calculated based on capacitance, self-inductance, and magnetic fields from the Biot-Savart-Laplace law. Based on these elements, a large number of designs have been created for the microwave field, specifically in filter and antenna engineering. Replacement of metal meta-elements with dielectric ones is one of the ways to reduce dissipation losses at high frequencies. However, even in simple dielectric bodies, for example, a sphere, disk, or cylinder, when interacting with an electromagnetic wave, different types of resonances are excited, the frequencies of which can coincide; therefore, the calculations of resonance frequencies and scattering fields for dielectric bodies are becoming a complicated problem [14–19]. Prior studies have shown that a sub-wavelength dielectric ring is an ideal magnetic-type dipole [20] with a fundamental resonance frequency that can be calculated from the concepts of capacitance and self-inductance, and scattering fields from the Biot-Savart-Laplace law. Therefore, the dielectric ring can be used in structures that have already been created based on a metal ring dipole.

The aim of this work was to study the resonance magnetic field of a system made of a dielectric ring and a plasma element in the form of a positive column of a low-pressure discharge under the excitation of a flat EM-wave in the microwave range.

Results of experiments and computer simulation

The scheme for conducting experiments on measuring the magnetic fields of the structure of a dielectric ring and an additional conductive element excited by a flat electromagnetic wave was similar to the one used before [21]. The driving generator was one of the channels of an Agilent E5071C ENA network analyzer, the signal from which was transmitted to an amplifier (20 dB) and then to an ETS-Lindgren's model 3115 horn antenna that formed a flat linearly polarized wave. Magnetic fields were measured with a Beehive Electronics 100B EMC probe with an internal diameter of the detector ring of 3.7 mm, the signal from which was sent to the input of the Agilent E5071C ENA network analyzer. A flat microwave excited the system of the dielectric ring ($\varepsilon = 149$, $\mathrm{tg}\alpha = 0.0003$, external diameter of 38 mm, internal of 28 mm, height of 5 mm) and the plasma element. Straight and spiral fluorescent lamps were used as the plasma element.

Fig. 1 shows the system of the dielectric ring located on top of the spiral lamp with a power of 13 W, and external diameter of the rings of 38 mm, and a plasma diameter of 7 mm. The ring with the lamp was located at a distance of 25 cm from the antenna in such a way that the wave vector and electric field vector of the flat incident wave were parallel to the plane of the dielectric ring and the rings of the gas-discharge tube, while the wave magnetic field vector was perpendicular. The dielectric ring was placed either directly on the lamp or above the top lamp ring at a distance of 5 mm. Since the lamp spiral is structurally folded at the end, the dielectric ring is closely adjacent only to a half-ring of the lamp spiral. The magnetic field probe was located on the side of the dielectric ring farthest from the antenna. The distance from the ring edge to the probe was 10 mm, therefore, the probe measured the resonance spectrum of the transmitted signal in the near zone of the ring. The plane of the magnetic probe ring was perpendicular to the vector of the magnetic field and parallel to the wave vector and vector of the electric field of the incident wave.

Fig. 1. Photo of the dielectric ring system on the spiral lamp. The magnetic field probe is located on the right

Experimental results of the measurement of the magnetic field spectra of the ring and the spiral lamp are shown in Fig. 2. When the lamp is off, a standard resonant peak of the magnetic dipole is observed (curve *1*). When plasma is created in the lamp (the lamp is on), the resonant peak disappears (curve *2*). Curve *3* is the background signal from the probe when there is no ring and the lamp is off. The turned-on lamp with plasma (without the ring) slightly shields the transmitted signal (curve *4*). With other arrangements of the dielectric ring near the spiral lamp, no such strong attenuation effect at the resonance frequency is observed. Consequently, the effect of the interaction of the fields of the dielectric ring with the plasma half-ring occurs only when the induced electric field in the dielectric ring interacts closely with the plasma in the lamp, as a result of which an induced current with energy dissipation passes through the plasma. If the interaction length is small, the attenuation is also small. If the ring is removed from the lamp by 5 mm, the effect weakens dramatically. Thus, the plasma element in the form of a low-pressure electric discharge can act as a switch with the help of which one can turn on and turn off the resonant element.

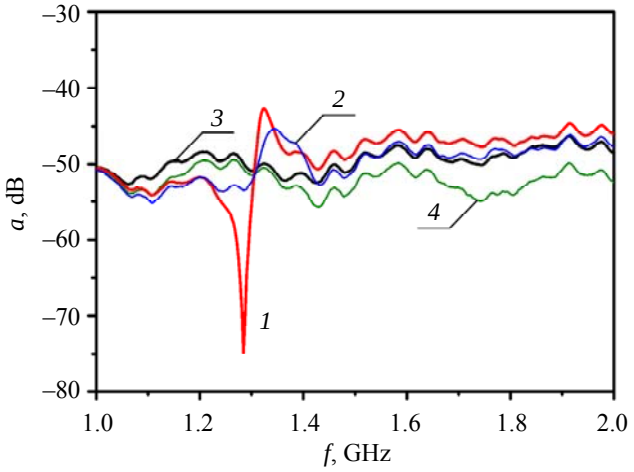

Fig. 2. Measured magnetic field spectra. 1 – ring on a lamp without plasma (red line 1); 2 – ring on a lamp with plasma (blue line 2); 3 – without the ring, lamp without plasma (black line 3); 4 – without the ring, lamp with plasma (green lime 4)

Based on the lamp power and current, the average electron concentration is about 10^{13} cm^{-3} at a standard electric field strength in the column of about 1 V/cm; therefore, the plasma frequency is orders of magnitude higher than the range of resonance frequencies of the dielectric ring. Consequently, the experiments and computer simulation can be conducted using a copper wire in the form of a half-ring instead of plasma placed on top of the dielectric ring. To isolate the scattered component of the magnetic field of the studied system, a measurement of the level of background radiation, initiated by the wave with the probe in the absence of the test objects, is conducted. Then the background signal was subtracted from the signal measured in the presence of the test elements. The computer simulation was conducted using the CST Microwave Studio software. The calculation parameters were set in accordance with the experimental conditions for the copper wire (conductivity 58 mln Sm/m) with a diameter of 2 mm in insulation with a thickness of 0.7 mm. The half-ring was located in different positions on the dielectric ring. The results of the experiments and calculations with the copper half-ring located with the bulge towards the probe are shown in Fig. 3. It can be seen that the calculated and experimental resonance spectra of a single dielectric ring match well in frequency (curves *1* and *2*). When adding a copper half-ring, the resonance frequency shifts towards low frequencies and decreases in amplitude both in the experiments and calculations (curves *3* and *4*). A decrease in the resonance frequency is associated with an increase in the effective capacitance in the resonant circuit when adding the metal half-ring. In the case of plasma, energy dissipation also occurs; therefore, the amplitude of the scattered magnetic field is strongly attenuated.

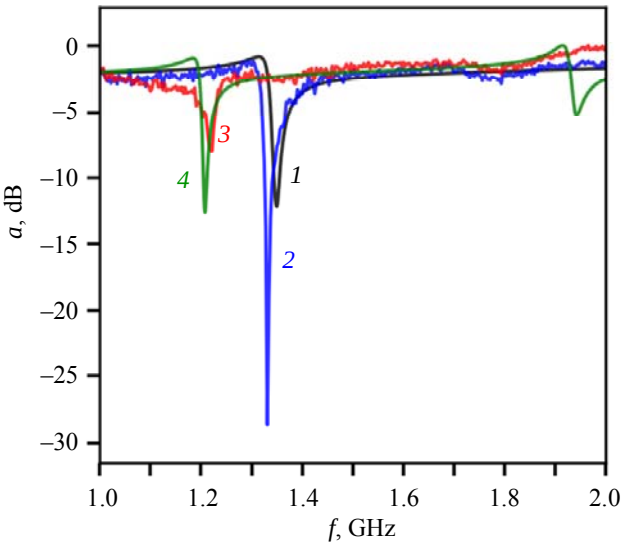

Fig. 3. Resonance magnetic field spectra for the dielectric ring and the half ring made of copper wire with a diameter of 2 mm in the insulation of 0.7 mm with a bulge towards the probe. The distance from the ring to the probe is 30 mm: 1 (black) – calculation, single dielectric ring, f_0 = 1.350 GHz, a_0 = –11.832 dB; 2 (blue) – experiment, single dielectric ring f_0 = 1.331 GHz, a_0 = –28.675 dB; 3 (red) – experiment, metal half-ring f_0 = 1.222 GHz, a = –7.903 dB; 4 (green) – calculation, copper half-ring f_0 = 1.208 GHz

Systems with the dielectric ring and linear low-voltage lamps with powers of 12 W and 15 W, diameters of 12.5 mm and 26 mm, and lengths of 370 mm and 430 mm, respectively, as well as copper wires of different lengths, have been studied during the lamp replacement. The

lamp or copper wire was located right after the dielectric ring, perpendicular to the wave vector and parallel to the electric field vector of the incident microwave. The probe was located after the lamp or the conductor at a distance of 30 mm from the ring. An example or the experimental results and calculations for the system of the ring and the copper wire with a half-wave length at the resonance frequency (115 mm) is shown in Fig. 4. The calculated and experimental spectra match well in the resonance frequency (curves *1* and *2*). When adding a wire behind the ring, the amplitude of the magnetic field is attenuated at the resonant frequency both in the experiment (curve *3*) and in the calculations (curve *4*).

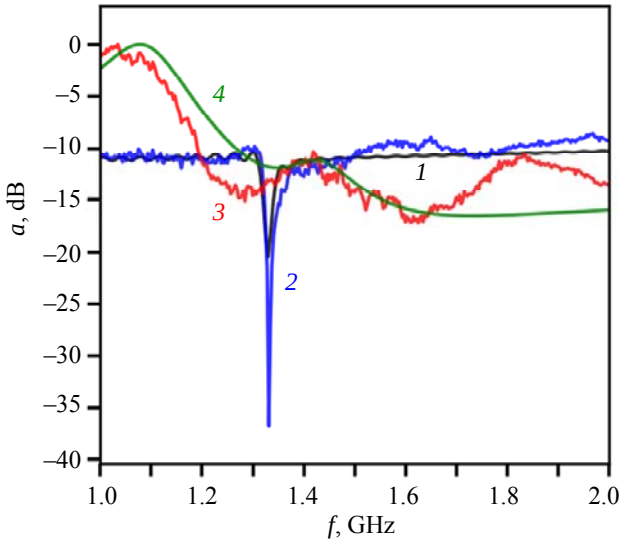

Fig. 4. Resonance spectra of the magnetic field for the ring and the half-wave straight conductor (115 mm): 1 (black) – calculation, single dielectric ring, f_0 = 1.350 GHz, a_0 = –11.832 dB; 2 (blue) – experiment, single dielectric ring f_0 = 1.331 GHz, a_0 = –28.675 dB; 3 (red) – experiment, ring with conductor; 4 (green) – calculation, ring with conductor

It is worth noting that the attenuation of the resonant amplitude of the magnetic field occurs only with a certain lamp orientation relative to the dielectric ring. If the ring is placed on the lamp, i.e. the axes of the lamp and the ring coincide, the lamp does not affect the spectrum. There is no effect if the lamp axis is parallel to the magnetic field or in other lamp positions near the ring. The lamp and the conductor have the greatest influence in the position when they are parallel to the electric field vector. If the conductor or lamp is parallel to the wave vector, then they affect the resonant spectrum of the ring only in the case when part of the lamp or the wire is on the left or right side of the ring, i.e. they can interact with the electric field of half the ring. If a lamp or wire passes through the center of the ring, there is no impact. Therefore, a straight lamp or a straight conductor can interact either through the circular electric fields of the ring, as in the case of a spiral lamp, or create an additional resonant system and shield the passing wave induced by the resonant field of the dielectric ring. In the second case, high-conductivity turns out to be a more important factor than attenuation in the plasma, which is confirmed by the calculations. Therefore, a plasma element in the form of a straight lamp can also turn on or off a passing resonant wave or resonant magnetic field. Such switches can be used in filters, antennas, and distribution systems of microwave energy.

Conclusion

The resonant scattering spectra of the dielectric ring – plasma element system have been studied. It was found that when the discharge is switched on, the attenuation of the amplitude of the scattered resonant magnetic field of the ring increases sharply. Experimental and computer modeling involving the replacement of plasma with a copper wire showed that in the case of half-ring, the resonance frequency shifts and the amplitude attenuates. In the case of a straight wire and a straight lamp, there is a resonant interaction of the incident plane EM-wave not only with the dielectric ring but also with the straight wire, as a result of which the strongest interaction occurs in cases when the wire length is a multiple of a quarter of the wavelength at the resonant frequency. It was found that the resonance shift and the attenuation of the resonant scattering occur only at a certain orientation of the plasma column relative to the dielectric ring, when the vector of the induced electric field strength is parallel to the discharge axis. Therefore, the plasma element can be used as a switch with the help of which one can turn on and off resonant scattering fields from the dielectric ring. Such switches can be used for switching resonant filters and for the redistribution of the microwave radiation fluxes in antenna technologies.

REFERENCES

1. Zheng Y., Dai H., Wu J., Zhou C., Wang Z., Zhou R., and Li W., Frontiers in Physics **10**, 1069722 (2022).
2. Remnev M. A. and Klimov V. V., Phys. Usp. **61**, 157–190 (2018).
3. Glybovski S. B., Tretyakov S. A., Belov P. A., Kivshar Y. S., and Simovski C. R., Physics reports **634**, 1–72 (2016).
4. Engheta N., IEEE Transections on Antennas and Wireless Propagation Letters **1** (1), 10–13 (2002).
5. Paniagua-Dominguez R., Luk'yanchuk B., and Kuznetsov A. I., Control of scattering by isolated dielectric nanoantennas. In Dielectric Metamaterials. Woodhead Publishing, 2020, pp. 73–108.
6. Lagarkov A. and Kissel V., Pys. Rev. Lett. **92** (7), 077401 (2004).
7. Klimov V. V., Phys. Usp. **64**, 990–1020 (2021).
8. Lagarkov A. N., Sarychev A. K., Kissel V. N., and Tartakovsky G., Phys. Usp. **52**, 959–967 (2009).
9. Rybin M. V. and Limonov M. F., Phys. Usp. **62**, 823–838 (2019).
10. Klimov V. V., Phys. Usp. **66**, 263–287 (2023).
11. Klimov V. V., Phys. Usp. **62**, 1058–1059 (2019).
12. Pendry J. B., Phys. Rev. Lett. **85** (18), 3996 (2000).
13. Smith D. R., Padilla W. J., Vier D. C., Nemat-Nasser S. C., and Schults S., Phys. Rev. Lett. **84**, 4184–4187 (2000).
14. Kapitanova P., Ternovski V., Miroshnichenko A., et al., Sci Rep. **7**, 731 (2017).
15. Shvartsburg A. B., Pecherkin V. Ya., Jimrenez S., Vasilyak L. M., Vrazquez L., and Vetchinin S. P., J. Phys. D: Appl. Phys. **54**, 075004 (2021).
16. Luk`yanchuk B., Vasilyak L. M., Pecherkin V. Ya., Vetchinin S. P., Fortov V. E., Wang Z. B., Paniagua-Domínguez R., and Fedyanin A. A., Sci Rep-UK **11**, 23453 (2021).
17. Bukharin M. M., Pecherkin V. Y., Ospanova A. K., Il'in V. B., Vasilyak L. M., Basharin A. A., and Luk'yanchuk B., Sci Rep-UK **12** (05), 7997 (2022).
18. Kapitanova P., Zanganeh E., Pavlov N., Song M., Belov P., Evlyukhin A., and Miroshnichenko A., Annalen der Physik **532** (12), 2000293 (2020).
19. Enriquez J. A., Balafendiev R., Millar A. J., Simovski C., and Belov P., Physical Review Applied **23** (5), 054053 (2025).
20. Bukharin M. M., Vasilyak L. M., Basharin A., Luk`yanchuk B., Ospanova A., and Pecherkin V. Ya., Journal of Applied Physics **137**, 203101 (2025).
21. Pecherkin V. Ya., Vasilyak L. M., Bukharin M. M., and Dobroklonskaya M. S., Applied Physics, No. 5, 15–21 (2023) [in Russian].

About authors

Dobroklonskaya Marina Sergeevna, Postgraduate Student, Joint Institute for High Temperatures of Russian Academy of Sciences (125412, Russia, Moscow, 13, Izhorskaya st., bldg. 2). E-mail: m.dobro42@gmail.com SPIN code: 5232-9283, AuthorID: 1175259

Pecherkin Vladimir Yakovlevich, Candidate of Physical and Mathematical Sciences, Senior research scientist , Joint Institute for High Temperatures of Russian Academy of Sciences (125412, Russia, Moscow, 13, Izhorskaya st., bldg. 2). E-mail: vpecherkin@yandex.ru SPIN code: 4910-0417, Author ID: 1089774, ORCID 0000-0001-7470-5132, Scopus ID: 6507468054

Vasilyak Leonid Mikhailovich, Doctor of Physical and Mathematical Sciences, Senior Research Assistant, Joint Institute for High Temperatures of Russian Academy of Sciences (125412, Russia, Moscow, 13, Izhorskaya st., bldg. 2). E-mail: vasilyak@ihed.ras.ru SPIN-code: 5623-5167, AuthorID: 19599, ORCID 0000-0001-6982-3038, Scopus ID 7004886755

PLASMA PHYSICS AND PLASMA METHODS

UDC 537.52 PACS: 52.80.Wq
EDN: OYKPBD

Interfacial dynamics in a water-oil system during electrical breakdown

V. A. Panov*, A. S. Saveliev, and Yu. M. Kulikov

Joint Institute for High Temperatures of Russian Academy of Sciences, Moscow, 125412 Russia
** E-mail: panovvladislav@gmail.com*

Received 9.02.2026; revised 5.03.2026; accepted 27.04.2026

In this work, the formation of a conical water–transformer oil interface under high-voltage application to electrodes is studied experimentally and through numerical simulation in an axisymmetric three-dimensional formulation. The use of cylindrical electrodes with rounded ends enabled more detailed numerical modeling, with results that agree well with experimental data. It is shown that the phase-variable profiles and the normalized axial velocity profiles should be used to track the interface. The proposed simulation method can serve as a tool for the preliminary assessment of the resistance of high-voltage oil-filled equipment to local electrical breakdowns caused by potential moisture presence.

Keywords: conductive water, transformer oil, pulsed electric field, water cone, EHD flows.

DOI: 10.51368/2949-561X-2026-2-44-49

For citation: Panov V. A., Saveliev A. S., and Kulikov Yu. M., Applied Physics, No. 2, 44–49 (2026).

Introduction

Humidity in the oil insulation of high voltage equipment is a critical risk factor contributing to the initiation of dielectric breakdown, which can result in catastrophic consequences. A particular danger is the presence of elongated (compared to inter-electrode gaps in high voltage equipment) “water-oil” phase boundary, the behavior of which in a pulsed electric field has not been fully studied, and the mechanism of electrical breakdown requires a detailed study in this case.

The presence of even a trace amount of water in transformer oil reduces its dielectric strength. This is due to the fact that water, having a high dielectric permittivity ($\varepsilon \sim 80$) compared to that of oil ($\varepsilon \sim 2{,}2$) and low electrical conductivity, is polarized in an inhomogeneous field, forming ohmic bridges and locally increasing the electric field strength [1, 2]. The condensation of moisture on the inner surfaces of the tank or the formation of free water droplets can lead to local charge accumulation that initiates internal breakdown and emergency depressurization of the transformer’s active part.

Two classical breakdown mechanisms prevail in homogeneous dielectric liquids [3]. The streamer-leader (avalanche) breakdown is due to impact ionization and the development of fast tree-like channels (streamers). It is characteristic of pulsed voltage application (nanosecond to microsecond ranges) in strong fields (>100 kV/cm) and has been well studied [3, 4]. Its dynamic is similar to breakdown in dense gases, where electron emission of electrodes from the cathode and the formation of gas bubbles due to Joule heating play a crucial role [3–12]. Thermal breakdown occurs in weaker but long-lasting fields, where the heating of the liquid from leakage currents and conduction exceeds the heat removal resulting in thermal instability and the formation of a conductive channel.

A factor significantly complicating the situation is a presence of an interphase boundary (gas-liquid or liquid-liquid). Its presence leads to

a contrast in dielectric properties and the accumulation of polarization charges, which significantly reduces the overall gap electrical strength of the gap. In particular, for the oil-water boundary at an average field strength below 5 kV/cm, the development of classical streamers in the volume of any of the liquids is impossible [3], and the thermal mechanism in water is also not realized due to the capacitive nature of the initial current. Thus, electrohydrodynamic instability starts to play a dominant role.

When applying a pulsed electric field to the boundary of two immiscible liquids with different conductivities and permittivities, free charges are induced at this boundary. The interaction of the external field with these charges creates tangential electrostatic forces (pressure), which cause boundary instability according to the Tonks-Frenkel instability type [13]. This results in non-linear deformation of the boundary – the occurrence of pointed edges or a cellular structure; electrohydrodynamics currents – the formation of convective currents in both liquids; and the explosive growth of disturbances – when the critical voltage is exceeded, the edge from the side of the more conductive liquid (water) can stretch into a thin jet capable of quickly reaching the opposite electrode and causing gap closure. This process can occur orders of magnitude slower than streamer breakdown and lead to the gap closure.

The studies show that the pulse polarity, electrodes geometry, and the ratio of the conductivities of the liquids are key parameters determining the morphology of deformation and the threshold voltage [14–17].

In paper [18], an experimental and numerical study of the behavior of the "water-transformer oil" phase boundary was conducted, where a sphere acted as a high-voltage electrode. The simulation results showed a lag of about 1.4 times from the actual cone height, which was attributed to the two-dimensionality of the problem statement.

The purpose of this work is an experimental and numerical study of the behavior of the "water-transformer oil" phase boundary, where a cylinder with a working end in the form of a hemisphere acts as a high-voltage electrode. Such a statement makes possible a three-dimensional axisymmetric simulation, which was impossible with the previous electrode geometry due to numerical oscillations occurring at the sphere pole opposite to the liquid boundary. This problem does not occur in the case of a cylindrical electrode, and the simulation results match the experimental ones with good accuracy.

Experimental unit and mathematical modeling methods

The experimental unit used in this work is identical to the one in [18] except for the high-voltage electrode, which in this work was chosen to be cylindrical with a diameter of 7 mm, the working edge of which facing the water-oil phase boundary was made as a hemisphere of the same diameter. A brief description is presented below. To conduct the research, a layer of water (300 μS/cm) is poured into a transparent Plexiglas container and then a layer of transformer oil is poured on it. The thickness of the layers is selected in such a way that the phase boundary is between the upper and lower electrode and is equidistant from them. The grounded electrode, made of a 1.6 mm brass rod with a rounded edge at the working end, is placed in the water layer. A high-voltage electrode in the form of a brass rod with a diameter of 7 mm is immersed in the oil layer to a depth of 12 mm. The discharge gap is monitored using an MBS-10 microscope and a Phantom v2012 photocamera. The voltage pulse is formed using a semiconductor high-voltage commutator ("half-bridge" type) connected to storage capacitor. The commutator is capable of raising the potential of the high-voltage electrode to the required value (as well as lowering it to 0) in a time of about 100 ns.

The simulation is conducted in an axisymmetric setup in a cylindrical region into which two electrodes are inserted. The lower electrode has a radius of 0.8 mm, its height is 25 mm, and the rounded electrode tip radius is 0.4 mm. The lower electrode is immersed into the water to a depth of 3 mm. The external cylindrical surface is at a distance of 40 mm from the electrode axis. A 12 mm thick layer of oil is located above a 28 mm thick layer of water. A rounded electrode with a radius of 3.5 mm is completely immersed in it. Thus, its lower surface is at a distance of 3 mm from the media phase boundary. The lower electrode is grounded

(voltage $V = 0$ V), and a constant voltage equal to V = 3360, 3900, 4440 V is applied to the top one. The computational domain is additionally divided into several subareas which are covered by a grid with different characteristics. Namely, in areas where the phase composition does not change, a calculation mesh of triangles is used. In all other areas where the phase boundary moves, an orthogonal grid is set. Spatial discretization based on the finite element method is used to jointly solve the Poisson's equation, the Navier-Stokes equations and phase transport. The implicit Euler scheme with a variable time step is used for temporal discretization. The algorithm uses splitting by physical processes: at each time step, the electric field, the distribution of velocities and pressure in the resulting flow, as well as the movement of the phase boundary, are sequentially calculated. The phase boundary has a finite thickness and is modeled based on the Level-Set method [19]. The occurrence of the driving electrostatic force is due to the divergence of the Maxwell stress tensor in a medium with non-uniform dielectric permittivity.

Findings and Discussion

Fig. 1 shows records of the movement of water – transformer oil phase boundary under the influence of pulsed voltages with an amplitude of 3360, 3900, and 4440 V. In the first moment after the voltage is applied, the boundary deformation near the electrode axis occurs almost uniformly, as in the case of a spherical electrode [18]. Then the boundary acquires a noticeable curvature with a radius of a constant sign. At a height of about 1 mm, a sharp peak starts to form at the boundary (where the curvature radius changes its sign). Further water movement deep into the oil occurs due to the sharpening and stretching of the tip of the boundary. When the distance to the electrode is reduced to approximately 0.2 mm, small droplets begin to separate from the tip of the cone at: *a*) 42.5 ms, *b*) 34.286 ms, and *c*) 29 ms, respectively, and form a stream that reaches the electrode surface. Electrical breakdown (34.994 ms in Fig. 1*b*) is initiated as a result of the simultaneous separation and stretching of many droplets, which consequently form a thin water channel that completely closes the gap or appears at distances from each other sufficient to break through the oil gap. The formation of a plasma channel is only observed at the thin top part of the cone, where the current density is sufficient for the thermal initiation mechanism. As the voltage increases, the total process time decreases, and the shape of the phase boundary goes through a similar evolution (see, for example, 34.826, 29, and 25 ms for *a*), *b*) and *c*), respectively).

Fig. 2 shows the curves of the cone vertex position. “E” and “m” indices refer, respectively, to the results of the experiment and modeling. The three-dimensional problem formulation provides a much better match with the experiment compared to the two-dimensional one [18].

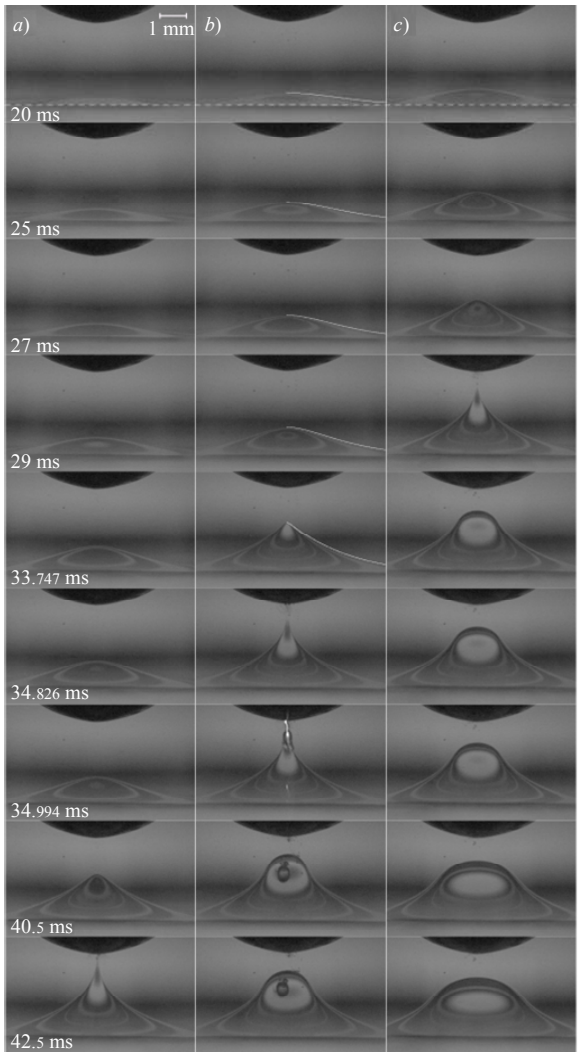

Fig. 1. Motion record of the water-transformer oil boundary in a vertical electric field at a voltage of a) 3360, b) 3900, and c) 4440 V. Results of the boundary position modeling are indicated with a white line for the case of 3900 V at the 20–33.747 ms frames. The dotted line indicates the location of the unperturbed boundary

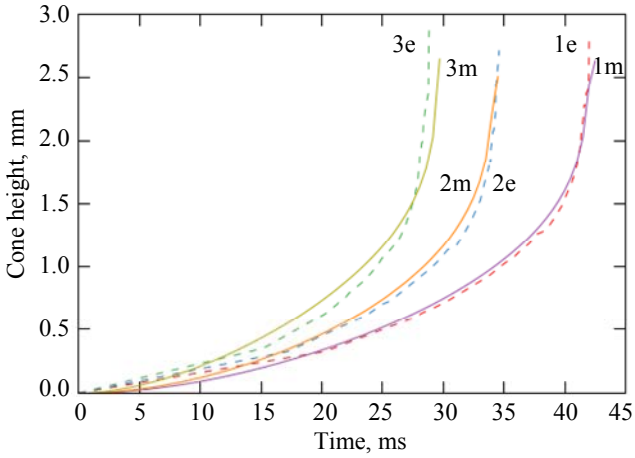

Fig. 2. Graphs of the dependencies of the cone vertex position on the time of voltage supply in the experiments (with the "e" mark) and numerical modeling (with the "m" mark) at a voltage of 1) 3360, 2) 3900 and 3) 4440 V

The vertex movement occurs with a constant increase in speed (curve 2 in Fig. 3) due to a constant increase in forces from the electric filed side, which increase with a decrease in the distance between the vertex and the surface of the high-voltage electrode.

Fig. 3 shows the dynamics of the normalized (to the maximum) cone vertex height H values, the velocity of the vertex movement υ and the volume V of the cone's visible part for the slowest case of 3360 V at the stages of growth and decline of the cone. It is noteworthy that the maximum values are not reached at the same time. The first to reach its peak is the maximum velocity, which is about 1 m/s. This is due to the beginning of liquid spraying from the tip which slows down the progress of the clearly visible part of the vertex. The maximum value of $H_{\max}$ height is 2.86 mm, which is less than the initial distance of 3 mm, also due to the spraying and de-energizing of the electrode before the breakdown. Much later, the maximum volume $V_{\max} = 41$ mm^3 of the visible part of the cone is reached, which is explained by the inertia of the liquid moving inside the cone. This value is estimated from the bottom because over time, an increasing amount of liquid appears outside the visible area. The presented picture is qualitatively repeated for all voltage cases.

Fig. 4 shows an extended comparison of experimental and numerical results for 3360 V case.

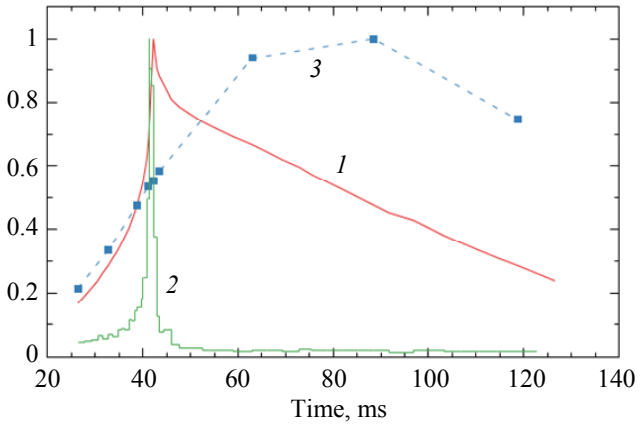

Fig. 3. Graphs of the dependencies of the cone vertex position H/H_{max} (1), its velocity υ/υ_{max} (2) and the volume V/V_{max} of the cone (3) normalized to their maximum values at the stages of growth and decline. The voltage is 3360 V; the voltage pulse decreases at t = 42.2 ms. $(H_{max}, \upsilon_{max}, V_{max}) = (2.86$ mm, 1 m/s, 41 mm$^3)$

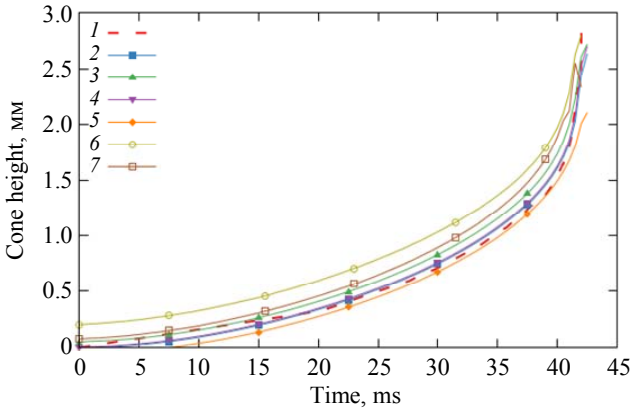

Fig. 4. Graphs of dependence of the cone vortex position H (1) in the experiment (3360 V) and the modeled values $\varphi = 0.5$ (2), $\upsilon_z/\max\{\upsilon_z\} = 0.1$ (3), $\upsilon_z/\max\{\upsilon_z\} = 0.5$ (4), $\upsilon_z/\max\{\upsilon_z\} = 0.9$ (5), $\min\{F_z\}$ (6), and $\max\{F_z\}$ (7)

For each calculation, the axial distribution of three quantities (along the *z-axis*) is considered: the profile of the phase variable φ, the profile of the z-component of the electric field intensity, the profile of the z-component of velocity (V_z), and the profile of the z-component of the ponderomotive volumetric force (F_z). For the phase variable in the range of values $\varphi = [0, 1]$, a number of N level lines is selected, according to which a discrete set is determined φ_i, excluding the extreme values 0 and 1. At each time interval t_i (for which the results were obtained) the position of the nearest points on the profile $\varphi = \varphi(z)$ for a set of levels φ_i, $i = 0$, N-1 is

determined. The change in the positions of points over time $z_i = z_i(t)$ allows for the construction of a set of corresponding curves and the identification of numerical results for a certain curve to compare with the experiment. The main reason why several quantities are considered is that the final thickness of the phase boundary significantly exceeds its physical analog. Moreover, it is subject to "blurring" during the calculation due to model diffusion. In the case of the velocity V_z, the profile is normalized to the maximum at each time interval, and the V_z level lines are changed in the same way. The behavior of the E_z levels turns out to be similar φ, and therefore, is not considered. The force profile undergoes very strong changes in the process of calculation both in amplitude (its maximum values change by several orders of magnitude) and in shape. Setting a set of levels for this value turns out to be unreasonable. However, one can track the movement of its front. The first obvious "marker" is the F_z maximum position at each time point. Considering the force profiles immediately after the voltage is applied, it can be noticed that spatial discretization by the finite element method leads to the occurrence of nonmonotonicity and with further water displacement towards the high-voltage electrode, the F_z distribution is characterized by strong inhomogeneities that can propagate at a different rate than the "material" variable φ. As an additional criterion for the displacement of the phase boundary, the location of the last local minimum on the $F_z = F_z(t)$ profile can be considered. The best approximation is provided by the profile along the midline $\varphi = 0.5$, the level line $\varphi = 0.1$ gives an overestimated value of the cone vertex and $\varphi = 0.9$ – an underestimated one during the entire calculation. Similarly to the phase variable, the level line $V_z/\max\{V_z\} = 0.9$ for velocity gives an underestimated value of the cone vertex for each time interval. In the initial stage ($t < 20$ ms) the best approximation is given by the level line $z_{Vz} = 0.0909$, and then the best approximation is given by the midline throughout the calculation. The use of the F_z maximum and the local minimum closest to the high-voltage electrode as the phase boundary motion markers gives underestimated values of the cone vertex and is unsatisfactory.

Conclusions

The motion of the phase boundary between water and transformer oil in a vertical electric field was studied experimentally and using numerical modeling. Data were obtained on the velocity of the phase boundary, the volume of the involved liquid, and the dynamics of the vortex of the water cone at the stage of its growth when the voltage was applied, as well as at the stage of its decline, It was shown that at a ratio 2:1 of the diameter D of the high-voltage electrode to the distance l to the phase boundary, the geometry of the electrode's working end defines the nature of the boundary deformation, while its height does not significantly affect the motion and charge development.

The transition from the two-dimensional to the three-dimensional axisymmetric simulation allowed to significantly bring the experimental and numerical results for the dependence of cone vertex position on time into close agreement. Changing the shape of the high-voltage electrode from spherical to cylindrical with similar hemisphere on the working end allowed for the optimization of computational time (despite the three-dimensional formulation) by completely eliminating spurious currents appearing at the sphere pole opposite to the discharge gap; these currents have little effect on the movement of the liquid phase boundary, yet, they require computing resources comparable to the problem under consideration.

Despite a large number of model hypotheses and limitations related to the finite thickness of the phase boundary, empirical coefficients in the phase variable transfer model, and an approximate form of recording the volumetric force, the model can generally correctly describe the motion of the "water-oil" boundary towards the high-voltage electrode. The best ways to represent this motion are the level lines of the phase variable ϕ and the normalized axial velocity $V_z/\max\{V_z\}$. The description in terms of the local extreme points of the ponderomotive volumetric force $F_{es,z}$ is unsatisfactory; however, it shows the degree of field disturbance of the volumetric force due to the finite thickness of the phase boundary.

REFERENCES

1. Sun C., Ohodnicki P. R., and Stewart E. M., IEEE Sens. J. **17** (18), 5786–5806 (2017).
2. Hao J., Chen G., Liao R., Yang L., and Tang C., IEEE Trans. Dielectr. Electr. Insul. **19**, 1456–1464 (2012).
3. Ushakov V. Ya., Klimkin V. F., and Korobeynikov S. M. Impulse Breakdown of Liquids. Berlin Heidelberg New York, Springer, 2007.
4. Lesaint O., J. Phys. D: Appl. Phys. **49** (14) 144001 (2016).
5. Chng T. L., Brisset A., Jeanney P., Starikovskaia S. M., Adamovich I. V., and Tardiveau P., Plasma Sources Sci. Technol. **28** (9), 09LT02 (2019).
6. Ding C., Khomenko A. Y., Shcherbanev S. A., and Starikovskaia S. M., Plasma Sources Sci. Technol. **28** (8), 085005 (2019).
7. Kosarev I. N., Starikovskiy A. Y., and Aleksandrov N. L., Plasma Sources Sci. Technol. **28** (1), 015005 (2019).
8. Liu Z., Hara K., and Shneider M. N., Phys. Fluids. **35** (4), 042101 (2023).
9. Shneider M. N. and Pekker M. Liquid Dielectrics in an Inhomogeneous Pulsed Electric Field. Institute of Physics Publishing, 2019.
10. Starikovskiy A. Y. and Aleksandrov N. L., Plasma Sources Sci. Technol. **28** (9), 095022 (2019).
11. Starikovskiy A. Y. and Aleksandrov N. L., Plasma Sources Sci. Technol. **29** (7), 075004 (2020).
12. Starikovskiy A. Y., Aleksandrov N. L., and Shneider M. N., Phys. Rev. E. **103** (6), 063201 (2021).
13. Tonks L., Phys. Rev. **48**, 562 (1935).
14. Aleksandrov G. N., Ivanov V. L., Kadomskaya K. P., Kozyrev N. A., Kostenko M. V., Kuchinskij G. S., Polovoj I. F., Ryabov B. M., and Hoberg V. A. Tekhnika vysokih napryazhenij. Moscow, Vysshaya shkola, 1973 [in Russian].
15. Panov V. A., Vasilyak L. M., Vetchinin S. P., Pecherkin V. Ya., and Saveliev A. S., Plasm. Phys. Rep. **44** (9), 882–885 (2018).
16. Panov V. A., Vasilyak L. M., Vetchinin S. P., Pecherkin V. Ya., and Son E. E., Plasm. Phys. Rep. **42**, 1074 (2016).
17. Panov V. A., Pecherkin V. Ya., Vasilyak L. M., Vetchinin S. P., and Saveliev A. S., Plasm. Phys. Rep. **47**, 623 (2020).
18. Panov V. A., Kulikov Yu. M., Pecherkin V. Ya., Vasilyak L. M., and Saveliev A. S., Applied Physics, No. 6, 5–10 (2023) [in Russian].
19. Olsson E. and Kreiss G., J. Comput. Phys. **210**, 225–246 (2005).

About authors

Panov Vladislav Aleksandrovich, Candidate of Physical and Mathematical Sciences, senior research scientist, Joint Institute for High Temperatures of Russian Academy of Sciences (125412, Russia, Moscow, 13, Izhorskaya st., bldg. 2). E-mail: panovvladislav@gmail.com SPIN code: 5821-2776, AuthorID: 755538

Saveliev Andrey Sergeevich, Candidate of Physical and Mathematical Sciences, senior research scientist, Joint Institute for High Temperatures of Russian Academy of Sciences (125412, Russia, Moscow, 13, Izhorskaya st., bldg. 2). E-mail: fisteh@mail.ru SPIN code: 6888-7369, AuthorID: 866343

Kulikov Yuri Matveevich, Candidate of Physical and Mathematical Sciences, senior research scientist Joint Institute for High Temperatures of Russian Academy of Sciences (125412, Russia, Moscow, 13, Izhorskaya st., bldg. 2). E-mail: kulikov-yurii@yandex.ru SPIN code: 7719-8459, AuthorID: 1130937

PHYSICAL SCIENCE OF MATERIALS

UDC 621.315.592 PACS: 81.
EDN: PIREAA

Possibilities of a planetary machining scheme for group grinding and polishing of InSb wafers and matrix modules

V. A. Ul'karov[1*], A. A. Trofimov[1,2], N. A. Sarkisov[1], V. O. Kuzin[1], K. Yu. Arbuzov[1], I. D. Razmahnin[1], A. N. Kobysh[2], R. Yu. Kozlov[3,4], and M. S. Nestyurkin[3,4]

[1] *RD&P Center ORION, JSC, Moscow, 111538 Russia*
[*] *E-mail: ulkarov@yandex.ru*
[2] *MIREA – Russian Technological University, Moscow, 119454 Russia*
[3] *Giredmet, JSC, Moscow, 111524 Russia*
[4] *University of Science and Technology MISIS, Moscow, 119049 Russia*

Received 5.03.2026; revised 20.03.2026; accepted 27.04.2026

During serial production, one of the key aspects, along with increasing productivity while maintaining product quality and reproducibility, is the desire to reduce costs and labor intensity. Single-sided lapping and polishing operations typically use an orbital machining system with individual loading. Switching to a planetary system potentially offers the optimal solution; however, it requires high precision and a significant upgrade in equipment design.
This paper proposes a planetary scheme of lapping and polishing, develops design and technological solutions, and conducts a series of processes on InSb wafers and matrix modules. Measurement results demonstrate the potential for increased labor productivity and yield while simultaneously reducing material costs.

Keywords: planetary lapping and polishing, photodetector array, lapping and polishing, InSb.

DOI: 10.51368/2949-561X-2026-2-50-55

For citation: Ul'karov V. A., Trofimov A. A., Sarkisov N. A., Kuzin V. O., Arbuzov K. Yu., Razmahnin I. D., Kobysh A. N., Kozlov R. Yu., and Nestyurkin M. S., Applied Physics, No. 2, 50–55 (2026).

The photosensitive indium antimonide (InSb) material is one of the main materials in the industrially oriented production of matrix photodetectors for the mid-wave IR range and the photoreceiving devices based on them, which are mass-produced by various domestic enterprises [1].

The manufacturing technology for such devices is well-established; however, during mass production, one of the key factors, along with increasing productivity while preserving the quality of products and the reproducibility of results, is the desire to reduce costs and labor intensity, which motivates the search for new solutions and the modernization of individual processes within the manufacturing workflow. For one-sided grinding and polishing operations, as a rule, an orbital machining pattern with single-piece loading is used. Switching to a planetary pattern is potentially the best solution; however, it requires high accuracy and the structural modernization of the equipment. In this paper, we investigated separate operations at the stage of material processing to establish the possibility of their optimization to increase productivity.

The processing of bulk InSb wafers is conducted piece by piece using a loose abrasive and includes sequential grinding on both sides using abrasive suspensions with different grain sizes [2, 3]. The wafers are polished on each side after grinding. The schematic processing procedure is shown in Fig. 1.

Productivity gains while reducing the costs of the consumables used are provided by group processing methods [4]. To implement the group

processing shown in the scheme in Fig. 1, it is proposed to use a disk carrier with the maximum possible diameter (112 mm) for the bonding of wafers, which allows the existing equipment and tooling for grinding and polishing to work with it.

Knowing the current diameter of the processed wafers (50.8 mm) and applying the solution to the two-dimensional packing problem ("packing circles in a circle") obtained in 2014 by E. Specht [5] and reviewed by domestic authors [6], it was found that a 112 mm carrier disk accommodates 3 InSb wafers with a diameter of 50.8 mm (Fig. 2).

To assess the viability of the proposed solution, the group processing of the wafers was conducted by grinding using standard tooling. An Al_2O_3 abrasive with a grain size of 3 μm diluted in deionized water was used. The total load on the samples was 1.35 kg (23 g/cm^2), the rotation speed of the grinding plate was set at 15 rpm, and the processing time was 10 min. The profile of the grinding plate surface (diameter of 300 mm) is shaped as a convex surface (+ 3 μm) to compensate for the difference in material removal in the central part of the disk carrier and at the edges due to the difference in angular velocities during grinding, since in this processing model using three wafers on one disk carrier, the InSb wafers are located close to each other. The measurement of the wafers' thickness was performed on a Logitech NCG-2 (Scotland) non-contact gauge as shown in Fig. 3.

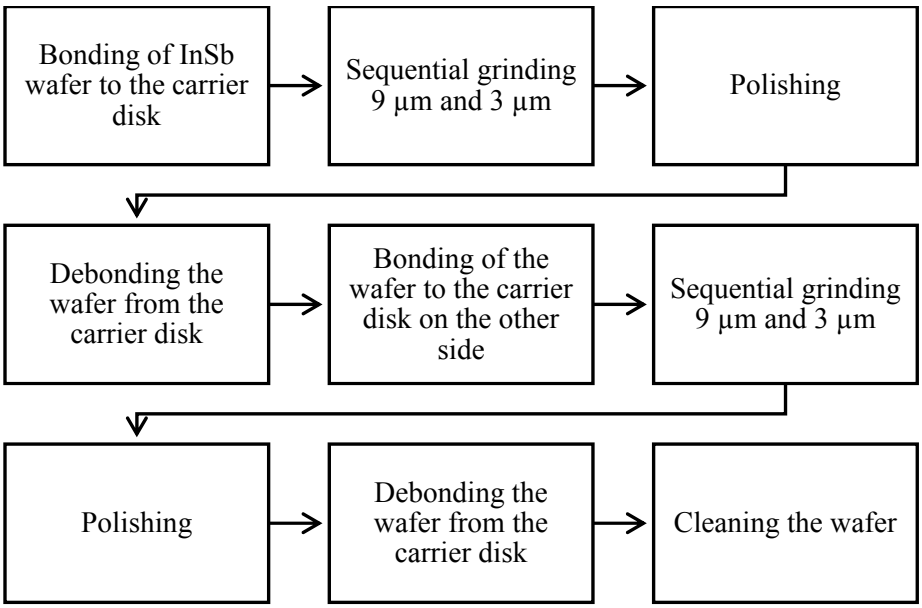

Fig. 1. The scheme of InSb wafers processing during the grinding and polishing stages

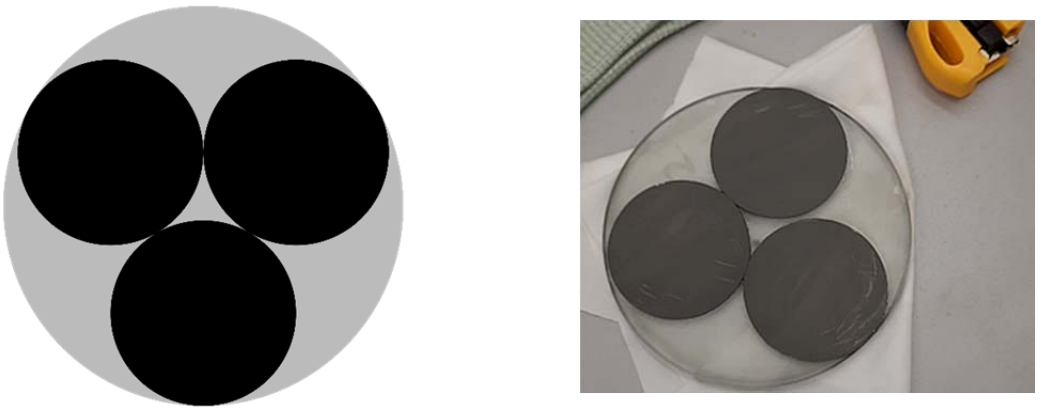

a) *b*)

Fig. 2. Illustration of the solution of the two-dimensional packing problem for a disk carrier with a diameter of 112 mm and InSb wafers with a diameter of 50.8 mm (a) and a photo of the InSb wafers bonded to the disk carrier (b)

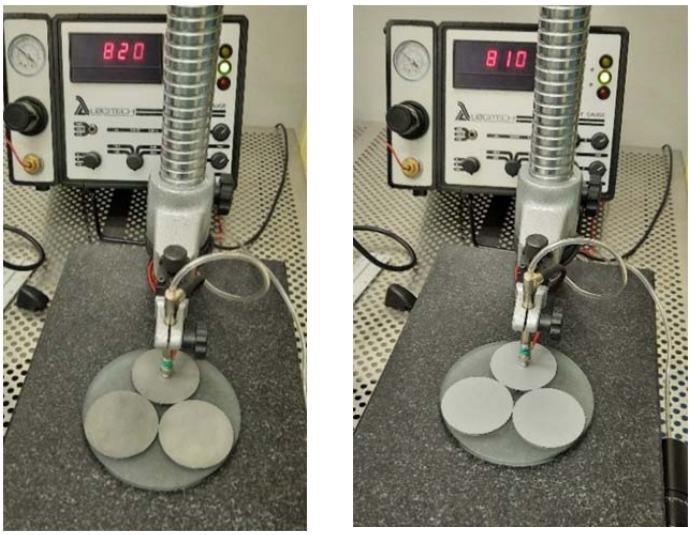

a) b)

Fig. 3. Simultaneous processing by grinding of three InSb wafers with a diameter of 50.8 mm on a glass disk carrier with a diameter of 112 mm; a) measurement of thickness before processing, b) measurement of thickness after processing

The results of processing and thickness measurements before and after processing, as well as the measurement scheme for several points on each wafer, are shown in Table 1.

The flatness of the treated surfaces of the InSb wafers was measured by a contact method on a Bruker DektakXT (Germany) profilometer with a scan length of 49 mm (Fig. 4).

Analyzing the measurement results, it is noticeable that deviations from flatness do not exceed 0.5 μm. One can notice a slight edge roll-off of 0.25 μm, probably due to an insufficient convexity of the grinding plate profile selected for the processing during tooling preparation. Nevertheless, the results are in the permissible range of deviations that is currently applied to the piece-by-piece processing of wafers (up to 3 μm).

Thus, the proposed solution for the group processing of InSb wafers in the mass production of matrix photodetectors for the mid-wave IR range shows the possibility of its application for process optimization.

After grinding and polishing, the InSb wafers are subjected to the following operations in the manufacturing workflow aimed at the formation of matrix photosensitive elements and their docking with a silicon LSI. The fabricated matrix photosensitive modules are supplied for thinning, which is a complex technological process necessary to improve the spatial resolution and increase the quantum efficiency of the photodetector device.

Table 1

Measurement results of wafers' thickness before and after grinding (μm)

Number of sample / Point measurements		A	V	C	D	E	Location of measurement points on each sample
9	before	817	819	822	821	820	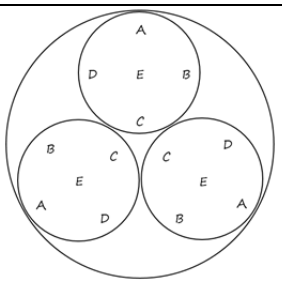
	after	809	809	810	809	810	
10	before	816	817	821	818	818	
	after	808	808	810	810	809	
11	before	817	816	819	819	818	
	after	808	808	810	808	809	

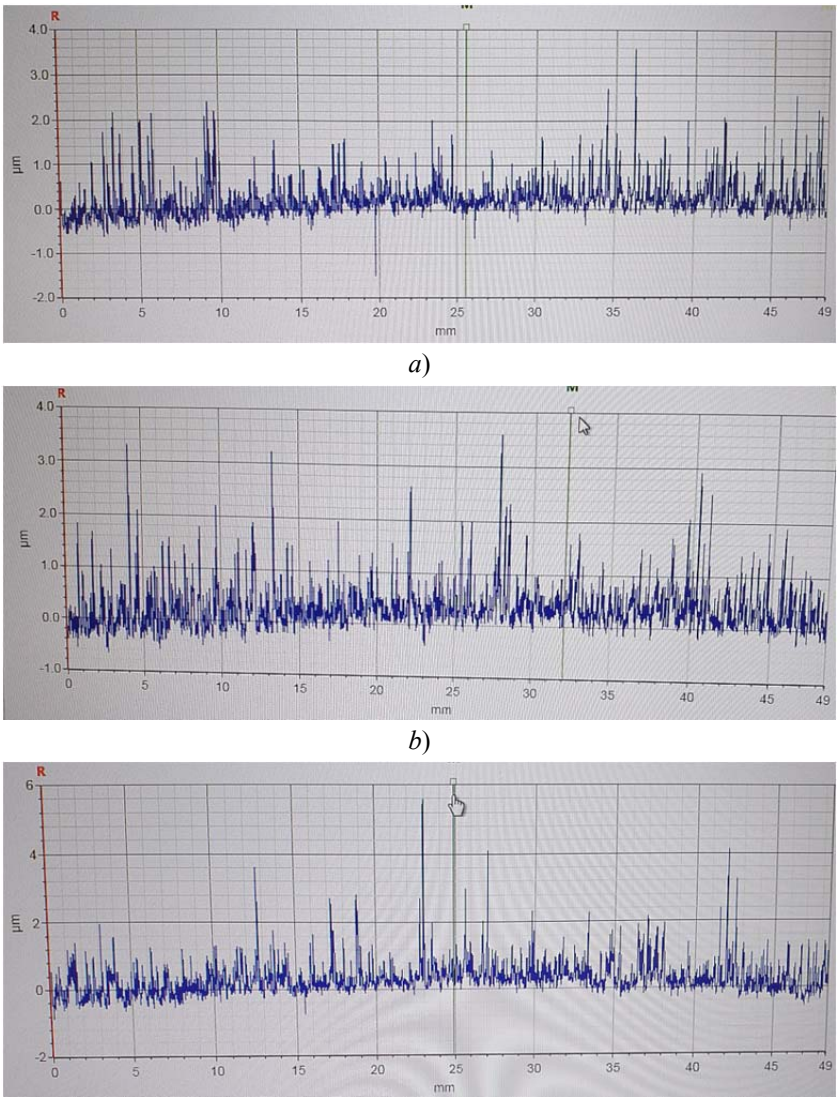

Fig. 4. The results of flatness measurements of the processed InSb wafers surfaces: a) – sample No. 9; b) – sample No. 10; c) – sample No. 11

Currently, at the grinding and polishing stage, the module thinning is conducted piece by piece [7]. To implement the possibility of processing by the group method (3 photosensitive modules simultaneously) a design and technological solution was developed, a prototype model of a new component was made, and the tooling of the polishing equipment was modified (Fig. 5).

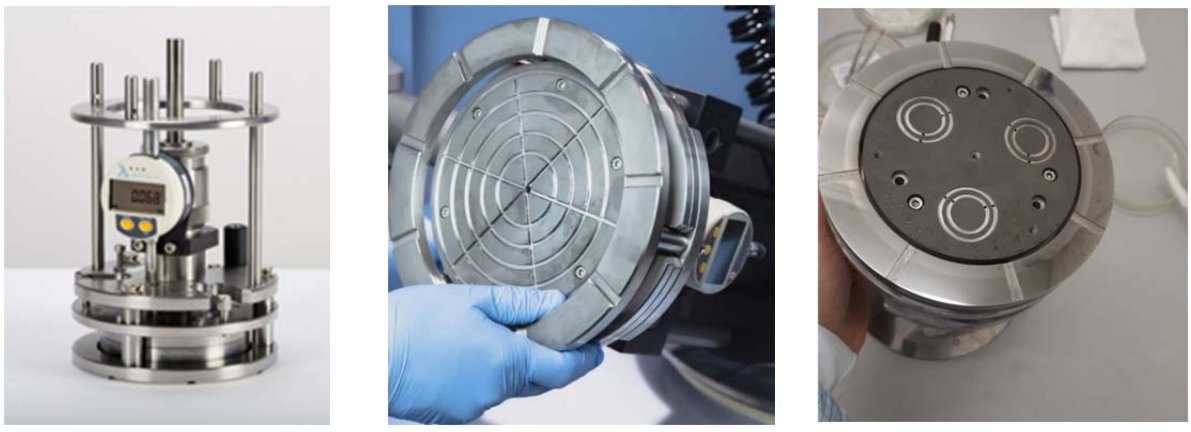

a) *b*) *c*)

Fig. 5. Tooling for the polishing unit: a) – appearance; b) – standard vacuum chuck of the tooling; c) – tooling modification by adding a prototype model of a new vacuum chuck

The prototype model of a new component is coupled in a certain way with the standard tooling for polishing to ensure maximum surface flatness, which is an important factor for the subsequent group processing of photosensitive modules. The modes and other processing parameters described in paper [7] did not change, except for disabling the reciprocating motion of the tooling along the polishing pad during processing. Such movement during piece-by-piece polishing allows one to achieve the best results in the surface flatness of the processed sample. In the case of group processing, polishing is conducted according to a planetary scheme, which ensures the improvement of the qualitative characteristics of the surface during finishing, high accuracy, and uniform material removal due to the complex spatial movement of each photosensitive module [8, 9].

As a result of the experimental group processing of the photosensitive modules, the thinning was conducted to a thickness of 30–60 μm. After processing, the measurement results of the flatness of the modules' surfaces, obtained on a Bruker DektakXT (Germany) profilometer, are shown in Fig. 6. The data show that the deviation from flatness at the target distance (highlighted by vertical green and red lines) does not exceed 2–3 μm. The difference in the thicknesses of the processed modules is due to the difference in the thicknesses of the special holders for the modules, which are made of leucosapphire. These holders require their thickness to be adjusted to a uniform size, which ensures the uniform removal of material from all modules in a single process.

Thus, as a result of the conducted studies aimed at increasing the efficiency of the industrially oriented production of matrix photodetectors for the mid-wave IR range, solutions for the group processing of InSb wafers and photosensitive modules were proposed and tested. It was established that the quality of the

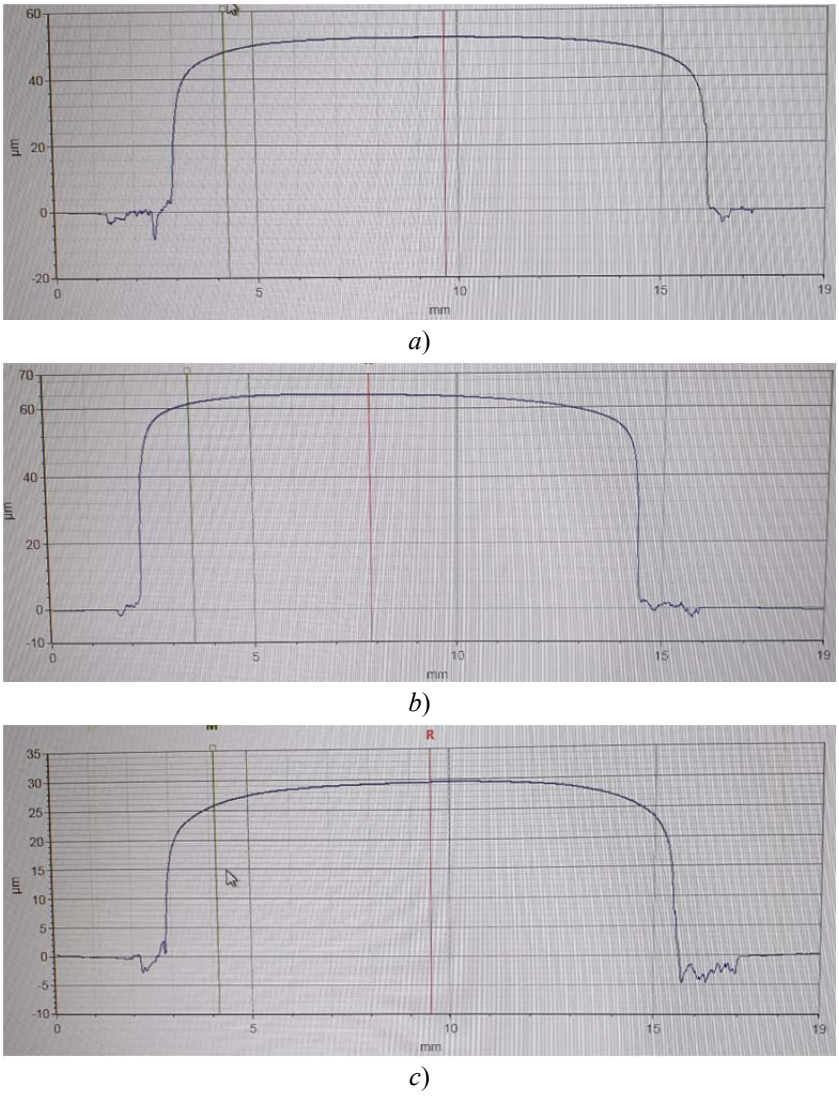

Fig. 6. Measurement results of the surface flatness of InSb photosensitive modules docked with a silicon integrated readout circuit, after group processing: a) – sample No. 4536; b) – sample No. 4571; c) – sample No. 4573

products obtained during group processing is not inferior in a number of parameters to that obtained during piece-by-piece processing. At the same time, it is possible to increase labor productivity and throughput, while simultaneously reducing the costs of consumables.

However, there are still some unsolved problems within this framework, particularly:

– conducting the full processing of InSb wafers, including material removal from both wafer sides, as well as polishing;

– the preparation of special holders for modules made of leucosapphire and having the same thickness;

– conducting the complete module processing cycle using the new special holders;

– conducting a series of processes for both wafer and module processing to achieve the reproducibility of results;

– the implementation of the obtained and justified solutions into mass production.

Despite a number of unsolved problems, the authors consider it appropriate to continue further studies to achieve positive results in the interests of the industrial production of domestic matrix photoreceiving elements and the photoreceiving devices based on them.

REFERENCES

1. Burlakov I. D. and Startsev V. V. Materialy XXVII Mezhdunarodnoj nauchno-tekhnicheskoj konferencii po fotoelektronike i priboram nochnogo videniya. Moscow: RD&P Center ORION, JSC, 2024, pp. 24–27 [in Russian].
2. Trofimov A. A., Kozlov R. Yu., Krivobok V. S., Lopatin V. V., Ul'karov V. A., Molodcova E. V., Pavlov P. V., Pavlova O. S., Kosyakova A. M., Komarovskij N. Yu., Nestyurkin M. S., Klekovkin A. V., Minaev I. I., Eroshenkov V. V., Atrashkov A. S., and Kovin Ya. A., Applied Physics, No. 5, 46–56 (2024) [in Russian].
3. Ul'karov V. A., Trofimov A. A., Pavlova O. S., Novikov I. V., Sarkisov N. A., and Kuzin V. O., Usp. Prikl. Fiz. (Advances in Applied Physics) **12** (5), 456–464 (2024) [in Russian].
4. Kozlov R. Yu., Trofimov A. A., Molodcova E. V., Abramova E. N., Pavlov P. V., Pavlova O. S., Nestyurkin M. S., and Shchenikov N. V., Pribory, No. 12, 32 (2024) [in Russian].
5. Specht E. The best known packings of equal circles in a circle (complete up to N = 2600).
6. Kazakov A. L. and Lebedev P. D., Vychislitel'nye metody i programmirovanie **16**, 307–317 (2015) [in Russian].
7. Mirofyanchenko E. V., Mirofyanchenko A. E., and Popov V. S., Applied Physics, No. 2, 46–52 (2020) [in Russian].
8. Zverovshchikov V. Z. and Zotov E. V., Izvestiya MGTU «MAMI», No. 2 (8), 209–213 (2009) [in Russian].
9. Artemov I. I., Zverovshchikov A. E., and Martynov A. N., Izvestiya vysshih uchebnyh zavedenij. Povolzhskij region, Tekhnicheskie nauki. Mashinostroenie i mashinovedenie, No. 4 (28), 199–211 (2013).
10. Boltar' K. O., Vlasov P. V., Eroshenkov V. V., and Lopuhin A. A., Applied Physics, No. 4, 45–50 (2014) [in Russian].
11. Babu S. V. Advanced in chemical mechanical planarization (CMP). Woodhead Publishing, 2016.

About authors

Ul'karov Vadim Airatovich, Candidate of Technical Sciences, Lead Engineer RD&P Center ORION, JSC (111538, Russia, Moscow, Kosinskaya st., 9). E-mail: ulkarov@yandex.ru

Trofimov Alexander Aleksandrovich, Candidate of Technical Sciences, Assistant Professor, Head of the department the development Materials RD&P Center ORION, JSC (111538, Russia, Moscow, Kosinskaya st., 9); MIREA – Russian Technological University (119454, Russia, Moscow, Vernadsky Ave., 78). E-mail: aa-trofimov@yandex.ru SPIN code: 3716-5536, AuthorID: 818356

Sarkisov Nikita Andreevich, Engineer Cat. 2, RD&P Center ORION, JSC (111538, Russia, Moscow, Kosinskaya st., 9). E-mail: nsarkisov@mail.ru

Kuzin Vladislav Olegovich, Engineer Cat. 2, RD&P Center ORION, JSC (111538, Russia, Moscow, Kosinskaya st., 9).

Arbuzov Kirill Iurevich, Engineer, RD&P Center ORION, JSC (111538, Russia, Moscow, Kosinskaya st., 9).

Razmahnin Ivan Dmitrievich, Engineer Cat. 2, RD&P Center ORION, JSC (111538, Russia, Moscow, Kosinskaya st., 9).

Kobysh Alina Nikolaevna, Candidate of Technical Sciences, head of the department of optoelectronic devices and systems MIREA – Russian Technological University (119454, Russia, Moscow Vernadsky Ave., 78). E-mail: kobysh@mirea.ru SPIN code: 8836-0683, AuthorID: 514026

Kozlov Roman Yurievich, head of laboratory, Giredmet, JSC (111524, Russia, Moscow, Elektrodnaya st., 2, bld. 1); University of Science and Technology MISIS (119049, Russia, Moscow, Leninsky Prospekt, 4, bld. 1). E-mail: RYKozlov@rosatom.ru SPIN code: 7324-5403, AuthorID: 1302882

Nestyurkin Mikhail Sergeevich, division manager, Giredmet, JSC (111524, Russia, Moscow, Electrodnaya st. 2/1); University of Science and Technology MISIS (119049, Russia, Moscow, Leninsky Prospekt, 4, bld. 1). SPIN code: 1217-6079, AuthorID: 1341074

PHYSICAL SCIENCE OF MATERIALS

UDC 53.083.4 PACS: 73.50.Lw
EDN: LJYRUZ

Thermo-EMF of nanosized In_2O_3/SnO

A. S. Terekhova*, L. A. Zelensky, and S. V. Smirnov

Tomsk State University of Control Systems and Radioelectronics, Tomsk, 634050 Russia
** E-mail tas18102004@mail.ru*

Received 27.10.2025; revised 21.11.2025; accepted 27.04.2026

The results of studies of differential thermo-EMF and Seebeck coefficient of nanosized In_2O_3/SnO (ITO) films obtained by magnetron sputtering of a compact target are presented. The dependence of the thermoelectric coefficient of films on temperature is shown, and its correlation with the temperature dependence of electrical conductivity is explained. An automated device for measuring the thermo-EMF of films and distributing it over the surface of the plate in the temperature range from 300 to 450 K has been designed. The results obtained allow us to predict the possibility of further use of ITO films in electronics.

Keywords: ITO films, thermo-EMF, Seebeck coefficient, Fermi level, charge carrier concentration.

DOI: 10.51368/2949-561X-2026-2-56-60

For citation: Terekhova A. S., Zelensky L. A., and Smirnov S. V., Applied Physics, No. 2, 56–60 (2026).

Introduction

Transparent conducting In_2O_3/SnO (ITO) films are widely used as a primary material for optoelectronic devices, biosensors, electrochemical analysis sensors, and temperature sensors. Since thin ITO films in all the above-mentioned applications are used in various combinations with metallic and semiconducting materials over a wide temperature range, the problem of accounting for the thermo-EMF arising at their contact arises. The thermo-EMF is a critical characteristic of metals and semiconductors. Knowing its value allows one to calculate their electrophysical characteristics, such as the Seebeck coefficient, the position of the Fermi level, the charge carrier concentration, and the density of states in the conduction band [1, 2].

Therefore, the aim of this work is to measure the intrinsic thermo-EMF coefficient of ITO films, which will make it possible to predict the potential for further application of these films in electronics.

The Seebeck coefficient S_{AB} for two contacting materials is determined by the formula:

$$S_{AB} = \frac{dU}{dT} = \alpha_A - \alpha_B, \quad (1)$$

where α_A and α_B are the thermo-EMF coefficients of materials A and B, respectively.

As a rule, thermo-EMF coefficients are taken relative to lead or platinum, since it is considered that these materials do not generate a potential difference under a temperature gradient, and their coefficients are known quantities for many metals. Thus, by measuring the Seebeck coefficient of the contact of an ITO film with a metal whose thermo-EMF coefficient is known, one can calculate the intrinsic thermo-EMF coefficient of the film.

In ITO films, electrical conductivity is realized both through delocalized states near the Fermi level, caused by the degeneracy of the semiconductor, and through hopping via localized states, which are oxygen vacancies.

In the low-temperature range (10–100 °C), ITO films represent a degenerate semiconductor with a high degree of amorphization. In this case, the most suitable formula for determining the thermo-EMF is that proposed by Mott:

$$\alpha = \frac{\pi^2 \cdot k^2 \cdot T}{3} \cdot \left(\frac{d\left(\ln \sigma\right)}{dE} \right)_{E=E_f} \qquad (2)$$

where α is the thermo-EMF coefficient, $k = 1.38 \times 10^{-23} \dfrac{\text{J}}{\text{K}}$ is the Boltzmann constant, T is the temperature, E_f is the position of the Fermi level relative to the bottom of the conduction band, and σ is the electrical conductivity.

From formula (2), the position of the Fermi level relative to the bottom of the conduction band can be determined:

$$E_c - E_f = \frac{\pi^2}{3} \cdot \frac{k^2 \cdot T}{q} \cdot \frac{1}{\alpha}. \qquad (3)$$

Then, using the Burstein–Moss formula, the electron concentration in the conduction band can be calculated:

$$n = \frac{8 \cdot \pi \cdot \left(3 \cdot m_e^*\right)^{\frac{3}{2}}}{3 \cdot h^3} \cdot \left(E_f - E_c\right)^{\frac{3}{2}}, \qquad (4)$$

where m_e^* is the effective electron mass, and $h = 6{,}63 \times 10^{-34}\,\text{J} \cdot \text{s}$ is the Planck constant.

However, at higher temperatures, electrical conductivity in ITO films begins to occur via a hopping mechanism. In this case, the energy levels of oxygen vacancies are degenerate, i.e., they have approximately the same energy, which facilitates the formation of a band through which electrical conductivity takes place. Then the temperature dependence of the thermo-EMF can be represented by the following expression:

$$\alpha = \omega_1 \cdot \left(-\frac{\pi^2}{3} \cdot \frac{k^2 \cdot T}{q} \cdot \frac{1}{E_F} \right) + \\ + \omega_2 \cdot \left(-\frac{k}{q} \cdot \left(\frac{\pi - 2}{\pi} \cdot \frac{\Delta E_a}{k \cdot T} + \frac{2 \cdot \pi}{3} \cdot k \cdot T \right) \cdot \frac{1}{E_F} \right), \qquad (5)$$

where ω_1 is the contribution of the degeneracy of the energy levels of oxygen vacancies to the thermo-EMF value, ω_2 is the contribution of the hopping conductivity mechanism to the thermo-EMF value, and ΔE_a is the electrical conductivity activation energy, which can be found from its temperature dependence:

$$\sigma = \sigma_0 \cdot \exp\left(-\frac{E_a}{2kT} \right). \qquad (6)$$

The most common method is measuring the Seebeck coefficient of thin ITO films by creating a thin-film thermocouple with a reference material, for example, ITO-tungsten [4–8].

Experimental Setup

In this work, a tungsten wire with a diameter of 1 mm is used as the measurement electrodes. The movement of the measurement electrodes is performed using four stepper motors with a lead screw. To increase positioning accuracy, the control drivers use a microstepping function with a 1/16 division; the positioning accuracy in this case equals ±5 μm.

Thermo-EMF voltage measurements of nanoscale conducting films are carried out at four points, which allows the measurement accuracy to be increased and the thermo-EMF distribution profile over the sample surface to be presented. Also, the developed test bench provides the capability to study the dependence of the thermo-EMF voltage on temperature. A 3D model of the measuring part of the setup is presented in Figure 1.

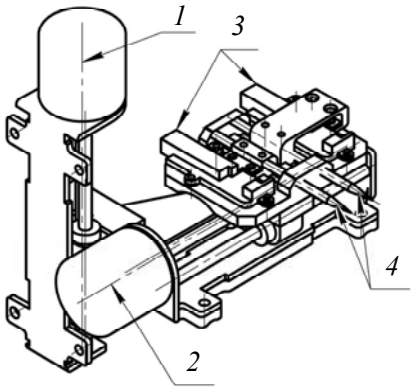

Fig. 1. 3D model of the measuring part of the setup: 1 – Y-axis motor, 2 – X-axis motor, 3 – Z-axis motors, 4 – copper electrodes

The electrodes measure the thermo-EMF of nanoscale conducting films at four points, which allows the measurement accuracy to be increased and the thermo-EMF distribution profile over the film surface to be presented.

Figure 2 shows the external view of the setup.

Figure 3 presents the block diagram of the setup.

Thermo-EMF registration is performed by a 16-bit analog-to-digital converter with an input impedance of 100 MΩ; the measurement results are processed using an 8-bit microcontroller of the AVR family, ATmega328p.

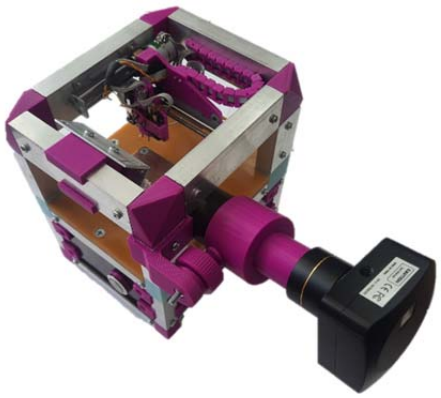

Fig. 2. External view of the setup for measuring the thermo-EMF of nanoscale conducting films

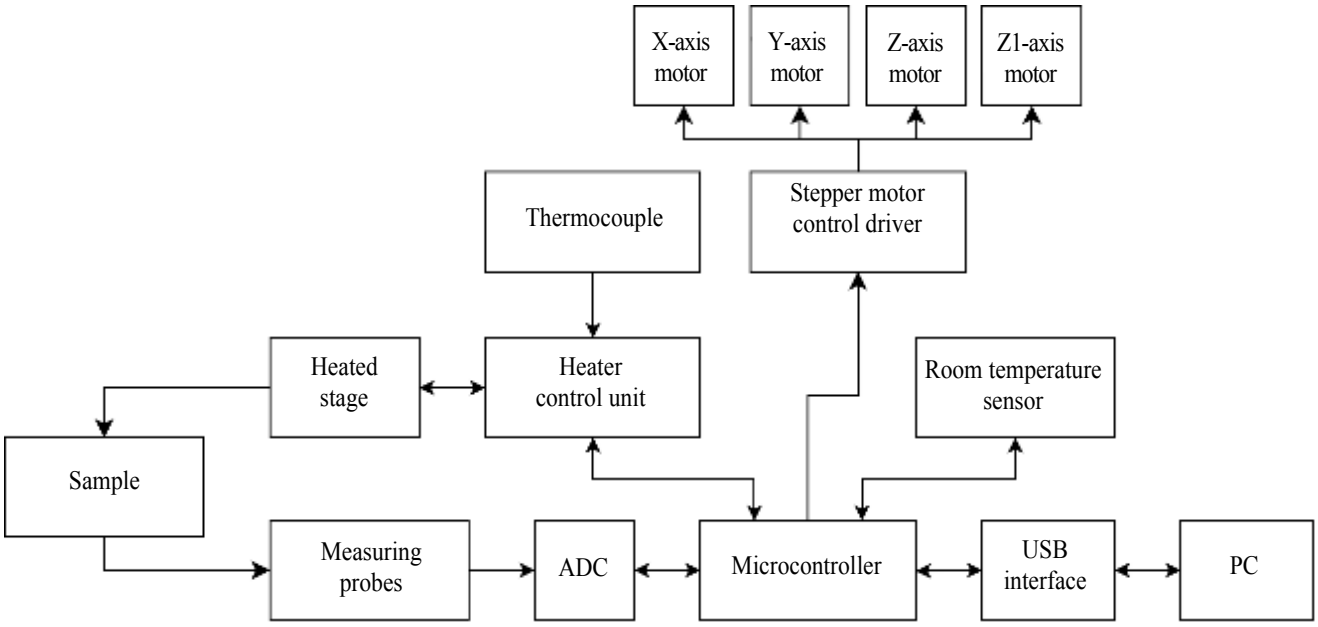

Fig. 3. Block diagram of the setup for measuring the thermo-EMF of nanoscale conducting films

Find the results

The samples studied in this work were obtained by magnetron sputtering from a compact indium-tin target (90 % In, 10 % Sn) in an argon gas environment with the addition of oxygen. The oxygen pressure amounted to 10–30 % of the total pressure in the chamber [9, 10]. Silicon and borosilicate glass were used as substrates. Sputtering lasted for 20 minutes onto a substrate preheated to 350 °C, followed by vacuum annealing at 400 °C for 30 minutes. The resistivity of the obtained films was measured by the 4-probe method, and the temperature dependence of electrical conductivity was recorded, which is presented in Figure 4.

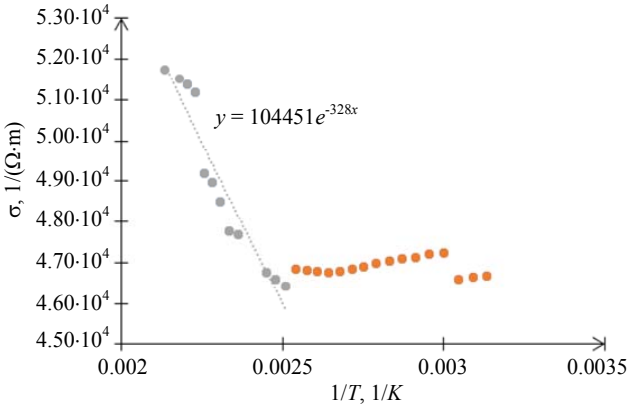

Fig. 4. Temperature dependence of the electrical conductivity of the ITO film

Two regions are clearly discernible on the dependence curve. In the region up to 110 °C, a metallic type of electrical conductivity is noticeable, which indicates that at these temperatures the ITO film is a degenerate semiconductor and electrical conductivity occurs via delocalized states near the Fermi level. The higher-temperature region corresponds to hopping conductivity via oxygen vacancies, which are F-centers. Each such center facilitates the capture of one or two electrons depending on the vacancy charge. In this region, the temperature dependence of electrical conductivity has an activation character with an electrical conductivity activation energy on the order of 0.05 eV, which is characteristic of the hopping mechanism of electron transfer.

Next, using the experimental setup, the temperature dependence of the thermo-EMF was recorded and the temperature dependence of the Seebeck coefficient of the tungsten-ITO contact was plotted, which is presented in Figure 5.

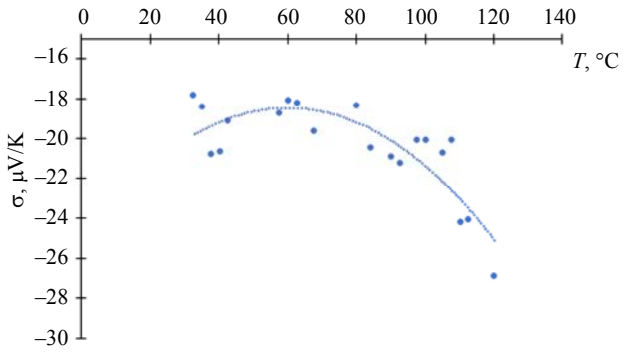

Fig. 5. Temperature dependence of the Seebeck coefficient of the tungsten–ITO contact

By approximating the experimental values, it can be noted that in the temperature range of 30–110 °C the Seebeck coefficient values are small and practically independent of temperature, which is characteristic of metals, since the main contribution to the generation of thermo-EMF in metals is made by electrons, whose concentration is constant and whose energy is close to the Fermi level located in the conduction band. At these temperatures, changes in the distribution of electrons over energy levels are insignificant, and consequently, the potential difference between two metals in contact under a temperature gradient is insignificant and constant.

The electron concentration in the ITO film at room temperature, calculated using Formula (4), amounted to 2.6×10^{20} cm^{-3}. The Fermi level is then located above the bottom of the conduction band by 0.42 eV.

At temperatures above 110 °C, the Seebeck coefficient begins to increase in absolute value and becomes temperature-dependent, which is characteristic of non-degenerate semiconductors. In such semiconductors, the concentration of free charge carriers depends on temperature.

A correlation can be noted between the temperature dependences of the Seebeck coefficient and the electrical conductivity, which at temperatures up to 110 °C has a metallic character, and at higher temperatures a semiconducting character, caused by the presence of oxygen vacancies [4].

To calculate the electron concentration in the hopping conductivity region, it should be taken into account that oxygen vacancies in ITO films are formed both during their sputtering and during vacuum annealing. The films studied in this work were subjected to vacuum annealing for 30 minutes at 400 °C. Knowing these technological parameters, the concentration of oxygen vacancies in the film can be calculated using the following formula:

$$N_v = N_0 \cdot \exp\left(-\frac{E_{\text{Eb}}}{kT}\right), \qquad (7)$$

where N_0 is the concentration of oxygen atoms at the stoichiometric composition of the film material, and E_{Eb} is the binding energy of an oxygen atom with an In_2O_3 molecule, equal to the energy of oxygen vacancy formation.

It should be understood that electrical conductivity may not occur via all oxygen

vacancies, since not all oxygen vacancies are located in a suitable energy band to participate in charge transfer. For this reason, oxygen vacancies located far from the Fermi level cannot effectively participate in charge transfer.

As a rule, electrons with energies on the order of kT near the Fermi level participate in hopping conductivity. The concentration of such electrons is equal to:

$$n = kT \cdot N\left(E_F\right), \tag{8}$$

where $N\left(E_F\right)$ is the density of states at the Fermi level, which is calculated using the following formula:

$$N\left(E_F\right) = \frac{3}{4 \cdot \pi \cdot R^3 \cdot E_a}, \tag{9}$$

where R is the electron hopping length.

The calculated concentration of oxygen vacancies in the film amounted to 9.93×10^{21} cm^{-3}, and the concentration of electrons participating in hopping conductivity amounted to 1.8×10^{21} cm^{-3}. Despite the high concentration of these electrons, the increase in electrical conductivity after vacuum annealing of the films does not exceed 20 %, which is associated with their low mobility under the hopping mechanism – in this case, not exceeding 0.3 cm²/(V·s) [3, 10].

Conclusion

In this work, the thermoelectric and electrical properties of nanoscale ITO films obtained by magnetron sputtering were investigated, and it was established that their thermo-EMF at temperatures from 20 to 110 °C increases monotonically (in absolute value) and has a magnitude from –15 to –25 μV/K. A correlation was established between the temperature dependence of electrical conductivity and the temperature dependence of the thermo-EMF. It has been demonstrated that the developed prototype of the measuring setup shows promise for its use in scientific research.

The work was carried out under grant No. FEWM-2024-0004 Theoretical Studies and Experimental Development of an Optical Attachment for Analyzing the Parameters of Components of High-Speed Fiber-Optic Transmission Systems for Analog and Digital Signals."

REFERENCES

1. Zeng S., Baillargeat D., Ho H. P., and Yong K. T., Chemical Society Reviews **43**, 3426–3452 (2014).
2. Erickson D., Mandal S., and Yang A., J. Microfluid Nanofluid **4**, 33 (2008).
3. Mott N. Electronic processes in non-crystalline substances. Moscow: Mir, 1974.
4. Parfenov O. E. and Shklyaruk F. A., Physics and technology of semiconductors **41** (9), 1041–1045 (2007).
5. Sytchkova A., Zola D., Bailey L. R., Mackenzie B., Proudfoot G., Tian M., and Ulyashin A., Materials Science and Engineering **178** (9), 586–592 (2012).
6. Zhongkai Zhang, Zhaojun Liu, Jiaming Lei, Luntao Chen, Le Li, Na Zhao, Xudong Fang, Yong Ruan, Bian Tian, and Libo Zhao, iScience **26**, 1–19 (2023).
7. Rafiq Mulla and Charles W. Dunnill, Carbon Trends **4**, 1–9 (2021).
8. Xiaohui Zhao, Hongmin Wang, Zixiang Zhao, and Wanli Zhang, Nanoscale Research Letters **4** (2017).
9. Zhidik Y., Ivanova A., Smirnov S., Zhidik K., Ynusov I., and Trojn P., Coatings **12** (120, 1868 (2022).
10. Smirnov S. V., Minin O. N., Chistoedova A. A., and Petryuk A. E., Nanotechnologies: development, application – XXI century **11** (1), 14–18 (2019).

About authors

Terekhova Alexandra Sergeyevna, Tomsk State University of Control Systems and Radioelectronics (634050, Russia, Tomsk, Lenina Ave., 40). E-mail: tas18102004@mail.ru

Zelensky Leonid Andreyevich, Tomsk State University of Control Systems and Radioelectronics (634050, Russia, Tomsk, Lenina Ave., 40). E-mail: leonidzelenskij22@mail.com

Smirnov Serafim Vsevolodovich, Doctor of Technical Sciences, Professor, Tomsk State University of Control Systems and Radioelectronics (634050, Russia, Tomsk, Lenina Ave., 40). E-mail: serafim.smirnov@mail.ru SPIN code: 8284-0404, AuthorID: 438551

ELECTRON, ION AND LASER BEAMS

UDC 537.533.79: 621.384.6.01 PACS: 41.85.-p
EDN: IQIUXS

Pulse current compression of high-current relativistic electron beam on a virtual cathode

A. E. Donets*, V. I. Rogozhin, A. A. Ravaev, A. B. Buleyko, O. T. Loza, D. A. Adamyants, and I. R. Muftakhov

Joint Stock Company State Research Center of the Russian Federation Troitsk Institute for Innovation and Fusion Research (JSC SRC RF TRINITI), Moscow, Troitsk, 108840 Russia
** E-mail: donets@triniti.ru*

Received 18.11.2025: revised 30.11.2025; accepted 27.04.2026

The limit transport current of a high-current relativistic electron beam (REB) in a strong magnetic field in a coaxial liner with the potential of the central electrode equal to the potential of the cathode forming the REB has been analytically calculated. The conditions for the virtual cathode formation in a coaxial diode with magnetic insulation and a double cathode, in which the diameter of the inner conductor changes along its length, have been found. The phenomenon of temporal compression of the REB current has been experimentally demonstrated. The current amplitude increase by 1.5–2 times with pulse duration decrease from 2.5 ns to ~1 ns is due to the appearance of the virtual cathode. The directions for further study of the REB dynamics, its temporal and energy parameters contributing to the virtual cathode formation and, as a result, temporal compression of the REB, have been outlined.

Keywords: Explosive emission cathode, high-current electron beam, virtual cathode, nanosecond pulse, magnetic field.

DOI: 10.51368/2949-561X-2026-2-61-68

For citation: Donets A. E., Rogozhin V. I., Ravaev A. A., Buleyko A. B., Loza O. T., Adamyants D. A., and Muftakhov I. R., Applied Physics, No. 2, 61–68 (2026).

Introduction

For the generation of high-current relativistic electron beams (REBs) in direct-action accelerators at electron energies on the order of 10^6 eV and beam currents of $\sim 10^3$ A and above, explosive-emission cathodes are used. The current magnitude in this case is limited not by the emission capability of the cathode, but by the REB potential, which is determined by the shape of the electrodes and the electron flow. At a fixed initial electron energy, as the current increases, the electron flow potential rises and, under certain conditions, reaches that of the cathode voltage, while the electron velocity drops practically to zero. Such an electron cloud with the cathode potential and zero particle velocity has been termed a virtual cathode (VC).

Virtual cathodes, which are of great interest for ion acceleration, the generation of strong electromagnetic waves (in particular, the vircator – a microwave radiation generator based on a VC), and for a number of other applications, have been studied for many years in various configurations. For many purposes, REBs are formed in a strong magnetic field as a tubular-shaped electron flow; therefore, a significant part of VC research has been conducted specifically in this configuration. In the present work, we will also restrict ourselves to the axially symmetric case of forming a tubular REB and transporting it in a strong solenoidal magnetic field within a circular cross-section vacuum chamber with conducting walls – in a hollow metal pipe.

It was shown in [1] that, for a fixed radius r_b of a thin-walled tubular REB propagating along

the axis of the chamber with radius R, its current cannot exceed the limiting value I_{lim}:

$$I_{lim} = I_0 \frac{\left(\Gamma^{2/3} - 1\right)^{3/2}}{2\ln\frac{R}{r_b}}. \quad (1)$$

Here, the current is $I_0 = \frac{4\pi\varepsilon_0 mc^3}{e} \approx 17$ kA, and the factor Γ is determined by the potential difference U in the accelerator diode:

$$\Gamma = 1 + \frac{eU}{mc^2}, \quad (2)$$

where the value is $\frac{mc^2}{e} \approx 511$ kV.

The relativistic factor $\gamma = \left(1 - \frac{v^2}{c^2}\right)^{-1/2}$, which depends on the electron velocity v, for the current I_{lim} is equal to $\gamma = \Gamma^{1/3}$. The potential of the electron flow is determined by the difference between the total and kinetic energies:

$$\Phi = (\Gamma - \gamma)\frac{mc^2}{e} = U - (\gamma - 1)\frac{mc^2}{e}. \quad (3)$$

When attempting to inject a current exceeding the I_{lim} value, the electron beam transitions to an unstable "compressed" state [2], in which $\gamma < \Gamma^{1/3}$, and which rapidly collapses toward $\gamma \to 1$, turning into a VC. The current flowing from the VC remains equal to I_{lim} on average [3], but becomes non-stationary, and two main frequency groups prevail in the oscillation spectrum. The so-called "transit-time" frequencies are determined by the motion time of electrons trapped between two equipotential regions: the accelerator cathode and the VC. The second frequency group is the Langmuir frequencies of the electron cloud $\omega_{Le} = \sqrt{\frac{4\pi ne^2}{m}}$ with a concentration n that varies in time and space.

The most common method of creating a VC using a REB propagating in a strong magnetic field is its injection into a chamber with a variable radius. It is seen from formula (1) that as the chamber diameter R increases, the limiting current I_{lim} decreases. Therefore, the REB is injected into a chamber with a small radius, where its current does not exceed the limiting value. Further, as the REB propagates in a uniform magnetic field, the chamber expands so that the I_{lim} value falls below the current value, and then a VC is formed in the transition region from the smaller to the larger radius.

The described configuration is not the only possible one for creating a VC. Our preliminary calculations [4] showed that, with a certain electrode configuration and a REB pulse duration of up to several nanoseconds, the forming VC first impedes the passage of electrons through it, and then rapidly releases the accumulated charge. Thereby, the REB current pulse duration decreases, while its amplitude increases.

The purpose of the present work was the experimental demonstration of the phenomenon of current increase in a nanosecond relativistic electron beam upon shortening of the REB pulse duration the REB pulse shortening, which can be called electron beam current pulse compression or, more concisely, temporal compression of an electron beam. In the present work, experimental studies of the transport of an REB formed in a strong magnetic field through a VC region in the previously proposed configuration [4] were carried out, as well as analytical estimations of the conditions required for this. The configuration [4] makes it easy to experimentally implement the variation of the limiting transport current I_{lim} while keeping the parameters of the REB formed at the cathode constant, as well as keeping the VC location in the same liner cross-section while maintaining the configuration of its outer walls unchanged.

Analytical calculations

The method of REB formation and virtual cathode generation is shown in Fig. 1. The entire structure possesses axial symmetry and is placed in a strong uniform magnetic field. In Fig. 1, a cathode **2** with infinite emission capability at its emitting edge with radius r_c is placed inside a cylindrical chamber **1** with radius R. A cylinder **4** with radius r is fixed on the cathode by means of

a holder rod **3** with radius r_s. Pipe **1**, which acts as the anode, is grounded, while cathode **2**, rod **3**, and cylinder **4** constitute a single conducting structure held at the same negative potential U. In a strong uniform magnetic field, the radius of the tubular relativistic electron beam **5** coincides with the radius of the cathode edge: $r_b = r_c$.

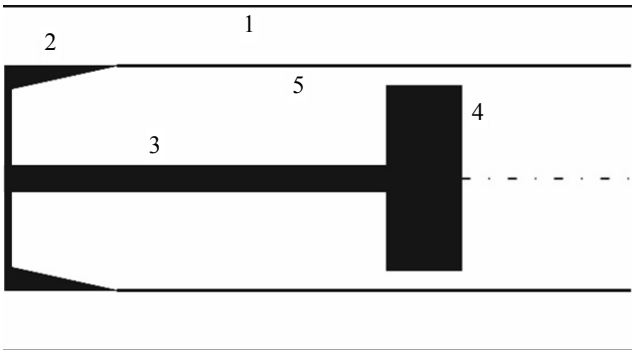

Fig. 1. Diode with a virtual cathode: 1 – cylindrical chamber (anode), 2 – explosive-emission cathode edge, 3 – rod, 4 – cylinder, 5 – REB trajectory

In [5], the current of an external cathode formed in a magnetically insulated coaxial diode with a double cathode, which corresponds to electrodes **2** and **3** in Fig. 1, was calculated. The current from cathode **2** in the presence of the long conducting rod **3**, which is equipotential to it, but without taking cylinder **4** into account, is equal to

$$I_N = \frac{I_0}{2\ln\dfrac{R}{r_s}}\left[\frac{\Gamma-\gamma}{1-\varkappa}-\frac{\gamma-1}{\varkappa}\right]\sqrt{1-\frac{1}{\gamma^2}}, \qquad (4)$$

where

$$\gamma = \frac{3}{2}\sqrt{1+\frac{8}{9}\varkappa\left(\Gamma-1\right)}-\frac{1}{2},\ 0<\varkappa=\frac{\ln\left(\dfrac{r_b}{r_s}\right)}{\ln\left(\dfrac{R}{r_s}\right)}<1,$$

the index N indicates the first author of paper [5], and the beam potential is determined by formula (3).

For $r_s \to 0$ ($\varkappa \to 1$), the electron beam current according to formula (4) and the factor determining the potential Φ according to formula (3) take the corresponding values of the Fedosov current I_F [6] and the factor γ of a tubular REB formed by a magnetically insulated coaxial diode in a hollow circular waveguide:

$$I_F = I_0\frac{1}{2\ln\dfrac{R}{r_b}}\frac{\left(\Gamma-\gamma\right)\sqrt{\gamma^2-1}}{\gamma},$$

where $\gamma = \sqrt{\dfrac{1}{4}+2\Gamma}-\dfrac{1}{2}.$ (5)

Cylinder **4** in Fig. 1 with radius $r > r_s$ and potential U can cause the formation of a virtual cathode. The current of the tubular REB behind the virtual cathode equals the limiting transport current of the electron beam [3]. Therefore, a virtual cathode is formed if the current from the cathode in the presence of the rod with radius r_s exceeds the limiting transport current of the electron beam in the region where cylinder **4** is located. The calculation of the current of an infinitely thin tubular REB in an infinitely strong magnetic field under the specified conditions presents no difficulties under the assumption that the longitudinal dimensions of the system substantially exceed the transverse ones.

By repeating procedures similar to those performed in [1, 5, 6], one can obtain the dependence of the limiting transport current of a tubular thin-walled electron beam in the coaxial configuration shown in Fig. 1 on the parameter γ:

$$I_{coax} = \frac{I_0}{2}\left[\frac{\Gamma-\gamma}{\ln\dfrac{R}{r_b}}-\frac{\gamma-1}{\ln\dfrac{r_b}{r}}\right]\sqrt{1-\frac{1}{\gamma^2}}. \qquad (6)$$

The maximum of this function, i.e., the limiting transport current, is reached at:

$$\frac{dI_{coax}}{d\gamma}=0, \qquad \gamma = \sqrt[3]{\frac{\ln\dfrac{R}{r_b}+\Gamma\ln\dfrac{r_b}{r}}{\ln\dfrac{R}{r_b}+\ln\dfrac{r_b}{r}}}. \qquad (7)$$

For $r \to 0$, the value $\gamma \to \Gamma^{1/3}$ and the current according to formula (1) takes the value of the limiting current [1] for the transport of a tubular REB in a hollow circular waveguide: I_{lim}.

Fig. 2 shows two current dependences on the radii. Note that the abscissa axis represents

the radius values of different electrodes, but such a comparison helps to better understand the features of the process. The upper curve 1 according to formulas (6, 7) shows the dependence of the limiting REB transport current I_{coax} on the cylinder radius r. In this case, $R = 24$ mm, $r_b = 10$ mm, and the parameter $\Gamma = 1.5$. At $r = 0$, i.e., in the absence of the cylinder, the current equals the limiting current [1] in a hollow waveguide: $I_{coax} = I_{lim}$.

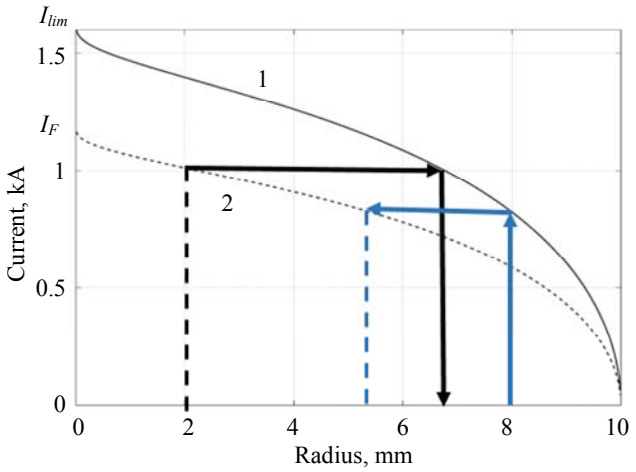

Fig. 2. Dependences of: 1 – the limiting REB transport current in the coaxial configuration $I_{coax}(r)$ according to formula (6); 2 – the current of the external electrode of the double cathode $I_N(r_s)$ according to formula (4)

The lower curve 2 according to formula (4) illustrates the dependence of the Nechaev current I_N [5] from the external electrode of the double cathode **2** in Fig. 1 on the rod radius r_s. As applied to Fig. 1, this is the current from cathode **2** as a function of the radius r_s of rod **3** in the absence of cylinder **4**. At $r_s = 0$, i.e., in the absence of the internal electrode (rod), this current (5) coincides with the Fedosov current [6] from the cathode in a hollow waveguide: $I_N(r_s = 0) = I_F$. In both dependences $I_{coax}(r)$ and $I_N(r_s)$, as the radii of the internal electrodes r and r_s approach the radii of the cathode and the electron beam ($r_c = r_b$), the currents of the formed beam I_N and the transported beam I_{coax} tend to zero.

The dependence $I_{coax}(r)$ according to formula (6) does not involve the parameter r_s in any way, and conversely, $I_N(r_s)$ according to formula (4) lacks any dependence of the current on the radius r, which makes it possible to compare these dependences in Fig. 2, as well as to optimize the experiment on VC generation. By fixing the cylinder dimension r, one can select the required rod radius r_s, and vice versa. Examples of such a selection are shown in Fig. 2 by arrows. Curve 2 shows that for a rod radius $r_s = 2$ mm, the cathode current equals 1 kA. The horizontal line from it to the right and the vertical line from its intersection point with curve 1 indicate the cylinder radius $r \approx 6.7$ mm, above which the transported current becomes smaller than the cathode current. In other words, a VC is formed at $r_s = 2$ mm and $r > 6.7$ mm, i.e., at a distance from the REB to the cylinder $r_b - r < 3.3$ mm. In the opposite case, the vertical line from $r = 8$ mm to the intersection with curve 1 shows that a cylinder of such a radius does not transmit a current exceeding 0.8 kA. The horizontal line from this point to curve 2 determines the maximum rod radius for VC formation at fixed cylinder dimensions: at $r = 8$ mm, i.e., at $r_b - r = 2$ mm, the rod radius $r_s < 5.3$ mm.

The described scheme of VC generation provides simpler methods of varying the experimental parameters (changing the rod and the cylinder) compared to the traditional REB configuration in a tube with expanding walls. However, as will be shown below, the VC parameters can be optimized altogether within a single series of experiments without replacing parts or even changing their positions.

Experimental Setup

Fig. 3 shows the scheme of the axially symmetric experimental setup used in this work for VC investigation.

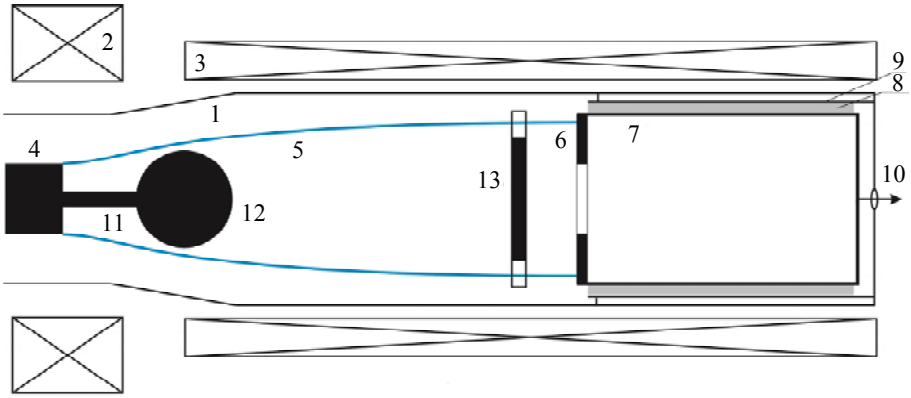

Fig. 3. Experimental setup for VC investigation: 1 – vacuum chamber; 2 – coil; 3 – solenoid; 4 – cathode; 5 – REB; 6 – collector; 7 – inner metal cylinder of the current meter; 8 – dielectric; 9 – outer metal cylinder of the current meter; 10 – coaxial vacuum-tight connector; 11 – threaded rod; 12 – spherical electrode; 13 – slit diaphragm

Vacuum chamber **1** with a vacuum pumping system ensures a pressure not exceeding 0.1 Pa. Coil **2** and solenoid **3** with independent power supplies create a quasi-stationary magnetic field: the coil – up to 3.5 T, the solenoid — up to 1 T. A graphite explosive-emission cathode **4** with a diameter of 20 mm is located in the region of the strong magnetic field of coil **2**, and chamber **1** near the cathode has a diameter of 48 mm. A negative potential pulse is applied to the cathode from the Radan-303 high-voltage pulse generator [7] with an additional pulse-forming unit. After the pulse former, the generator pulses have a rise time of 0.3 ns and a plateau of 2 ns with an amplitude of 250 kV at a total FWHM duration of 2.5 ns (see Fig. 4). A calibrated capacitive voltage divider (not shown in the figure), which measures the pulsed voltage, is located in the oil-filled transmitting coaxial line with an impedance of 50 Ω at a distance of about ~60 cm from the cathode.

The cylindrical electron beam **5** propagates along the magnetic field lines from the region of coil **2** into the region of solenoid **3**, gradually increasing in diameter from 20 to ~ 34 mm. The characteristic length of the magnetic field variation region is about ~ 15 cm. Vacuum chamber **1** also has a variable diameter that varies in accordance with the magnetic field lines and equals 60 mm in the region of solenoid **3**. The electron beam **5** is collected on collector **6**, which is simultaneously a part of the picosecond-duration high-current REB current meter described below [8].

A rod **11** with a diameter of 5 mm with a thread is fixed on cathode **4**, onto which electrode **12** is screwed. This electrode has the shape of a sphere with a diameter of 30 mm, in contrast to its functionally analogous cylindrical electrode 4 in Fig. 1. The spherical shape of the electrode, which is at the cathode potential, and its polished surface prevent electron emission from it during the pulse, which has a duration of about ~ 2 ns.

It is clear from Fig. 2 that the onset of a VC in our case is actually determined by the distance from the REB trajectory to the sphere **12**, which is equipotential to the cathode. Coarse adjustment of this distance in the experiment is performed by changing the position of the sphere along rod **11**. With the change in the REB trajectory radius during the transition from the strong magnetic field region to the weak one by 7 mm over a characteristic length of 15 cm, such adjustment can be easily performed with an accuracy of at least 1 mm. In addition, the independent power supply systems of coil **2** and solenoid **3** provide additional possibilities for controlling the REB radius. If the position of sphere **12** and the beam current in solenoid **3** are fixed, then weakening the field of coil **2**, i.e., the magnetic field at the cathode, leads to a decrease in the distance from the electron trajectories to the sphere. Moreover, this distance optimization can be carried out at different positions of the sphere (and the associated position of the VC) along the axis, thereby substantially changing the distance from it to the cathode.

The choice of the current measurement method was determined by the short REB pulse

duration, which makes the use of traditional shunts and Rogowski coils problematic. The current meter [8] shown on the right in Fig. 3 represents a long coaxial waveguide and consists of inner **7** and outer **9** metal cylinders separated by dielectric **8**. The outer electrode of the waveguide is grounded to chamber **1**, the inner electrode on the REB side is connected to collector **6**, and on the opposite side – to the central conductor of the coaxial vacuum-tight SMA-type connector 10. The REB current with an amplitude of ~ 1 kA induces a voltage of about 1.5 kV on the measuring line with an input impedance of ~ 1.5 Ω. To transmit the signal through SMA coaxial connectors and attenuators without the risk of breakdown, the measured current and the resulting voltage on the line were reduced in advance by more than an order of magnitude, for which purpose beam **5** passed onto collector 6 through a slit diaphragm **13**. The 40 cm length of the current meter made it possible to reliably record signals before the appearance of re-reflections in the line after ~ 4 ns. The registration of cathode potential signals and currents was carried out using an oscilloscope with a sampling rate of 50 GSa/s and an operating frequency bandwidth of 10 GHz.

Experiment results and discussion

Fig. 4 shows the oscillograms of the cathode potential (*a*) and the currents: (*b*) – in the classical scheme without a VC, and (*c*) – upon VC formation. Preliminary precise synchronization of the potential and current pulses was hampered not only by the large distance of ~ 1 m between the sensors. Along this path, the signal velocity was determined by the propagation velocities of the wave in the transmitting coaxial line of the accelerator and the measuring coaxial line, as well as by the velocity of the electrons of the formed beam, which gradually changed from zero to the maximum value. However, the current signals – Fig. 4 (*b*) and (*c*) – were obtained from the same sensor; therefore, their mutual delay can be judged with confidence.

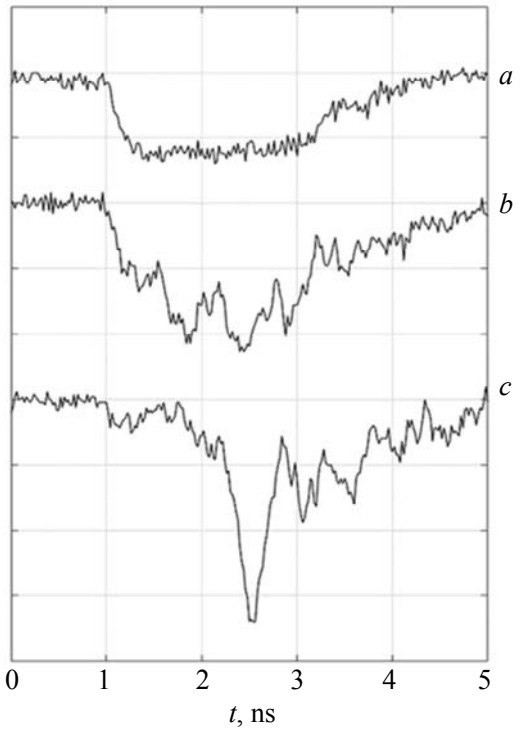

Fig. 4. Oscillograms: a – cathode potential; b – REB current in the absence of the rod and the spherical electrode on the cathode; c – REB current after the VC

In the absence of the rod and the spherical electrode on the cathode, i.e., when forming a REB in a classical magnetically insulated coaxial diode [6], the voltage (Fig. 4*a*) and current (Fig. 4*b*) pulses coincide in duration and are equal to approximately 2 ns from the beginning of the leading edge to the beginning of the pulse fall. The similarity of the shape of these pulses after 2 ns – a sharp drop to about half the amplitude over ~ 0.4 ns and a smoother decay thereafter – suggests that the voltage and current pulses begin simultaneously with an accuracy of up to 0.2 ns.

The current oscillations with a period of 0.6 ns, visible on the oscillograms, can have at least two possible origins. First, they may be a consequence of the explosive-emission cathode operation at the initial stage of electron emission development from emerging and disappearing cathode micro-flares. Second, the cause may be the use of a slit diaphragm that limits the total REB current. It is known that a convective diocotron instability develops in magnetized tubular REBs [9], which at the nonlinear stage of development manifests itself in the form of beam filamentation. The number of filaments (threads) is greater, the thinner the current tube. Under the conditions of the described experiment, with a

REB wall thickness of up to 1 mm after traversing a distance of ~ 0.5 m from the cathode to the current meter, the number of filaments amounted to several tens: the beam imprint on the target clearly demonstrated current inhomogeneities with a spacing of ~ 1 mm along the perimeter. Several such current filaments passed through the slit diaphragm. In crossed fields – the axial magnetic field and the radial electrostatic field of the electron flow space charge — the current filaments have the form of spirals whose twist angle depends linearly on the REB current. With small fluctuations of the cathode current, a different number of current filaments passes through the slit diaphragm; therefore, the recorded current after the diaphragm varies much more strongly. This pattern was previously observed by the authors of [8]; therefore, to register the total REB current without slit diaphragms, more complex methods of attenuating the electrical signal from the current meter directly in the vacuum chamber were employed.

When the propagation trajectory of beam electrons **5** and electrode **12** approached to a certain distance, a VC was formed. The signal from the current sensor (Fig. 4*c*) began with a delay of more than 1 ns compared to the case without a VC, but its amplitude exceeded that shown in Fig. 4*b* without a VC by a factor of ~ 1.5. Approximately the same effect was observed in calculations using the CST code [4] in a diode configuration with a uniform magnetic field, as in Fig. 1, but with a spherical electrode, as in Fig. 3.

The following sequence of events can be assumed. Initially, the potential of the spherical electrode delays the passage of REB electrons for a certain time, and space charge accumulation occurs in the space between the cathode and the sphere. When the current is cut off, the cathode potential increases to higher values than in the absence of electrode 12, because the signal from the accelerator transmitting line with an impedance of 45 Ω encounters a load with a higher impedance. To a certain extent, this simple explanation agrees with the results of numerical simulation of the process under consideration [4].

Conclusion

The purpose of the present work was the experimental demonstration of the phenomenon of current increase in a nanosecond relativistic electron beam upon shortening of the REB pulse duration, which can be called the temporal compression of an electron beam. The design allows for the experimental implementation of the variation of the limiting transport current I_{lim} while keeping the parameters of the REB formed at the cathode constant. This feature distinguishes the work from previous ones – the VC can be either formed or not formed in the same liner cross-section while maintaining the configuration of its outer walls and the solenoids that create the magnetic field. In addition, methods for both coarse and fine adjustment to select the VC formation parameters have been proposed. Coarse adjustment was carried out by moving the central electrode by means of a threaded connection with the vacuum system vented, whereas fine adjustment was achieved by slightly changing the magnetic field profile by varying the current in one of the two solenoids during a single series of experiments.

The substantiation and consistent explanation of the physical processes occurring in the diode with the described electrode configuration require additional experiments and three-dimensional numerical simulation. In particular, first, it is necessary to obtain more reliable experimental results in which the influence of the slit diaphragm (and the diocotron instability of the REB) on the measurements of the total beam current will be excluded. Second, numerical simulation of the processes in the diode is required using parameters that not only reproduce the conditions of the conducted experiment, but also exploit the advantages of a numerical experiment, which is not limited by the framework of direct experimental realization.

The work was carried out within the framework of state contract No. Н.4к.241.09.25.1066 dated May 20, 2025.

REFERENCES

1. Bogdankevich L. S. and Rukhadze A. A., Sov. Phys. Usp. **14**, 163–179 (1971).
2. Ignatov A. M. and Tarakanov V. P., Phys. Plasmas. **1** (3), 741–744 (1994).
3. Belomyttsev S. Ya., Grishkov A. A., Kitsanov S. A., Korovin S. D., Polevin S. D., and Ryzhov V. V., Technical Physics Letters **31** (1), 55–57 (2005). https://doi.org/10.1134/1.1859500
4. Donets A. E., Rogozhin V. I., and Ravaev A. A. Vserossijskaya molodezhnaya konferenciya po upravlyaemomu termoyadernomu sintezu, plazmenny`m texnologiyam i vy`sokotexnologichnoj medicine VMKT-2925. Moscow, g. Troiczk, 2025. pp. 161–162. ISBN 978-5-521-24626-7. https://www.triniti.ru/upload/pdf/vmkt_theses_web.pdf
5. Nechaev V. I., Soluyanov E. I., and Fuks M. I., Pis`ma v ZhTF **5** (2), 113–117 (1979).
6. Fedosov A. I., Litvinov E. A., Belomytsev S. Y. et al., Soviet Physics Journal **20**, 1367–1368 (1977). https://doi.org/10.1007/BF00898924
7. Shpak V. G., Shunailov S. A., Yalandin M. I., and Dyadkov A. N., Instruments and Experimental Techniques **36** (1), 106–111 (1993).
8. Mesyats G. A., Yalandin M. I., Reutova A. G., Sharypov K. A., Shpak V. G., and Shunailov S. A., Plasma Physics Reports **38** (1), 29–45 (2012).
9. Eremeev A. I., Kabanov V. S., Strelkov P. S., Fedotov A. V., and Shkvarunets A. G., Sov. J. Plasma Phys. **14** (8), 958–964 (1988).

About authors

Donets Aleksandra Evgenyevna, Junior Researcher, Joint Stock Company State Research Center of the Russian Federation Troitsk Institute for Innovation and Fusion Research (JSC SRC RF TRINITI) (108840, Moscow, Troitsk, Pushkovykh st., bldg. 12). E-mail: donets@trininti.ru SPIN code: 7676-9276

Rogozhin Vasily Ilyich, Junior Researcher, Joint Stock Company State Research Center of the Russian Federation Troitsk Institute for Innovation and Fusion Research (JSC SRC RF TRINITI) (108840, Moscow, Troitsk, Pushkovykh st., bldg. 12). E-mail: rogozhin@triniti.ru

Ravaev Alexander Alexandrovich, Leading Researcher, Joint Stock Company State Research Center of the Russian Federation Troitsk Institute for Innovation and Fusion Research (JSC SRC RF TRINITI) (108840, Moscow, Troitsk, Pushkovykh st., bldg. 12). E-mail: aaravaev@triniti.ru SPIN code: 9461-0294, AuthorID: 123902

Buleyko Alla Borisovna, Head of the Laboratory, Joint Stock Company State Research Center of the Russian Federation Troitsk Institute for Innovation and Fusion Research (JSC SRC RF TRINITI) (108840, Moscow, Troitsk, Pushkovykh st., no. 12). E-mail: buleyko@triniti.ru SPIN code: 5470-6692, AuthorID: 1092022

Loza Oleg Timofeevich, Scientific consultant, Joint Stock Company State Research Center of the Russian Federation Troitsk Institute for Innovation and Fusion Research (JSC SRC RF TRINITI) (108840, Moscow, Troitsk, Pushkovykh st., no. 12). E-mail: OTLoza@triniti.ru SPIN code: 3536-2581, AuthorID: 25260

Adamyants Diana Anuarovna, Intern, Joint Stock Company State Research Center of the Russian Federation Troitsk Institute for Innovation and Fusion Research (JSC SRC RF TRINITI) (108840, Moscow, Troitsk, Pushkovykh st., 12). E-mail: E-mail: daadamyants@triniti.ru

Muftakhov Ilyas Rashidovich, Intern, Joint Stock Company State Research Center of the Russian Federation Troitsk Institute for Innovation and Fusion Research (JSC SRC RF TRINITI) (108840, Moscow, Troitsk, Pushkovykh st., 12). E-mail: irmuftakhov@triniti.ru

PHYSICAL EQUIPMENT AND ITS ELEMENTS

UDC 681.7.068 PACS: 42.30.Va, 42.79.Bh, 07.05.Mh
EDN: FWZBSG

Image autofocusing in optoelectronic systems based on a fuzzy PID controller

A. A. Berillo

RD&P Center ORION, JSC, Moscow, 111538 Russia
E-mail: berillo.andrey@yandex.ru

Received 16.03.2026; revised 3.04.2026; accepted 27.04.2026

The problem of improving the accuracy and speed of automatic focusing systems in optoelectronic systems (OES) is considered. It is shown that the application of classical PID controllers is limited by nonlinearities of drives and non-stationarity of observed scenes. A structure of an adaptive system using fuzzy logic for dynamic tuning of the PID controller coefficients is proposed. The choice of the Tenengrad contrast measure function and the Orange Pi 6 Plus hardware platform for real-time algorithm implementation is substantiated. The expected performance indicators of the proposed approach are given.

Keywords: autofocus, optoelectronic system, fuzzy controller, PID controller, focus measure function, image processing, Orange Pi, adaptive control.

DOI: 10.51368/2949-561X-2026-2-69-71

For citation: Berillo A. A., Applied Physics, No. 2, 69–71 (2026).

Introduction

Modern optoelectronic systems (OES) impose stringent requirements on image quality, the key condition for which is precise focusing (autofocus). The task is complicated by the nonlinearities of the lens drive (backlash, dry friction) and the variability of the characteristics of the observed scenes (illumination, contrast), which makes the control object non-stationary. A promising direction for operation under such conditions is the application of adaptive control methods [1, 2].

Traditional PID controllers, tuned to a single operating point, lose efficiency when the dynamics of the object change. Extremum-seeking controllers are prone to oscillations near the focus point and have low response speed. An alternative effective approach is the application of fuzzy PID controllers [3], which allow real-time adaptation of control parameters, ensuring robustness to nonlinearities and external disturbances. The effectiveness of such an approach for autofocus tasks has been confirmed experimentally [2].

The aim of this work is the theoretical substantiation and development of the structure of an autofocus system structure based on a fuzzy PID controller using a modern element base for video data processing.

Problem statement and selection of the focus evaluation function

The autofocus process can be represented as the task of finding the lens position x^* at which the sharpness evaluation function $F(x)$ is maximal: $x^* = \arg\max F(x)$. The control error $e(t)$ is indirectly determined through the deviation from this maximum. The dynamics of the drive, for example, a DC motor, can be described by the transfer function $W(s) = \dfrac{k}{s(T_m s + 1)}$, where k is the gain coefficient, and T_m is the electromechanical time constant. This model does not account for nonlinearities such as backlash, which requires the application of more complex control algorithms [2, 4].

The performance quality of the system directly depends on the choice of $F(x)$. A comparative analysis of methods showed that for real-time tasks, the most applicable is the **Tenengrad gradient method**, which provides a good compromise between accuracy and computational complexity. The fundamental justification of this method is presented in [5]. Its effectiveness for images close in nature to those obtained in OESs has been confirmed in later studies [6]. The algorithm consists in convolving the image $I(x,y)$ with Sobel operators to obtain the horizontal $G(x)$ and vertical $G(y)$ gradient components, to calculate the gradient magnitude $S(x,y)=\sqrt{G_x\left(x,y\right)^2+G_y\left(x,y\right)^2}$ and to summing it over the analysis region $M\times N$:

$$F_{Tenengrad}=\sum_{x=1}^{M}\sum_{y=1}^{N}S\left(x,y\right).$$

Development of a fuzzy PID controller

The proposed system (Fig. 1) is built according to a two-level scheme. The lower level is a classical PID controller, generating a control signal $u(t)$ to the drive. The upper level is a fuzzy corrector that dynamically changes the PID controller coefficients: ΔK_p, ΔK_i, ΔK_d. The resulting coefficients are determined as: $K_p=K_{p0}+\Delta K_p$ etc., where K_{p0} are the baseline values. The theoretical foundations of fuzzy control are set out in [3], and the successful application of a similar structure for autofocus tasks has been demonstrated in [2, 4].

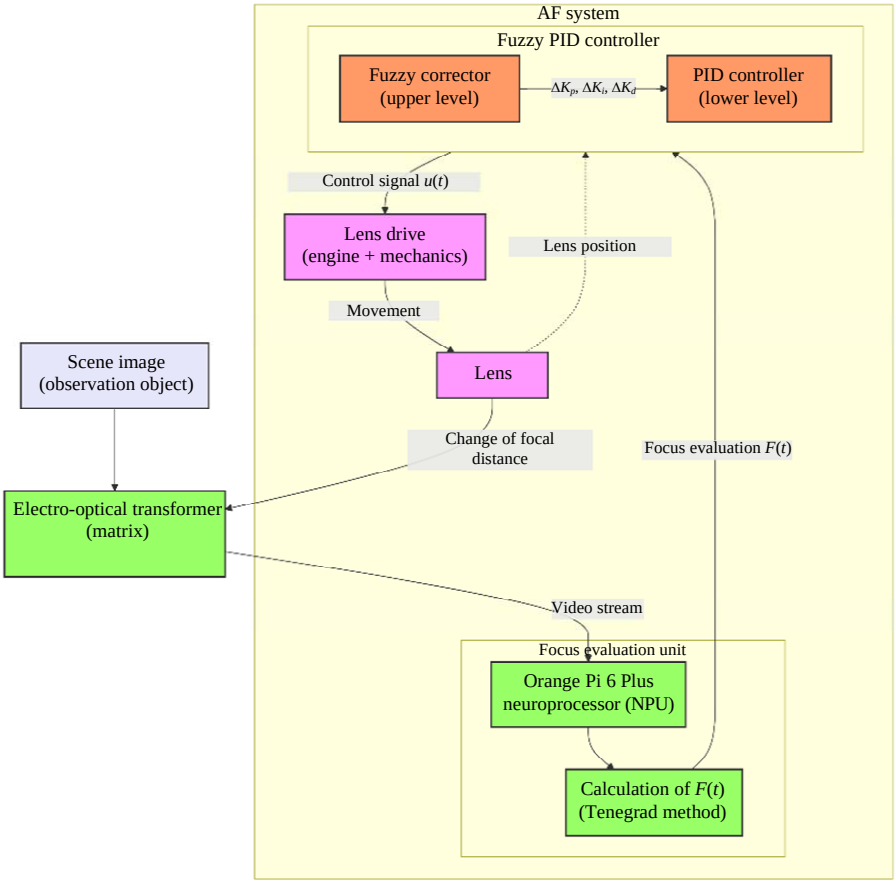

Fig. 1. Structural diagram of the autofocus system with a fuzzy PID controller

The input crisp variables – error e and its rate of change $\dot{e}$ – are transformed into linguistic variables with seven terms: NB (negative big), NM, NS, Z, PS, PM, and PB (positive big). Triangular-shaped membership functions are chosen. The fuzzy rule base (table) was developed on the basis of empirical knowledge about tuning PID controllers, adapted for the autofocus task. To obtain crisp values of the correction coefficients, the centroid method is used. A similar approach to forming the rule base was used in [2].

Table

Fragment of the rule base for ΔKp correction

e / $\dot{e}$	**NB**	**NM**	**NS**	**Z**	**PS**	**PM**	**PB**
NB	PB	PB	PM	PM	PS	Z	Z
Z	PM	PM	PS	Z	NS	NM	NM
PB	Z	Z	NS	NM	NM	NB	NB

Hardware implementation and expected results

To implement the system, it is proposed to use an Orange Pi 6 Plus single-board computer with a CIX CD8180 SoC. A key advantage is the built-in neural processing unit (NPU) with a performance of 28.8×10^{12} operations per second, enabling hardware acceleration of the Tenengrad function computation (convolution with Sobel kernels). The following load distribution is planned: NPU – preprocessing and computation of $F(t)$; CPU (high-performance cores) – operation of the fuzzy controller.

Given that the work is at the stage of theoretical development, quantitative performance indicators are estimated as projected. It is planned to conduct simulation modeling in MATLAB/Simulink for a drive model with a "backlash"-type nonlinearity. It is expected that, compared with a classical PID controller, the fuzzy PID controller will allow overshoot to be reduced by 20–30 % and settling time to be reduced by 25–35 % (Fig. 2), which is consistent with the results obtained in [2, 4].

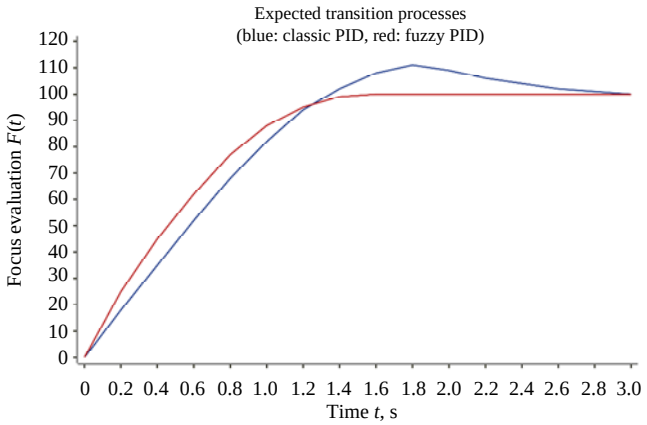

Fig. 2. Expected transient processes for classical and fuzzy PID controllers.

Conclusion

In this work, an analysis of the autofocus problem was carried out, and the feasibility of applying adaptive control methods was substantiated [1, 2]. A contrast evaluation function (Tenengrad method) was selected, based on fundamental [5] and modern [6] studies, and the structure of a fuzzy PID controller was developed [2, 3]. The choice of the Orange Pi 6 Plus hardware platform was justified; its use will enable real-time implementation of the algorithms. Projected performance indicators were formulated. Further research will be directed toward simulation modeling and experimental validation on a developed test bench.

REFERENCES

1. Pegat A. Fuzzy Modeling and Control. Moscow: Laboratoriya znaniy Publ., 2020 [in Russian].
2. Zhou J., Xue L., Li Y., Cao L., and Chen C., Sensors **22** (22), 8657 (2022).
3. Ali R., Peng Y., Ali A., Ali H., Akhter N., Ahmed J., and Jalil A., IEEE Access **8**, 130014–130026 (2020).
4. Wang D. J., Ding X., Zhang T., and Kuang H., Optics & Laser Technology **45**, 190–197 (2013).
5. Pech-Pacheco J. L., Cristobal G., Chamorro-Martinez J., and Fernandez-Valdivia J. Proceedings of the 15th International Conference on Pattern Recognition, Barcelona, **3**, 2000, pp. 314–317.
6. Ma C., Zhang M., Dai Z., Zhang Q., Ma J., Niu X., and Yan Y., PLoS ONE **20** (11), e0336810 (2025).

About the author

Berillo Andrey Anatolyevich, Lead Software Engineer, Master, RD&P Center ORION, JSC (111538, Russia, Moscow, Kosinskaya st., 9). E-mail: berillo.andrey@yandex.ru

PHYSICAL EQUIPMENT AND ITS ELEMENTS

UDC 534.134, 534.143, 534.442.1, 534.6.08, 621.3.019.1 PACS: 43.30.-k, 43.30.+m
EDN: AXGRNO

Characteristics of a compact hydroacoustic transducer with high power density in transmission and reception modes

A. K. Britenkov[1,2*], B. N. Bogolyubov[1], R. V. Travin[1], V. A. Farfel[1], I. I. Leonov[1], and D. A. Kosteev[1]

[1] *A. V. Gaponov-Grekhov Institute of Applied Physics of the Russian Academy of Sciences, Nizhny Novgorod, 603951 Russia*
[*] *E-mail: britenkov@ipfran.ru*
[2] *National Research Lobachevsky State University of Nizhny Novgorod, Nizhny Novgorod, 603022 Russia*

Received 5.11.2025; revised 27.11.2025; accepted 27.04.2026

The use of reversible compact low-frequency transducers in hydroacoustic repeaters designed for use at distances of up to several tens of kilometers allows reducing the mass and dimensions of such devices. The paper presents the results of electroacoustic measurements of a compact transducer with a complex shape of an all-metal case both in the emission and reception modes of hydroacoustic signals. The acoustic power emitted by such a transducer exceeds 38 W for quasi-harmonic signals and reaches 12 W for complex pulse signals. The voltage amplitude at the output of the transducer operating in the reception mode is at a level of about 1500 mV in the operating frequency band and 200–400 mV outside its operating band, which is several times higher than the indicators of existing reversible hydrophones at similar values of the received sound pressure.

Keywords: hydroacoustics, underwater sonar communication, piezoelectric transducer, hydroacoustic emitter, hydroacoustic repeater, reversible hydrophone, electroacoustics.

DOI: 10.51368/2949-561X-2026-2-72-78

For citation: Britenkov A. K., Bogolyubov B. N., Travin R. V., Farfel V. A., Leonov I. I., and Kosteev D. A., Applied Physics, No. 2, 72–78 (2026).

Introduction

A specific feature of hydroacoustic measurements in marine conditions is their dependence on positioning errors of the measuring system components, which, along with the effect of environmental parameter fluctuations on sound propagation, reduces measurement accuracy. The use of transponders (responder beacons) that emit the same or a predetermined signal after registration reduces positioning errors and the dependence on environmental parameter variations. Responder beacons have become widespread in navigation [1], including that of unmanned vessels [2], the control of autonomous underwater vehicles, and telemetry data transmission, as well as for marking underwater equipment to facilitate search operations [3], and in other hydroacoustic applications.

Such devices are subject to mutually exclusive requirements of increasing autonomous operation duration and emitted signal energy. To meet these requirements, the device must incorporate a radiator with high efficiency along with an energy-efficient driving circuit. Therefore, the development of radiators with small wave dimensions and high specific power [4] is one of the urgent tasks of engineering support for hydroacoustic measurements.

Compact 3D LF radiator – a high specific power transducer

Compact low-frequency transducers are typically defined as those satisfying the relation $\lambda > 2\pi D$ (λ is the sound wavelength, and D is the characteristic dimension of the radiator), given

that $D < 0.5$ m and the fundamental resonance frequency does not exceed 2 kHz. Given the small wave dimensions of the radiating surface, compact low-frequency transducers usually exhibit low efficiency and a narrow operating frequency bandwidth. To achieve higher efficiency and increase the sound pressure level generated by the radiator, technical solutions are employed that are primarily aimed at increasing the vibration amplitude and the radiating surface area. A successful example of a compromise between the radiated acoustic power, efficiency, operating frequency bandwidth, and fundamental resonance frequency is the 3D LF radiator – a flextensional hydroacoustic transducer with an all-metal body of complex geometry [5].

The compact 3D LF radiator described in [6], measuring 96×130 (diameter×length) mm and weighing less than 1.5 kg with a structural volume of 735 cm^3, has its fundamental resonance in the range up to 2 kHz and a relative operating frequency bandwidth of 25–30 %, which allows it to radiate up to 40 W of acoustic power using CW and LFM signals (more than 2.0 kPa of effective sound pressure value reduced to 1 m). For complex signals, the acoustic power radiated by such a radiator reaches 12 W. Fig. 1a shows the radiated acoustic power for pulsed phase-modulated signals with a crest factor up to 1.6, a duty cycle close to 100%, and an effective value of the driving voltage applied to the radiator of about 700 V (Fig. 1*b*).

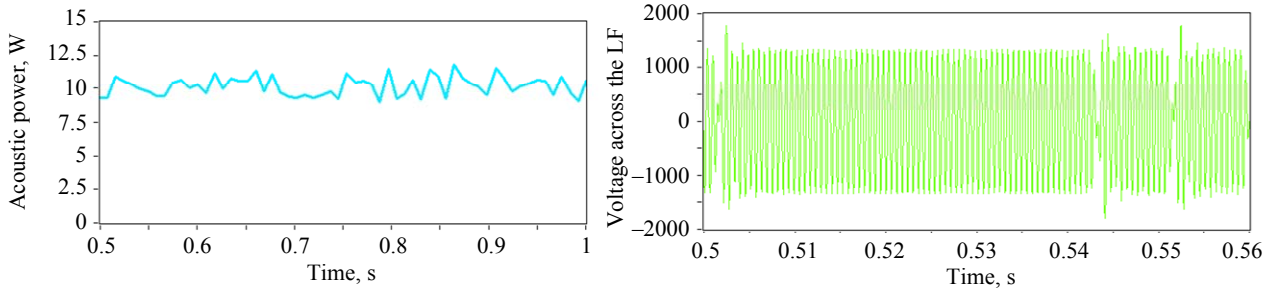

a) *b)*

Fig. 1. Radiated acoustic power and driving voltage of the 3D LF radiator for complex pulsed signals with a small off-period

The acoustic radiation power for complex signals is lower than that for quasi-continuous quasi-harmonic signals, because during rapid changes in the signal phase, the 3D LF radiator, being an oscillatory system with a high Q-factor, requires some time to reach the maximum amplitude mode. Fig. 1b shows that the driving voltage amplitude at certain moments during carrier frequency phase changes reaches 1800 V. The difference in the levels of radiated acoustic power for continuous and complex signals directly depends on the information transmission rate [7], since the number of transmitted alphabet elements determines the number of switchings of the transducer's oscillatory system per unit time, and accordingly, the total duration of radiation at maximum power.

The radiated acoustic power of commercially available responder beacons and hydroacoustic modems amounts to 10–20 W for distances ranging from several thousand meters to several tens of kilometers. For example, the maximum acoustic power level of the Evo Logics S2CR 12/24 hydroacoustic modem is 57 W in the frequency band of 13–24 kHz, while for information transmission at a rate of up to 9.2 kbit/s over a distance of 6 km, the device radiates up to 15 W of acoustic power. A similar operating range of the transponder can be ensured when using the compact 3D LF radiator in the frequency range up to 2 kHz, taking into account the lower attenuation over such distances with an increase in the wavelength of the emitted sound [8]. Taking into account the experimental data (see Fig. 1), the average level of acoustic power radiated by such a 3D LF radiator for complex signals can be increased to 15–20 W, which, combined with high efficiency (over 60 %), allows the use of such transducers in autonomous systems [9].

Measuring the characteristics of the compact 3D LF radiator as a receiver

The voltage sensitivity of the transducer operating as a receiver is determined by

comparing it with the sensitivity of a reference radiator reduced to 1 m:

$$\xi = \frac{U_{\text{h}} L_{\text{h}}}{\gamma_{\text{h}}(f) U_{\text{LFR}}^{\text{h}}}, \qquad (1)$$

where L_{h} is the distance from the measuring hydrophone to the reference LF radiator, U_{h} is the voltage at the measuring hydrophone, $\gamma_{\text{h}}(f)$ is the sensitivity of the measuring hydrophone, $U_{\text{LFR}}^{\text{h}}$ is the excitation signal voltage at the reference radiator with a similar dependence recorded using the 3D LF radiator operating as a receiver. Normalizing this dependence by the ratio of distances from the reference LF radiator to the receivers and the sensitivity of the measuring hydrophone yields the frequency dependence of the transducer's receiving voltage sensitivity:

$$\gamma_{\text{3DLFR}} = \gamma_{\text{h}}(f) \frac{U_{\text{3DLFR}} L_{\text{3DLFR}}}{U_{\text{h}} L_{\text{h}}} \text{ [V/Pa]}, \qquad (2)$$

where $L_{\text{3D LFR}}$ is the distance from the receiver (3D LF radiator) to the reference radiator, $U_{\text{3D LFR}}$ is the voltage at the 3D LF radiator. It should be noted that, in order to reduce the influence of hardware errors during measurements, identical amplitudes of excitation voltages are set at the reference radiator when recording the sound pressure by the reference measuring hydrophone and the 3D LF radiator, which eliminates the need to account for the ratio of these quantities on the right-hand side of formula (2). According to some studies [10, 11], the reciprocity coefficient, equal to the ratio of the transducer's transmitting voltage sensitivity to its receiving voltage sensitivity, does not depend on the design but is determined by the radiation and reception conditions and the properties of the acoustic medium. However, in practice, in-situ measurements are necessary to estimate the reciprocity coefficient precisely because of the transducer's structural design and the conditions of radiation and reception.

The determination of the transmitting and receiving electroacoustic characteristics was carried out in open water at a depth range ranging from 5 to 70 m. The transducer, mounted on an acoustic pole 3 m long, 1 m from the reference hydrophone and 2 m from the reference radiator, was submerged using a rig structurally connecting the reference radiator, the 3D LF radiator, and the hydrophone (Fig. 2).

Fig. 2. Rig for measuring the electroacoustic characteristics of the 3D LF radiator

For measurements and data recording, NI 9215 ADC and NI 9263 DAC modules were used together with a National Instruments NI cRIO-9031 chassis, a G61N hydrophone, and a Probe Master 4241A differential voltage probe. A Bicon opposed-piston type LF radiator (acoustic monopole) [4] was employed as the reference. In accordance with the measurement procedure [12], the emitted signal, current, voltage at the reference radiator, as well as the voltage from the hydrophone and the 3D LF radiator were synchronously recorded using a data acquisition system based on LabView 2015.

The sensitivity characteristics of the compact 3D LF radiator as a receiver of hydroacoustic signals exceed those of the hydrophone. The frequency dependence of the voltage acquired from the 3D LF radiator operating in the receiving mode practically coincides with its transmitting voltage sensitivity characteristic [6]. The slight difference in the frequency maxima of the characteristics obtained for reception and transmission is related to the difference in the types of resonance phenomena in the oscillatory system of the 3D LF radiator transducer and does not exceed the range of instrumental errors of electroacoustic measurements. Fig. 3 shows the frequency dependences of the output voltage of the 3D LF radiator in the receiving mode on the wave dimension kr, where k is the wave number, r is the equivalent radius of the radiator, defined as the radius of a sphere with a volume equal to the water volume displaced by the 3D LF radiator structure.

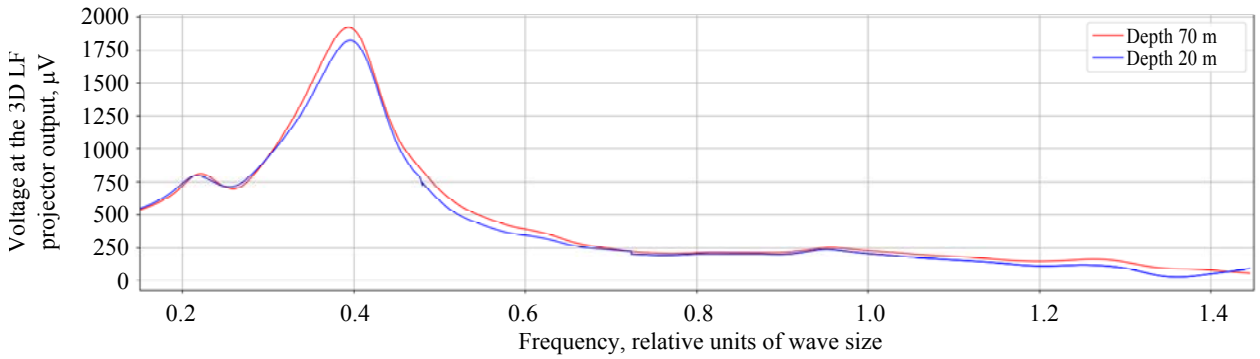

Fig. 3. Output voltage of the compact 3D LF radiator placed at a depth of 20 and 70 m when used as a receiving hydrophone

Due to the special geometry of the 3D LF radiator body, its sensitivity curves as a receiver remain virtually unchanged in a depth range down to 100 m. Considering the characteristics of the compact 3D LF radiator when operating on reception, which are comparable with the parameters of commercially produced hydrophones (e.g., G61N, G3301, ZET 311, etc.), the application of such a transducer as part of a transponder [13] is fully justified.

Using the compact 3D LF radiator as part of a transponder

The high mechanical transformation coefficient of the compact 3D LF radiator and the developed surface of its body provide, outside its operating frequency band, a sensitivity 5–10 times greater compared to reversible hydrophones. For most reversible hydrophones, for example, ZETLAB ZET 351 (manufactured by Electronic Technologies and Metrological Systems), the maximum acoustic radiation power is less than 1.0 W (receiving sensitivity 160 μV/Pa, operating frequency band from 3 to 2500 Hz). Thus, the 3D LF radiator as a hydroacoustic receiver will enable a half-duplex operating mode of the transponder, where the emission of a response signal at a different frequency is performed with a delay relative to the incoming transmission. Combining the receiver and radiator in a single device reduces the dimensions of the hydroacoustic beacon operating in such a mode and using the 3D LF radiator in the frequency band outside its fundamental resonance.

For operation in full-duplex mode, due to the high voltage amplitude at the radiator, in order to avoid damage to the receiving path of the transponder, it is necessary to use filters with isolation between bands of about 120 dB. Such a characteristic can be implemented based on an active filter model [14] consisting of several stages on operational amplifiers (Fig. 4).

Due to the limitations of the existing component base in terms of maximum input voltage levels, ensuring the operation of the transponder in full-duplex mode involves replacing the integrated circuits of the first stages of the separation filter with circuits made of discrete components having the required dielectric strength. Thus, taking into account the parameters of existing high-voltage transistors (such as 2SC5411, IHW30N160R5XKSA1, or 2T839A/IM), the implementation of a filter with isolation between bands of at least 120 dB appears technically feasible.

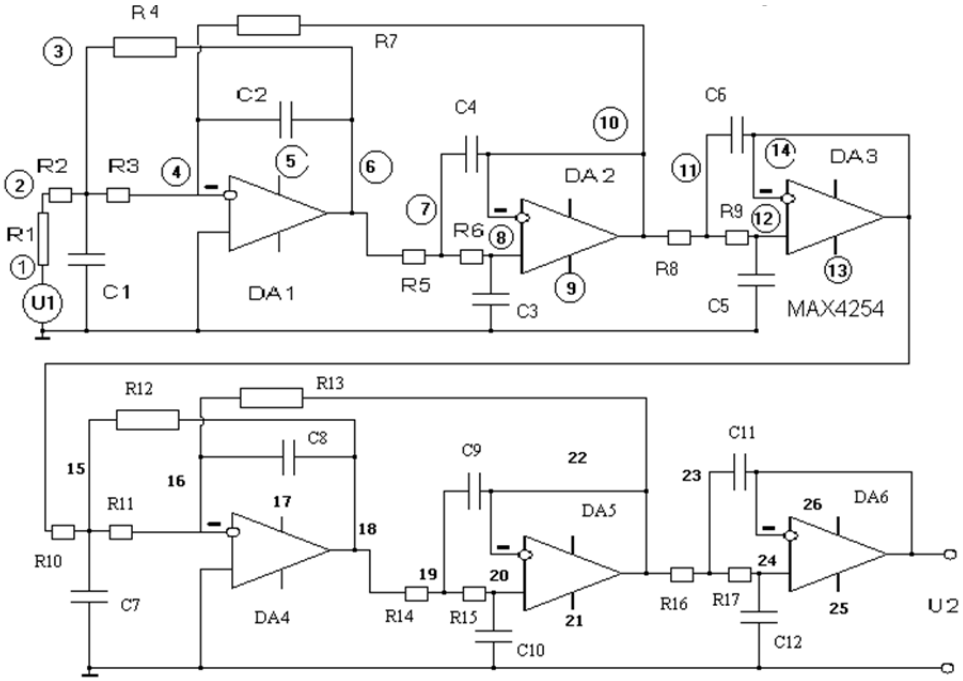

Fig. 4. Circuit of an active 12th-order polynomial filter with a roll-off slope of more than 120 dB per octave

Influence of depth on radiator characteristics

The electroacoustic characteristics of a radiator depend on many factors, in particular, on the external hydrostatic pressure. Due to the special geometry of the 3D LF radiator body, the stiffness of its oscillatory system remains practically unchanged in the depth range of 10–70 m. However, with an increase in immersion depth, the radiator body undergoes some deformation under the influence of external hydrostatic pressure. As the shell deflection decreases, the Q-factor of the transducer drops slightly and its resonance frequency f_0 decreases, causing an increase in the frequency response bandwidth from 16 % (of f_0) at a depth of 10 m to 20–24 % at 70 m. The drift of f_0 is less than 2.5 % per 100 m (Fig. 5), which is lower than the values for traditional flextensional radiators of similar size with a force-driven design [15].

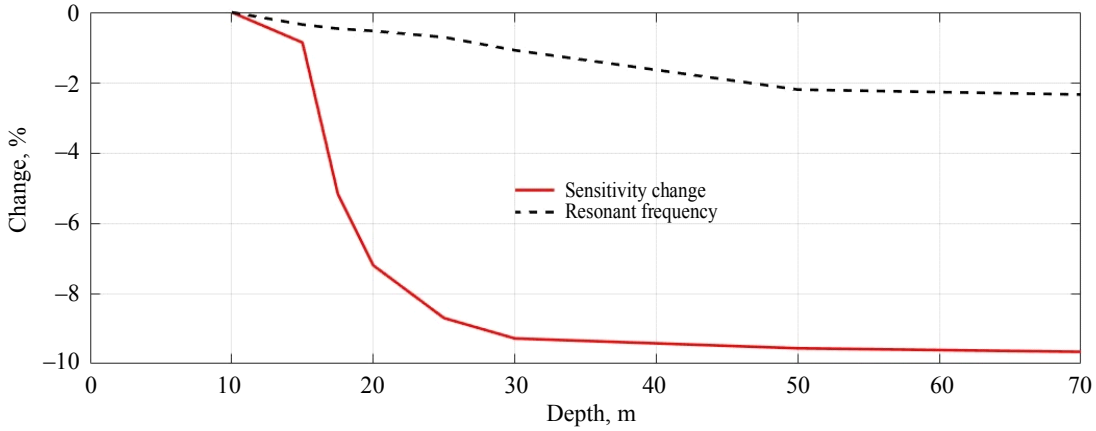

Fig. 5. Dependence of the electroacoustic parameters of the compact 3D LF radiator on depth

In known transducers [16], the fundamental resonance frequency usually increases with depth due to the aggregate increase in the stiffness of the transducer's oscillatory system. Thus, the resonance frequency of a compact LF flextensional radiator of traditional design with a hydrostatic pressure compensator at 200 m can rise by 10 % or more from f_p at a depth of 30–50 m, increasing with depth by more than 3.5 % per 100 m [17].

The decrease in the 3D LF radiator voltage sensitivity caused by the increase in radiation

resistance with increasing depth amounts to about 5 % per 100 m (Fig. 5), which does not exceed the measurement error. The relative error of voltage measurement in accordance with GOST R 8.736-2011 and the errors of the ADC $\delta_{ADC} = \pm 1$ %, hydrophone – $\delta_h = \pm 12$ %, differential high-voltage probe – $\delta_U = \pm 2$ %, and measurement of the distance to the radiator – $\delta_L = \pm 0.5$ %, is determined by the formula

$$\delta_{\gamma_{3D\ LFR}} = \sqrt{\sum_i \delta_i^2}\ , \qquad (3)$$

where δ_i are the relative measurement errors, including the errors of excitation voltage measurement (errors of the differential probe δ_U and ADC δ_{ADC}), errors of voltage measurement at the hydrophone (δ_h and δ_{ADC}), distance from the LF radiator to the hydrophone L, etc. Thus, the resulting sensitivity measurement error is within ± 14–15 % (reception) and ± 10–12 % (transmission).

As can be seen from Fig. 5, the influence of external hydrostatic pressure in the depth range from 20 to 50 m on the radiator parameters is insignificant; however, in some applications it must be taken into account due to the requirements for the developed sound pressure level given the limited energy resources of the driving system.

Conclusion

The 3D LF radiator possesses sufficient dielectric strength, allowing it to radiate complex signals with a crest factor of 1.6 or more at a level of 10–15 W. The unevenness of the frequency response of the compact 3D LF radiator operating in the receiving mode in the low-frequency range does not play a significant role for an acoustic transponder due to the possibility of frequency correction in the preamplifier, and the reception of signals of a certain type is not associated with requirements for a high degree of linearity of the receiving path's frequency response. The combination of compact dimensions with electroacoustic characteristics, in particular, high specific radiated acoustic power and a wide frequency band for receiving acoustic signals, allows the use of such 3D LF radiators in various hydroacoustic applications: modems, underwater acoustic communication systems, and responder beacons, including those operating in full-duplex mode.

The authors express their gratitude to V. N. Bugrov, Associate Professor of the Department of Radio Engineering of the Radiophysical Faculty at the Lobachevsky State University of Nizhny Novgorod; A. I. Chernova, Leading Programmer of the Department of Automation of Scientific Research; V. A. Perfilov, Head of the Laboratory of Experimental Electronics; M. B. Salin, Head of the Laboratory of Vibroacoustics; and P. I. Korotin, Head of the Center for Hydroacoustics, for their attention to this work, assistance in organizing and conducting the research, as well as their comments during the discussion of the results.

The work was carried out within the framework of the state assignment of the Institute of Applied Physics of the Russian Academy of Sciences "Propagation of Acoustic Waves in the Marine Environment and the Upper Layer of the Earth's Crust" (project FFUF-2024-0041).

REFERENCES

1. Bogdanovich M. L., Borodin M. A., Kovalenko Yu. A., and Khametov R. K., Hydroacoustics, No. 44 (4), 37–44 (2020) [in Russian].
2. Zaitsev A. I., Karetnikov V. V., and Sikarev A. A., Marine Radioelectronics, No. 3 (61), 6–9 (2017) [in Russian].
3. Karalyun V. Yu. Underwater acoustic beacon-responder. Patent for invention No. 2125733 C1 (RF). 1999.
4. Britenkov A. K., Farfel V. A., and Bogolyubov B. N., Applied Physics, No. 3, 72–77 (2021) [in Russian].
5. Britenkov A. K., Bogolyubov B. N., and Smirnov S. A. Longitudinal-bending hydroacoustic transducer. Patent for invention No. 2681268 (RF). 2019.
6. Britenkov A. K., Norkin M. S., Stulenkov A. V., and Travin R. V. Nauchnoe Priborostroenie **33** (4), 28–39 (2023).
7. Shavenko N. K. Fundamentals of information theory and coding. MIIGAiK, 2012 [in Russian].
8. Sheehy M. J. and Halley M. R., J. Acoust. Soc. Amer. **29** (4), 464–469 (1957).
9. Vershinin A. S., Molodoy uchenyy, No. 12 (92), 156–161 (2015) [in Russian].

10. Belousov Yu. I. and Rimsky-Korsakov A. V., Acoustical Physics **21** (2), 161–172 (1975) [in Russian].
11. Kolesnikov A. E. Acoustic measurements. Sudostroenie, 1983 [in Russian].
12. Britenkov A. K., Bogolyubov B. N., and Farfel V. A., Memoirs of the Faculty of Physics. Lomonosov Moscow State University, No. 1, 2010106 (2020) [in Russian].
13. Kosteev D. A., Britenkov A. K., Zemnyukov N. E., Lvov A. V., and Salin M. B. Nauchnoe Priborostroenie **34** (3), 54–63 (2024) [in Russian].
14. Bugrov B. N. and Makarova Yu. M., Sovremennaya elektronika i tekhnologii avtomatizacii, No. 1, 76–81 (2017) [in Russian].
15. Andreev M. Ya., Bogolyubov B. N., Klyushin V. V., and Rubanov I. L., Sensors and systems, No. 12, 51–55 (2010) [in Russian].
16. Evtyutov A. P., Lyalikov A. P., Mitko V. B., Ponomarenko V. I., Prostakov A. L., Sverdlin G. M., Smaryshev M. D., Tarasyuk Yu. F., and Kolesnikov A. E., Handbook of hydroacoustics. Sudostroenie, 1982 [in Russian].
17. Britenkov A. K., Zakharov S. B., Travin R. V., and Farfel V. A. Proc. of the XXXVI session of the Russian Acoustic Society (RAO). Moscow, 2024, pp. 649–655 [in Russian].

About authors

Britenkov Alexander Konstantinovich, Candidate of Physical and Mathematical Sciences, Senior Researcher of the Department of Ocean Acoustics, A. V. Gaponov-Grekhov Institute of Applied Physics of the Russian Academy of Sciences (603950, Russia, Nizhny Novgorod, Ulyanova st., 46); Associate Professor of the Department of Radio Engineering of the Radiophysical Faculty, National Research Lobachevsky State University of Nizhny Novgorod (603022, Russia, Nizhny Novgorod, Gagarina Ave., 23). E-mail: britenkov@ipfran.ru SPIN code: 9041-7248, AuthorID: 117978 WoS ID: AAF-4262-2022, ORCID ID: 0000-0002-0885-2510, Scopus Author ID: 57224398205

Bogolyubov Boris Nikolaevich, Candidate of Technical Sciences, Head of the Laboratory of Applied Hydroacoustics, A. V. Gaponov-Grekhov Institute of Applied Physics of the Russian Academy of Sciences (603950, Russia, Nizhny Novgorod, Ulyanova st., 46). E-mail: boris@ipfran.ru AuthorID: 33193

Travin Roman Vadimovich, Senior Laboratory Researcher of the Laboratory of Applied Hydroacoustics, A. V. Gaponov-Grekhov Institute of Applied Physics of the Russian Academy of Sciences (603950, Russia, Nizhny Novgorod, Ulyanova st., 46). E-mail: r.travin@ipfran.ru SPIN code: 3323-6940, AuthorID: 1199264

Farfel Viktor Alexandrovich, Researcher of the Department of Ocean Acoustics, A. V. Gaponov-Grekhov Institute of Applied Physics of the Russian Academy of Sciences (603950, Russia, Nizhny Novgorod, Ulyanova st., 46). E-mail: vicfar@ipfran.ru AuthorID: 27023

Leonov Igor Ivanovich, Head of the Software Sector, A. V. Gaponov-Grekhov Institute of Applied Physics of the Russian Academy of Sciences (603950, Russia, Nizhny Novgorod, Ulyanova st., 46). E-mail: leonov@ipfran.ru AuthorID: 36697

Kosteev Dmitry Alexeyevich, Junior Researcher of the Laboratory of Vibroacoustics, A. V. Gaponov-Grekhov Institute of Applied Physics of the Russian Academy of Sciences (603950, Russia, Nizhny Novgorod, Ulyanova st., 46). E-mail: dkosteev@ipfran.ru SPIN code: 5368-6339, AuthorID: 1048062

PHYSICAL EQUIPMENT AND ITS ELEMENTS

UDC 577.15, 543.55 PACS: 87.15.R-
EDN: DRVJEJ

Nanotechnology-based sensors for monitoring single molecules of cytochrome P450 BM3

I. D. Shumov[1*], V. S. Ziborov[1,2], A. N. Ableev[1], A. V. Vinogradova[1], O. N. Afonin[1], N. S. Bukharina[1], N. V. Vaulin[3], D. V. Lebedev[3], A. S. Bukatin[3], I. S. Mukhin[3], I. N. Saraeva[4], A. I. Archakov[1], and Yu. D. Ivanov[1,2]

[1] *Institute of Biomedical Chemistry (IBMC), Moscow, 119121 Russia*
[*] *E-mail: shum230988@yandex.ru*
[2] *Joint Institute for High Temperatures of Russian Academy of Sciences (JIHT), Moscow, 125412 Russia*
[3] *Alferov Federal State Budgetary Institution of Higher Education and Science Saint Petersburg National Research Academic University of the Russian Academy of Sciences, St. Petersburg, 194021 Russia*
[4] *P. N. Lebedev Physical Institute of the Russian Academy of Sciences, Moscow, 119991 Russia*

Received 25.12.2025; revised 30.01.2026; accepted 27.04.2026

Nanotechnology-based sensors – an electrical nanopore detector (END) and an atomic force microscope (AFM) – were used to monitor the behaviour of single molecules of cytochrome P450 BM3 enzyme. An END, based on a solid-state nanopore formed in silicon nitride, has been used to monitor the functional activity of P450 BM3 in the reaction of laurate hydroxylation in the presence of NADPH. The functional activity of the studied enzyme has been confirmed by spectrophotometry. Using high-speed AFM, the dynamics of the enzyme molecules on the surface of an inorganic substrate has been visualized. The obtained results clearly demonstrate the potential of using nanotechnology-based detectors to determine the physicochemical properties of enzymes at the single-molecule level, thus gaining a deeper understanding of the fundamental principles of functioning of enzyme systems.

Keywords: cytochrome P450, solid-state nanopore, enzymatic activity, atomic force microscopy, spectrophotometry.

DOI: 10.51368/2949-561X-2026-2-79-84

For citation: Shumov I. D., Ziborov V. S., Ableev A. N., Vinogradova A. V., Afonin O. N., Bukharina N. S., Vaulin N. V., Lebedev D. V., Bukatin A. S., Mukhin I. S., Saraeva I. N., Archakov A. I., and Ivanov Yu. D., Applied Physics, No. 2, 79–84 (2026).

Introduction

Devices with nanoscale sensing elements that are comparable in geometric dimensions to single macromolecules of proteins and nucleic acids are increasingly used in fundamental research. Thus, an atomic force microscope (AFM) enables visualization of single protein macromolecules, including enzymes [1, 2], adsorbed on a solid surface; in turn, electrical nanopore detectors (ENDs) based on solid-state nanopores allow the detection of single enzyme macromolecules [3, 4] and the monitoring of enzymatic processes [5, 6].

Processes in living organisms are catalyzed by enzymes [7]; therefore, understanding any process requires a detailed insight into the mechanism and kinetics of the functioning of the enzymes that regulate it. Currently, macroscopic methods are overwhelmingly used to study the kinetics of enzymatic processes; these methods record an averaged signal coming from an

ensemble of a large number of molecules of the enzyme under study [8]. Analysis of the kinetics of an enzymatic catalytic process at the single-molecule level is more profound and informative, and it is exceptionally useful for understanding processes occurring in living cells [8]. In this regard, the advantages of using ENDs to study enzymatic processes at the single-molecule level are evident. The operating principle of an END consists in recording the ionic current flowing through a nanopore formed in an inorganic membrane that separates two chambers filled with an electrolyte solution [4–6]. The macromolecule of the enzyme under study, when inserted into the nanopore, partially blocks the nanopore, modulating the ionic current flowing thereby. During enzymatic catalysis, changes occur in the structure of the enzyme macromolecule inside the nanopore. These changes, accordingly, causes fluctuations in the ionic current that are then recorded.

It is also worth noting the importance of using AFM to study the physicochemical properties of single enzyme macromolecules – such as their adsorption [2], diffusion properties [9], and enzymatic activity [1]. For instance, the successful use of AFM to determine the activity of single molecules of the enzyme cytochrome P450 BM3 was previously demonstrated [1].

In the present work, we propose the use of an END based on a solid-state nanopore for recording the enzymatic activity of a single molecule of cytochrome P450 BM3 in the hydroxylation reaction of laurate in the presence of NADPH. The solid-state nanopore was formed in a silicon nitride (Si_3N_4, hereinafter referred to as SiN) membrane. The interaction of the enzyme molecule with the surface of the inorganic membrane can affect the process of insertion of this molecule into the nanopore. In this regard, we proposed the use of AFM, in parallel with END and spectrophotometry (hereinafter referred to as SP), to study the behavior of the enzyme under study on the solid surface of an inorganic silicon-containing substrate. Considering the positive experience of the combined use of nanotechnological (atomic force microscopy) and macroscopic (SP) methods for studying the physicochemical properties of enzymes [2], in the present work we propose the application of this approach to cytochrome P450 BM3. The use of the classical SP method [10] allows the functional activity of the enzyme under study to be confirmed [2].

The object of study in our experiments was cytochrome P450 BM3, which belongs to the superfamily of heme-containing monooxygenases (cytochromes P450) and catalyzes the monooxygenation of fatty acids [11]. This enzyme is catalytically self-sufficient [11], meaning that it does not require partner proteins for its functioning. This fact makes cytochrome P450 BM3 a very convenient model object for studying the cytochrome P450 system, which plays a key role in the metabolism of xenobiotics [12].

The aim of the present work is to investigate the dynamics of the behavior of a single cytochrome P450 BM3 molecule on an inorganic substrate both before and during the enzymatic reaction.

Materials and methods

Experimental design. To study the functioning of a single cytochrome P450 BM3 molecule in the reaction of laurate hydroxylation in the presence of the reduced form of nicotinamide adenine dinucleotide phosphate (NADPH), we used an END based on a solid-state nanopore formed in a SiN membrane. In parallel, the functional activity of the enzyme in this reaction was confirmed by the classical SP method [10]. To observe the behavior of the molecules of the enzyme under study on the surface of an inorganic silicon-containing substrate, they were visualized by AFM in liquid.

Reagents and enzyme. Wild-type cytochrome CYP102A1, which was kindly provided by Professor A. W. Munro (University of Manchester, UK), was used in this work; the enzyme was expressed and purified as described by Neeli et al. [10]. The enzyme was also expressed by A. V. Grudo (Institute of Bioorganic Chemistry, NAS of Belarus, Minsk, Republic of Belarus). Sodium laurate (purity ≥ 99 %) and NADPH were purchased from Sigma (USA). Potassium hydroxide (analytical grade) and monobasic sodium phosphate (Na_2HPO_4, analytical grade) were purchased from Reakhim (Moscow). Potassium chloride (KCl) was purchased from Fluka (Germany). Dulbecco's phosphate-buffered saline (DPBS buffer, pH 7.4; 8 mmol/L Na_2HPO_4, 2 mmol/L

KH_2PO_4, 140 mmol/L NaCl, 10 mmol/L KCl) was prepared from a mixture of salts purchased from Pierce (USA). All solutions used in the experiments were prepared using deionized ultrapure water (18.2 MΩ·cm) obtained with a Simplicity UV system (Millipore, France).

Measurements using END. The END comprised a liquid measurement cell with two chambers of 700 μL volume each, separated from each other by a 40-nm-thick SiN membrane. A nanopore with a diameter of ~5 nm was formed in this membrane by electron beam drilling using a JEM-2000F transmission electron microscope (TEM) (JEOL, Japan). Prior to the experiments, both chambers were filled with ultrapure water, which was replaced during the experiments with pure 2 mmol/L DPBS containing 0.6 mol/L KCl. Solutions of cytochrome P450 BM3, sodium laurate, and NADPH were added to one of the chambers to final concentrations of 10 nmol/L, 500 μmol/L, and 200 μmol/L, respectively. After each measurement, the chip was rinsed with ultrapure water. During measurements, a constant voltage of –400 mV was applied between the chamber volumes using Ag/AgCl electrodes. The ionic current was measured in the 1000 Hz frequency range using an amplifier with an internal noise level of ~0.3 pA and recorded with a 16-bit analog-to-digital converter (ADC). The signal was processed using a 1 kHz Butterworth filter. The detector was shielded with a Faraday cage to prevent exposure to external electromagnetic interference.

Measurements using AFM. To investigate the behavior of cytochrome P450 BM3 on the surface of an inorganic substrate, the enzyme was adsorbed onto the surface of a freshly cleaved mica substrate from 2 μL droplet of a 0.25 μmol/L enzyme solution in 10 mmol/L DPBS, pH 7.4, which was incubated on the substrate surface for 3 min and then rinsed off with ultrapure water. The substrate thus prepared was placed into the measurement cell of a RIBM high-speed AFM (manufactured by Prof. T. Ando, Japan) containing 2.5 mmol/L DPBS, pH 7.4. AFM scanning was performed in liquid using NanoWorld probes with a tip radius of less than 10 nm and gold coating (cantilever length 2.5 μm; cantilever resonant frequency in air and in liquid ~1.5 MHz and 0.9 MHz, respectively; spring constant ~0.6 N/m).

Spectrophotometric measurements. The activity of cytochrome P450 BM3 in the laurate hydroxylation reaction was determined by the method developed by Neeli et al. [10] using a model 8453 spectrophotometer (Agilent Deutschland GmbH, FRG). In the experiments, 2 μL of a 50 μmol/L enzyme stock solution was pipetted into a 3-mL quartz cuvette with a 1-cm optical path length containing 500 μmol/L sodium laurate in 50 mmol/L phosphate buffer solution, pH 7.0, and mixed thoroughly. After that, an NADPH solution in the same buffer solution was pipetted into the cuvette to adjust the final NADPH concentration in the cuvette to 200 μmol/L [10], and the recording of the time dependence of the absorbance of the solution in the cuvette was started immediately. Measurements were carried out at a wavelength of 340 nm for 600 s at 25 °C.

Results and Their Discussion

Let us consider the behavior of the enzyme during the reaction it catalyzes. Figure 1 shows typical time (t) dependences of the absorbance of the reaction solution at 340 nm (A_{340}) (left) and the ionic current (I) (right), obtained by monitoring the enzymatic reaction process using the SP method and with the END, respectively.

The $A_{340}(t)$ dependence, which illustrates the kinetics of NADPH consumption during the enzymatic reaction [10] and is shown in Fig. 1, confirms that under the experimental conditions the functional activity of the enzyme under study was quite sufficient for the enzymatic process to occur. Indeed, the activity value of cytochrome P450 BM3 determined from the results of our experiments was 20 s^{-1}. This value correlates well with that obtained by Neeli et al. under the same experimental conditions (50 ± 2 s^{-1} [10]). It should be emphasized that the enzymatic hydroxylation reaction of laurate in the presence of cytochrome P450 BM3 proceeds only in the presence of the electron donor, NADPH [10]. Characteristic peaks with an amplitude of 2–3 pA, indicative of fluctuations of the nanopore-confined enzyme macromolecule during into the nanopore during catalysis [6], are observed on the $I(t)$ curve only when all components of the reaction mixture are present in the measurement cell chamber, and are not observed in the absence of NADPH. It should be noted that characteristic peaks are observed on

the $I(t)$ curve for at least 1200 s, indicating that the molecule retains activity during this period of time.

As noted in the introduction, AFM makes it possible to observe the behavior of biological macromolecules on the surface of solid inorganic substrates [13]. In our AFM experiments, when scanning in liquid (buffer solution with pH 7.4), it was found that the enzyme macromolecules move along the substrate surface, i.e., a surface diffusion process was observed [13]. The AFM images presented in Fig. 2 illustrate this fact.

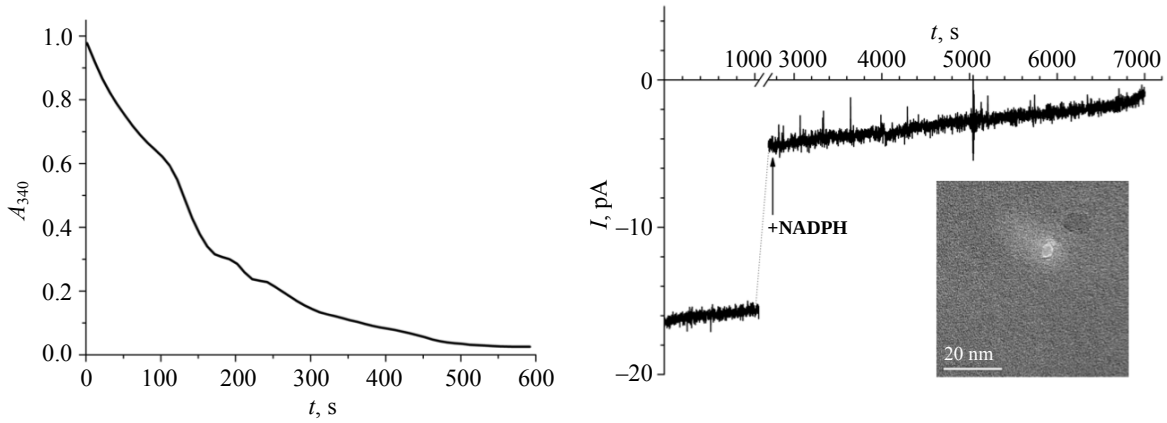

Fig. 1. A_{340}(t) (left) and I(t) (right) dependencies obtained by monitoring the enzymatic reaction process using the SP method and with the END, respectively. The inset shows a TEM image of the END nanopore

Fig. 2. AFM images of cytochrome P450 BM3 macromolecules in liquid, sequentially acquired with a high-speed AFM. Time per frame 1 s. Scan area 200 × 200 nm. Height scale from 0 to 4.5 nm. Frames were acquired at time points 0 s (left), 23 s (center), and 60 s (right)

It should be noted that silanol (Si-OH) groups are exposed on the mica surface [14]. The same groups are present on the surface of the membrane material (Si_3N_4) [15]. Consequently, it can be expected that the behavior of the molecules of the enzyme under study on the surface of the nanopore membrane is similar to their behavior on the mica surface, visualized by AFM in a solution with the same pH value at which the END experiments were conducted. From this, it can be concluded that the process of surface diffusion of the enzyme molecules can influence their transport toward the nanopore and their insertion into it.

Conclusion

Thus, the possibility of using an END to observe the behavior of a single cytochrome P450 BM3 molecule during the laurate hydroxylation reaction catalyzed by this molecule has been experimentally demonstrated. The activity of the enzyme in the reaction under study was confirmed by the SP method. The process of surface diffusion of the enzyme molecules on an inorganic substrate, which can influence their transport toward the nanopore and their insertion into it, was visualized by the AFM method.

The END and AFM measurements were carried out within the framework of the Program for Basic Research in the Russian Federation for a long-term period (2021–2030) (No. 122030100168-2). The SP experiments were carried out with the support of the Ministry of Science and Higher Education of the Russian Federation (State Assignment No. 075-00270-26-00).

REFERENCES

1. Ivanov Y. D., Bukharina N. S., Shumov I. D., Afonin O. N., Tatur V. Y., Grudo A. V., and Archakov A. I., Biosensors **15** (5), 303 (2025).
2. Ivanov Y. D., Pleshakova T. O., Shumov I. D., Kozlov A. F., Ivanova I. A., Valueva A. A., Tatur V. Y., Smelov M. V., Ivanova N. D., and Ziborov V. S., Sci. Rep. **10**, 9022 (2020).
3. Meyer N., Abrao-Nemeir I., Janot J.-M., Torrent J., Lepoitevin M., and Balme S., Adv. Colloid. Interface Sci. **298**, 102561 (2021).
4. Tan S. W., Gu D. J., Liu H., and Liu Q. J., Nanotechnology **27**, 155502 (2016).
5. Chau C. C. C., Weckman N. E., Thomson E., and Actis P., ACS Nano **19**, 3839–3851 (2025).
6. Ivanov Y. D., Ableev A. N., Shumov I. D., Ivanova I. A., Vaulin N. V., Lebedev D. V., Bukatin A. S., Mukhin I. S., and Archakov A. I., Int. J. Mol. Sci. **24**, 15636 (2023).
7. Metzler D. E. Biochemistry, the Chemical Reactions of Living Cells, 1st ed., Academic Press, Cambridge, UK, 1977; Moscow, Mir, 1980.
8. Xie X. S. and Lu H. P., J. Biol. Chem. **274** (23), 15967–15970 (1999).
9. Castronovo M., Lucesoli A., Parisse P., Kurnikova A., Malhotra A., Grassi M., Grassi G., Scaggiante B., Casalis L., and Scoles G., Nat. Commun. **2**, 297 (2010).
10. Neeli R., Girvan H. M., Lawrence A., Warren M. J., Leys D., Scrutton N. S., and Munro A. W., FEBS Lett. **579**, 5582–5588 (2005).
11. Narhi L. O. and Fulco A. J., J. Biol. Chem. **261** (16), 7160–7169 (1986).
12. Esteves F., Rueff J., and Kranendonk M. J., Xenobiot. **11**, 94–114 (2021).
13. Yamamoto D., Uchihashi T., Kodera N., Yamashita H., Nishikori S., Ogura T., Shibata M., and Ando T., Meth. Enzymol. **475**, 541–564 (2010).
14. Shinohara K. and Makida Y., Sci. Rep. **8**, 13982 (2018).
15. Antoniou M., Tsounidi D., Petrou P. S., Beltsios K. G., and Kakabakos S. E., Med. Devices Sens. **3**, e10072 (2020).

About authors

Shumov Ivan Dmitrievich, Candidate of Biological Sciences, Senior Researcher, Institute of Biomedical Chemistry (IBMC) (119121, Russia, Moscow, Pogodinskaya st., 10, bldg. 8). E-mail: shum230988@yandex.ru SPIN code: 3827-1620, AuthorID: 484732, ORCID: 0000-0002-9795-7065

Ziborov Vadim Serafimovich, Candidate of Physical and Mathematical Sciences, Senior Researcher, Institute of Biomedical Chemistry (IBMC) (119121, Russia, Moscow, Pogodinskaya st., 10, bldg. 8); Joint Institute for High Temperatures of Russian Academy of Sciences (JIHT) (125412, Russia, Moscow, Izhorskaya st., 13, bldg. 2). E-mail: ziborov.vs@yandex.ru AuthorID: 31839, ORCID: 0000-0001-7942-3337

Ableev Alexander Narimanovich, Lead Engineer, Institute of Biomedical Chemistry (IBMC) (119121, Russia, Moscow, Pogodinskaya st., 10, bldg. 8). E-mail: ableev@mail.ru SPIN code: 1193-5666; AuthorID: 1293547, ORCID: 0009-0004-3096-107X

Vinogradova Angelina Vladimirovna, Junior Researcher, Institute of Biomedical Chemistry (IBMC) (19121, Russia, Moscow, Pogodinskaya st., 10, bldg. 8). E-mail: angeluna1234@bk.ru SPIN code: 3979-1650, AuthorID: 1217129, ORCID: 0009-0001-6044-3490

Afonin Oleg Nikolaevich, Candidate of Technical Sciences, Senior Researcher, Institute of Biomedical Chemistry (IBMC) (19121, Russia, Moscow, Pogodinskaya st., 10, bldg. 8). E-mail: sunweb@mail.ru SPIN code: 1767-5835, AuthorID: 167545, ORCID: 0009-0008-7947-3674

Bukharina Natalia Sergeyevna, Candidate of Biological Sciences, Junior Researcher, Institute of Biomedical Chemistry (IBMC) (19121, Russia, Moscow, Pogodinskaya st., 10, bldg. 8). E-mail: natalia.bukho@gmail.com SPIN code: 8280-6076, AuthorID: 609294

Vaulin Nikita Vasilyevich, Laboratory Assistant, Alferov Federal State Budgetary Institution of Higher Education and Science Saint Petersburg National Research Academic University of the Russian Academy of Sciences (194021, Russia, Saint Petersburg, Khlopina st., 8, bldg. 3, letter A). E-mail: nikitavaylin@mail.ru SPIN code: 7466-5599, AuthorID: 1212356, ORCID: 0000-0001-6080-0729

Lebedev Denis Vladimirovich, Candidate of Physical and Mathematical Sciences, Senior Researcher, , Alferov Federal State Budgetary Institution of Higher Education and Science Saint Petersburg National Research Academic University of the Russian Academy of Sciences (194021, Russia, Saint Petersburg, Khlopina st., 8, bldg. 3, letter A). E-mail: denis.v.lebedev@gmail.com SPIN code: 8079-9286, AuthorID: 751908, ORCID: 0000-0001-5389-2899

Bukatin Anton Sergeevich, Candidate of Physical and Mathematical Sciences, Senior Researcher, Associate Professor, Alferov Federal State Budgetary Institution of Higher Education and Science Saint Petersburg National Research Academic University of the Russian Academy of Sciences (194021, Russia, Saint Petersburg, Khlopina st., 8, bldg. 3, letter A). E-mail: antbuk.fiztek@gmail.com SPIN code: 4604-0330, AuthorID: 744078 ORCID: 0000-0002-5459-1438

Mukhin Ivan Sergeeevich, Doctor of Physical and Mathematical Sciences, Professor, Head of the Laboratory, Alferov Federal State Budgetary Institution of Higher Education and Science Saint Petersburg National Research Academic University of the Russian Academy of Sciences (194021, Russia, Saint Petersburg, Khlopina st., 8, bldg. 3, letter A). E-mail: imukhin@yandex.ru SPIN code: 3242-8122, AuthorID: 546023, ORCID: 0000-0001-9792-045X

Saraeva Irina Nikolaevna, Candidate of Physical and Mathematical Sciences, Researcher, P. N. Lebedev Physical Institute of the Russian Academy of Sciences (119333, Russia, Moscow, Leninsky ave., 53). E-mail: saraevain@lebedev.ru SPIN code: 1795-7758, AuthorID: 889405, ORCID: 0000-0003-2362-023X

Archakov Alexander Ivanovich, Doctor of Biology, Academician of the Russian Academy of Sciences, Professor, Scientific Supervisor, Institute of Biomedical Chemistry (IBMC) (119121, Russia, Moscow, Pogodinskaya st., 10, bldg. 8). E-mail: alexander.archakov@ibmc.msk.ru SPIN code: 9412-0222, AuthorID: 78435, ORCID: 0000-0002-2290-8090

Ivanov Yuri Dmitrievich, Doctor of Biology, Professor, Head of the Laboratory, Institute of Biomedical Chemistry (IBMC) (119121, Russia, Moscow, Pogodinskaya st., 10, bldg. 8); Joint Institute for High Temperatures of Russian Academy of Sciences (JIHT) (125412, Russia, Moscow, Izhorskaya st., 13, bldg. 2). E-mail: yurii.ivanov.nata@gmail.com SPIN code: 7935-0461, AuthorID: 78445, ORCID: 0000-0001-5041-1914

INFORMATION

Rules for submission, reviewing and publishing of scientific papers

(as revised in 2026)

1. The "Applied Physics" journal is mainly intended for urgent publication of short papers concerning recent achievements in physics that have a potential of applied (technical and scientific) use. The journal is included in the new List of the Higher Attestation Commission, which came into effect on December 1, 2015.

By sending the article manuscript to the journal's editorial board, the authors grant the editorial board, founder and publisher of the journal a free, non-exclusive right to publish it in Russian as an article in the printed version of the journal, in the electronic version of the journal in the Internet and on laser disks. At the same time the authors retain their intellectual rights to the article manuscript (including "copyright"). In this regard and considering Part Four (Section VII) of the Civil Code of the Russian Federation, the authors shall submit a letter to the editor in the following form:

License agreement for transfer of the publish right (publishing license agreement)

We, the undersigned, the manuscript authors _____,
grant the editorial board, founder and publisher of "Applied Physics" journal a free, simple (non-exclusive) license to publish the article manuscript in both printed and electronic journal versions.

We confirm that this publication does not violate the intellectual rights of other persons or organizations. Signatures of authors: _____ (full name, academic degree, date)

The article shall be signed by all authors. If there are several authors, the name of the author responsible for message exchange with the editorial board shall be indicated. The article manuscript shall be sent to the address of the journal's editorial board: 111538, Moscow, Kosinskaya st, 9, AO NPO Orion, editorial board of "Applied Physics" journal or by e-mail: advance@orion-ir.ru

2. The article manuscript shall be submitted to the editor only in Russian.

3. The article manuscript shall be accompanied by an expert opinion whether its publication in the open media is allowed, which shall be drawn up in accordance with the established procedure.

4. The article size (including figures, bibliography and the English-language part) shall not exceed **7 pages** of A4 format with single line spacing. (A larger article is proposed to be sent to the affiliated **"Applied Physics Advances"** journal intended for publication of detailed articles and reviews). The article material shall be submitted in printed form (on paper) and in electronic form on a CD/DVD disk with the text in Word format (font type – Times New Roman, font size – 12), and the text shall already include figures with captions under them in the proper places. However, overly detailed and cumbersome mathematical transformations and expressions should be avoided in the text. The article styling shall be as follows:

– title of the journal section;
– UDK index;
– PACS classification code (https://publishing.aip.org/wp-content/uploads/2019/01/PACS_2010_Alpha.pdf);
– article title;
– initials and surnames of authors;
– abstract of the article (10–15 lines describing the purpose of the paper and its main findings);
– keywords;
– scientific specialty code.

5. The main text of the article shall begin with the "Introduction" section clearly stating the purpose and objectives of the paper along with arguments in favor of its preparation against the background of the existing state of the problem addressed in the article. The further text of the article shall also have meaningful headings (sections and subsections) without being numbered. The article shall end with a separate section, "Conclusion," listing the main findings, conclusions that follow from them, and, if possible, proposals for the research advance and use of its findings.

The bottom of the first page of the text shall accommodate a separate paragraph (in bold) containing contact information about the author (or authors) **(mandatory section)**: surname, first name, patronymic (in full), **e-mail (of all authors),** profiles and registration numbers in scientometric databases (SPIN code, RINTS Author ID, ArXiv Author ID, Orcid ID, Scopus Author ID), academic degree, title, position, postal address of the enterprise).

Also a person responsible for message exchange with the editorial board shall be specified.

Authors can suggest potential reviewers (2–3 people by indicating their full name, place of work, and email address). The proposed candidates shall not work in the institutions where the authors do.

The main text shall be followed by the list of references called “Bibliography”.
Examples of designations of references used in the "Bibliography" section.

Articles shall be referred to as follows: Surname, initials, journal title, year, volume, issue, page numbers.
Ivanov I. I. / Applied Physics. 2022. No. 1. P. 12–18.
Lang D. V. / J. Appl. Phys. 1974. Vol. 45. No. 7. R. 3023–3034.
Reference to **books**: Surname, initials, book title, city, publisher, year. (When a specific chapter or page in a book is referred to, the page number is placed after the year.)
Korn G., Korn E. Mathematical Handbook. – Moscow: Nauka, 1974.
Biberman L. M., Vorobiev V. S., Yakubov I. T. Kinetics of non-equilibrium low-temperature plasma. – Moscow: Nauka, 1982. P. 371.
Ultraviolet technologies in the modern world / edited by Karmazinov F.V. Kostyuchenko S.V., Kudryavtsev N.N. – Dolgoprudny: Intellekt, 2012.

Reference to **conference proceedings:** Surname, initials, title of publication, place and date of publication, page numbers.
Romanov A. V., Stepovich M. A., Filippov M. N. / Proceedings of the XVII International Conference "Radiation Physics of Solids". – Sevastopol, 2007. P. 592–599.

Reference to **patents**: Surname, initials, title, type, number, year.
Davydov S. G., Dolgov A. N., Yakubov R. H. Vacuum spark gap. Patent of invention No. 2654494 (RF). 2018.

Reference to **dissertations and Abstracts**: Surname, initials, title of paper (abstract), diss. … Candidate (Doctor) of Physics and Mathematics, city, organization, year.
Grechikhin V. A. Development and analysis of computer algorithms for processing single-particle signals of laser Doppler anemometers: Abstract from diss. by Candidate of technical sciences. – Moscow: MPEI, 1996.

Further, detailed English-language information about the article required for indexing the entire journal, the given article and its authors in international scientometric databases shall follow, namely: PACS, article title, authors' surname and initials (English transliteration), enterprise, its postal address, author(s) e-mail, abstract, keywords, references; since the journal is also distributed abroad, the editorial board reserve the right to correct the English part of the text without changing its meaning.
Styling of the References in the English part of the article has its own peculiarities. In particular, if the cited book or monograph is a translation into Russian from a foreign publication, the original data of this publication (authors, book title, publisher, city or country, year of publication) shall be given, as well as the Russian publisher and the year of publication in Russian. Given below are the main examples of designation of used references in the References section:

Article from the journal:
Ivanov I. I., Applied Physics, No. 1, 12–18 (2022) [in Russian].
Lang D. V., J. Appl. Phys. **45** (7), 3023–3034 (1974).
Note: if a Russian journal has a printed English analogue, the English title of the analogue shall be used and page numbers shall be taken therefrom. If there is no English analogue, the English transliteration of the Russian name shall be used.

Book:
Korn G. and Korn E. Mathematical Handbook. New York-London, Mcgraw-Hill Book Company, 1968; Moscow, Nauka, 1974.
Ultraviolet technologies in the modern world / ed. Karmazinov F. V., Kostyuchenko S. V., Kudryavtsev N. N. Dolgoprudny, Intellect, 2012 [in Russian].

Conference proceedings:
Romanov A. V., Stepovich M. A., and Filippov M. N. Proc. XVII Intern. Meeting on Radiation Physics of Solid State. Sevastopol, 2007, pp. 592–599.

Patents:
Davydov S. G., Dolgov A. N., Yakubov R. H. Vacuum spark gap. Patent for invention No. 2654494 (RF). 2018.
Dissertations and Abstracts:
Grechikhin V. A. Development and analysis of computer algorithms for processing single-particle signals of laser Doppler anemometers: Abstract. Diss. Candidate of Technical Sciences. M., MEI, 1996.

6. The list of references (“References”) shall correspond to all references to external sources used in the text of the article. These references shall be enclosed in square brackets, for example, [1–3], [7, 8]. Internal references, i.e. references to formulas, figures and tables of the article shall be enclosed in round brackets, for example, formula (3), equation (1), (Fig. 2), (Table 3). Any references in figure captions or in the figures are not recommended.

7. The number of figures and photos for a typical article shall not exceed 4. If one figure contains two, three or more variants of graphic (or photo) images of the type “Fig. 2*a*”, “Fig. 2*b*”, etc., each individual variant is considered as a separate figure. If the above limit number of figures (photos) is exceeded, the article is sent back to the authors for revision. Graphics (black and white and color) shall be put directly in the proper place in the article and in the proper scale. Next to the graph axes, the displayed physical quantities shall be indicated only (**strictly!**) using symbols (letters), and after a comma - the quantity dimension in Russian (in direct font). It is recommended to number different curves on graphs, even if they are identified by a different color or line type. Graphs shall be submitted only (**strictly!**) against the white background. Auxiliary grids are not allowed in the graph area.

8. Captions under the corresponding figures shall be out in the proper places in the text. Each caption shall be as short as possible, but meaningful in terms of its content. Any physical (technical) symbol included in the caption shall have its verbal explanation there.

9. Simple formulas shall be included in the text in the format of the text editor used; more complex formulas shall included using MathType formula editor. Standard mathematical notations (e.g. max, log, sin, exp, etc.) shall be typed directly. The same is true about figures and numbers. Formula numbers shall written in parentheses on the right. To indicate non-vector physical (technical) quantities using symbols, use only the Latin and Greek alphabets, while using a straight font for Greek letters, and an oblique font (italics) for Latin letters in the text. Vectors and matrices shall be marked by a bold, upright font (preferred) or an arrow above the italic vector symbol (less preferred). For subscripts and superscripts, use Arabic numerals, Latin or Greek letters, but if the index, usually a subscript, is a short (abbreviated) form of the Russian characteristic word, it is allowed to use Russian letters in its designation (uppercase font), for example U_{in}, I_{out}, v_{gr}, etc. The dimension of physical quantities shall be always given only in Russian, using an uppercase font.

10. Tables shall be made in accordance with the following requirements: the top line contains the data name and dimensions; the following lines contain the data itself.

11. Formulas, tables and figures shall have their own separate continuous numbering system. If there are no additional (return) references to a specific formula in the text or it is used only once, it shall not be numbered. A table and/or a figure used only once do not require numbering either.

12. Manuscripts and CD/DVD will not be sent back by the editorial board.

13. Authors (or an author) of each article after it is published in a journal issue have a right to receive an electronic version of the article in PDF format (Adobe Acrobat editor) from the editorial board.

14. When published in the journal, each article is accompanied by a footnote with the copyright symbol © placed before the author's name (authors’ names). The article shall also specify the date the article was received by the editorial board.

Applied Physics: Scientific and Technical Journal / RD&P Center ORION, JSC, 2026. No. 2.

Signed to the press on June 5, 2026
A4 format. Offset paper.
Digital printing.
Printed in the printing house of LLC PKK "YOUR FORMAT".
Address: 15, Malaya Kaluzhskaya st., Moscow, 119071.
Tel. (495) 749-45-84